DOLOMITE AND HIGH-MAGNESIUM CALCITE: CASE STUDIES FROM LABORATORY, FIELD, AND COMPUTER SIMULATION STUDIES

A Dissertation

by

CHIA PEI TEOH

Submitted to the Graduate and Professional School of
Texas A&M University
in partial fulfillment of the requirements for the degree of

DOCTOR OF PHILOSOPHY

Chair of Committee,	Juan Carlos Laya
Committee Members,	Ethan Grossman
	Michael Pope
	Mitchell Malone
Head of Department,	Julie Newman

August 2021

Major Subject: Geology

ABSTRACT

Dolomite ($CaMg(CO_3)_2$) is a diagenetic mineral occurring throughout geological time which replaces the precursor limestone via dolomitization. Dolomitization can alter rock properties such as porosity, permeability, and geochemistry; it requires a source of magnesium, a limestone precursor, and a hydrodynamic drive to move fluids through the limestone precursor. High-magnesium calcite (HMC) is of relevance as it can potentially satisfy the first two requirements of dolomitization on its own. This study examines the relationship between HMC and dolomite using high-temperature dolomite synthesis experiments, powdered X-ray diffraction, scanning electron microscopy, petrographical observations, geochemical analyses, digital outcrop models, and fluid flow simulations.

In high-temperature dolomite synthesis studies, we find that neither the rate of dolomitization nor dolomite stoichiometry correlate with HMC magnesium concentrations. However, mean dolomite crystal size has a negative relationship with HMC magnesium concentration. In field studies in Bonaire, selective dolomitization is observed within partially dolomitized samples, with the micrite matrix most likely to be dolomitized first, followed by coralline red algae, and subsequently all other allochems. Dolomitization also appears to have initiated from coralline red algae grains rather than by external fluids. Flow simulation results reveal an exponential relationship between water breakthrough times and flow rates versus dolomite proportions. Additionally, the arrangement of the dolomite bodies (aligned vs. disjoined) has very similar fluid flow behavior across a wide range of dolomite proportions. Sensitivity of flow behavior to the

geological models is strongly dependent on dolomite permeability relative to precursor limestone.

These studies have the following implications: 1) The observed correlation between coralline red algae abundance and global dolomitization events in the Neogene is not caused by reactant magnesium concentration, but likely reflects changes in species abundance and microstructure. 2) There is a more complex paragenetic sequence for the Seru Grandi clinoforms than previously known. 3) Having a good understanding of the dolomitization mechanism and dolomite body geometries reduces uncertainty in dolomite distributions and petrophysical properties in the subsurface, which allows for better fluid flow simulations.

DEDICATION

To perseverance, incrementalism, patience, and a generous helping of good luck.

ACKNOWLEDGEMENTS

I would like to thank my committee chair, Dr. Juan Carlos Laya, for taking a chance on me all those years ago and opening the door to another world of opportunities for me.

I would also like to thank my dissertation committee, Dr. Mike Pope, Dr. Ethan Grossman, and Dr. Mitch Malone for their input and guidance throughout my graduate school career.

I am grateful to my former master's supervisor, Professor Fiona Whitaker, whose unending ambition, decades of experience, and broad network has helped me be an all-around better scientist. Her past guidance has been instrumental in bringing me to where I am today.

Thanks go to the many friends and colleagues I have made and met along the way, for making my time in the US a more colorful and all-around wonderful experience.

I would like to thank the faculty and staff at the Department of Geology and Geophysics, for all the help, experience, and learning opportunities over all these years. My time in Texas A&M has been made all the richer as a result.

I would also like to thank the undergraduate students I have had the opportunity to work with, to mentor, and to teach over the years. They have made me realize how much I enjoy being an educator, and it is genuinely heartwarming to know I have made a positive impact in helping shape their future.

I am grateful for the experiences, the opportunities, the breakneck pace of learning, and for the additional figures in my bank account over the all too brief summers I had with Equinor and Shell.

I also want to thank my family back in Malaysia for their love, patience, and support through all the years as I hopped from one continent to another. I can only wish that times were better to allow us to see each other again soon.

Finally, the love of my life, Patricia Beatrice Teoh. My raft in a storm. My sunshine. My everything. I am forever grateful for your patience and unconditional love through all the dour days; be it through surreally stressful times or the simple yet deep discomfort of being apart yet again and again over the years I took to finish this dissertation. Thank you for choosing to be and to stay with me through merry and misery. This dissertation would not have been where it is today without you. Here is to a new chapter in our life that is about to start, one without another long goodbye at the airport or driveway.

CONTRIBUTORS AND FUNDING SOURCES

Contributors

This work was supervised by a dissertation committee consisting of Professor Juan Carlos Laya [advisor], Professor Michael Pope, and Professor Ethan Grossman of the Department of Geology & Geophysics and Professor Mitchell Malone of the Department of Oceanography.

The flow simulations and simulation data descriptions for Chapter 4 was provided by Dr. Carl Jacquemyn. The X-ray diffraction observations and dolomite synthesis experiments for Chapter 2 was greatly assisted by Dr. Stephen Kaczmarek and Katharine Rose.

All other work for the dissertation was completed by the student independently.

Funding Sources

This research was supported by multiple scholarships from the Berg-Hughes Center in the Department of Geology & Geophysics at Texas A&M University, by the IAS Travel Grant of the International Association of Sedimentologists, by the Outstanding Merit Award of the Geological Society of America, and a College of Geosciences Scholarship from Texas A&M University

NOMENCLATURE

CRA	Coralline red algae
Dol.	Dolomite
Cal.	Calcite
Mg	Magnesium
Ca	Calcium
HMC	High magnesium calcite
LA-ICP-MS	Laser Ablation Inductively Coupled Mass Spectrometer
LMC	Low magnesium calcite
SEM	Scanning Electron Microscopy
VHMC	Very high magnesium calcite
XRD	X-ray diffraction

TABLE OF CONTENTS

Page

LIST OF FIGURES

Page

LIST OF TABLES

Page

1. INTRODUCTION

Despite decades of intensive research into the formation of dolomite (dolomitization), there is still limited research which focused on the role of initial carbonate mineralogy in affecting dolomitization. This process is a diagenetic phenomenon in which carbonate minerals (e.g.: calcite, aragonite) are converted into dolomite in the following reaction:

$$2\ CaCO_3(s) + Mg^{2+} \leftrightarrow CaMg(CO_3)_2(s) + Ca^{2+}(aq)$$

For dolomitization to occur, a source of reactants (Mg, $CaCO_3$), high Mg/Ca ratios, fluid flow conditions which enables reactant transport to the dolomitization site, and favorable kinetic and thermodynamics are required (Morrow, 1982; Land, 1985; Warren, 2000; Whitaker et al., 2004). Inhibiting elements should also be minimized, which include presence of organic acids and complexation of Mg and Ca ions by Cl^- and SO_4^{2-} (Sibley et al., 1987, Swart, 2015). Thus, dolomitization is controlled by a complex interplay of variables which can either enhance or retard dolomitization. Previous studies have examined fluid salinity (Glover & Sipple, 1967), fluid Mg/Ca ratio (Carpenter, 1980; Usdowski, 1994, Kaczmarek & Sibley 2011, Sibley et al., 1987), fluid carbonate ion content (Morrow 1982; Machel & Mountjoy 1986), reactive surface area (Al-Helal et al. 2012), microbial activity (Wright 1999; Vasconcelos et al. 1995), initial mineralogy (Bartlett 1984; Land 1967), temperature (Kaczmarek & Thornton 2017) as well as

miscellaneous factors such as zinc concentration in dolomitizing fluid (Vandeginste et al., 2019), dioxane concentrations (Oomori and Kitano, 1987), polysaccharide concentrations (Zhang et al. 2012), and pCO_2 and pN_2 concentrations (Sibley, 1990).

Mineralogical differences were shown to result in vastly different dolomitization behaviors (Schlanger, 1957; Land and Epstein, 1970; Buchbinder, 1979; Kocurko, 1979; Sibley 1980 and 1982; Saller 1984; Bartlett, 1984; Land, 1967; Gaines, 1980; Katz and Matthews, 1976; Baker and Kastner, 1981; Bullen and Sibley, 1984), which include changing the dolomitization rate, nucleation density, crystal sizes, and the preservability of microfabrics within carbonate bioclasts. While several of these studies examined the role of high-Mg calcite (HMC) in dolomitization, there are currently no studies which specifically and systematically quantify changes in dolomitization rate, dolomite stoichiometry, dolomite textures, and preferential dolomitization in HMC. Additionally, global dolomitization events in the Neogene (Budd 1997) were suggested to be linked the species abundance of HMC-producing taxa such as coralline red algae (Laya et al. 2018). Considering the Neogene hosts a significant amount of carbonate reservoirs (Epting 1980), understanding this link can be of global economic importance as well. This gap in knowledge and the unexplored link in the Neogene with HMC forms the overarching basis for the studies included in this dissertation.

High- Mg calcite is precipitated chiefly in marine waters within calcareous skeletons, cements, and occasionally ooids (James and Jones 2016). Among HMC-secreting organisms, which include coralline red algae, benthic foraminifera, and echinoderms, coralline red algae often have the greatest concentrations of mole %

$MgCO_3$ (8 – 30 mol% $MgCO_3$) within their calcareous skeletons (Chave 1954). Magnesium incorporated into calcite in HMC is distributed randomly within the cation layers; this has implications for calcite solubility, which is a function of Mg content. That is, as Mg-calcite solubility increases with increasing Mg content. Relative to aragonite, HMC of >8 mole % $MgCO_3$ is more soluble than aragonite at equivalent conditions (Walter 1985).

At a broader scale, dolomitization is significant from an economic perspective as dolomitized reservoirs comprise the bulk of the world's carbonate petroleum reserves, which form 60% of global oil reserves (Burchette, 2012; Choquette and Roehl, 1985). This is because dolomitization commonly involves changes in petrophysical properties relative to its precursor limestone, which according to one model, reduces crystal sizes due to the higher density of dolomite relative to calcite and aragonite, leaving additional pore space in a closed system (Choquette and Pray 1970; Blatt et al. 1980; Roehl and Choquette 1985). However, this also introduces additional heterogeneity within a rock unit (Lucia and Major 1994). Therefore, understanding porosity and permeability changes related to dolomitization will provide a significant tool to predict reservoir performance. This forms the basis for the study in Chapter 4.

The overarching goal of this dissertation is to examine in detail the relationship between HMC and dolomite under laboratory, field, and computer simulation settings. Three research questions will form the basis of our investigations: 1) *Does magnesium concentration in biogenic high-Mg calcite (HMC) affect dolomitization?* 2) *Are HMC bioclasts preferentially dolomitized* 3) *What are the effects of dolomite geobodies on*

flow behavior in carbonate clinoforms? These research questions are addressed in chapters 2, 3, and 4 respectively.

2. THE EFFECTS OF MAGNESIUM CONCENTRATION IN HIGH-MAGNESIUM ALLOCHEMS ON DOLOMITIZATION: INSIGHTS FROM HIGH TEMPERATURE DOLOMITE SYNTHESIS EXPERIMENTS

2.1. Synopsis

Dolomitization of Neogene carbonates is common and has been linked to the abundance of high-Mg calcite (HMC) allochems such as coralline red algae in the precursor limestone. It has been proposed that the higher magnesium concentration in these allochems promotes dolomitization. To investigate the impact of magnesium concentration (mol% $MgCO_3$) in biogenic HMC on dolomitization, high temperature (200℃) dolomitization experiments were conducted to track dolomite reaction rates, dolomite stoichiometry, and dolomite textures for a variety of solid HMC reactants. Solids were characterized using standard powdered X-ray diffraction (XRD) and scanning electron microscopy (SEM). All experiments except those with *Corallina officinalis* exhibit replacement of the HMC reactants by protodolomite products. Except for *Goniolithon,* neither the rate of dolomitization nor protodolomite stoichiometry correlate with HMC reactant magnesium concentration. Mean protodolomite crystal size, however, exhibits a negative relationship with HMC reactant magnesium concentration. Dolomitized HMC skeletons reliably retain the original microstructure of the reactant. These findings collectively suggest that under the conditions investigated, dolomitization is less affected by reactant magnesium concentration than by other factors such as reactant microstructure and fluid chemistry. These results imply that the observed

correlation between coralline red algae abundance and global dolomitization events in the Neogene is not caused by reactant magnesium concentration, but more likely reflects changes in species abundance and microstructure.

2.2. Introduction

Dolomite, $CaMg(CO_3)_2$, is a common diagenetic mineral in the Phanerozoic rock record that forms by the replacement of a precursor $CaCO_3$ by dissolution-precipitation (Sun 1994). In the past 60 years, our understanding of dolomite has progressed substantially, yet there remains much controversy and uncertainty about where and how dolomitization occurs (Machel 2004; Kaczmarek et al. 2017; Petrash et al. 2017). One such controversy pertains to the reported global dolomitization events in the Neogene (Sibley 1980; Budd 1997a). One hypothesis proposed for these events is that there is a potential relationship between the high-magnesium calcite (HMC) skeletons of coralline red algae relative to species richness (a proxy for species abundance) with dolomitization (Laya et al. 2018c). Given that HMC can act as an additional source of magnesium (Mg) for dolomitization and the Mg/Ca of the solution has been shown in laboratory experiments to increase dolomitization rates (Kaczmarek and Sibley, 2011), the abundance of HMC allochems may prove predictive for dolomitization abundance.

Among common HMC secreting organisms (e.g., coralline red algae, benthic foraminifera, and echinoderms), coralline red algae skeletons generally have the highest concentrations of $MgCO_3$ (10 – 30 mole % $MgCO_3$) (Chave 1952; Chave 1954; Morse and Mackenzie 1990). Coralline red algae are globally pervasive (Adey and Macintyre

1973). Additionally, they are major limestone constituents since the Cretaceous (Aguirre et al. 2000), and have periodically been major reef builders, particularly in the Neogene when species richness of coralline red algae was at its peak (Aguirre et al. 2000; Halfar and Mutti 2005; Steinthorsdottir et al. 2020). Numerous studies have noted the relationship between coralline red algae and dolomitization (Schlanger 1957; Ohde and Kitano 1981; Saller 1984; Budd 1997a; Laya et al. 2018a). Theorized by Goodell and Garman (1969) based on their observations of Holocene and subsurface rocks in Andros Island, Bahamas, these HMC skeletal grains may liberate enough Mg-ions to dolomitize the local sediment at least partially without an additional Mg source. This hypothesis is consistent with reports that coralline red algae are typically mimetically dolomitized (Sibley 1982; Bullen and Sibley 1984) and occasionally preferentially dolomitized in mixed mineralogy sediments (Schlanger 1957; Buchbinder and Friedman 1970; Buchbinder 1979). It has also been reported that coralline red algae contain small volumes of disordered dolomite within their skeletal structure (Nash et al. 2011; Nash et al. 2013; Diaz-Pulido et al. 2014; Nash et al. 2015).

Given that dolomitization occurs via a dissolution-precipitation reaction (**Equation 1**)(Machel 2004), it can be expected that changes in reactant Mg concentration and thus reactant solubility will affect the equilibrium state of the reaction by increasing or decreasing the reactant ions availability such as Mg^{2+} and CO_3^{2-}. Coupled with the observation that HMC solubility increases with increasing magnesium concentration (magnesium concentration) (Walter 1985), higher magnesium concentration in the reactants provides a viable pathway to increase dolomite saturation

states, which may have implications for dolomite textures (Sibley 1991) and dolomitization rates (Land 1967).

$$2CaCO_{3\,(s)} + Mg^{2+}_{(aq)} \rightarrow CaMg(CO_3)_{2\,(s)} + Ca^{2+}_{(aq)} \quad \textbf{(Equation 1)}$$

High-temperature experiments indicate that the controls on dolomitization are numerous, including temperature (Gaines, 1968; Kaczmarek and Thornton, 2017), Mg/Ca concentrations (Kaczmarek and Sibley 2011), salinity (Glover and Sippel 1967; Cohen and Kaczmarek 2017), organic matter content (Gaines 1980; Kenward et al. 2013; Roberts et al. 2013; Petrash et al. 2017), precursor mineralogy (Land 1967), and precursor texture (Bullen and Sibley 1984). Many of these parameters show similar tendencies in the field (Qing and Mountjoy 1994; Ren and Jones 2017; Manche and Kaczmarek 2019). In terms of reactant mineralogy, the most common $CaCO_3$ precursors investigated experimentally are low-Mg calcite (LMC), high-Mg calcite (HMC), and aragonite, all of which show different dolomitization behaviors. For example, low-Mg calcite (LMC), HMC, and aragonite have been shown to cause differences in the dolomitization rate (Land 1967; Sibley et al. 1987), selective dolomitization (Schlanger 1957; Land and Epstein 1970; Kocurko 1979; Kaczmarek and Sibley 2014), dolomite stoichiometry (Rose and Kaczmarek 2019), and microfabric retention in skeletal grains (Bullen and Sibley 1984). Despite the extensive list of studies, however, none have attempted to quantify the effects of Mg concentration in HMC reactant on dolomite stoichiometry, dolomite crystal texture, and dolomitization rate. As the vast majority of

HMC in the rock record originates from biogenic sources which are affected by organic matter content, microstructure/texture, and species/phylum, all these variables require scrutiny alongside Mg concentration in biogenic HMC.

High-temperature dolomite synthesis experiments have a demonstrated validity in understanding low-temperature sedimentary dolomites. For example, Kaczmarek and Sibley (2007) observed the same growth and dissolution features between synthetic and natural dolomites in a wide range of formation conditions and growth rates. This observation suggests that the mechanisms that govern dolomite crystal precipitation and growth are directly applicable to both high-temperature synthetic and low-temperature natural dolomites. Furthermore, a study by Bullen and Sibley (1984) showed similar textures between their synthetically dolomitized skeletal grains with those observed in nature. Dolomite textures result from an interplay between different temperatures, pressure, dolomitizing fluid composition, precursor microstructure, time and precursor mineralogy (Sibley and Gregg 1987). Ultimately, these factors affect the two fundamental controls of dolomite texture: the density of nucleation sites and crystal growth mechanisms. Collectively, these studies help us understand the variables that control dolomitization, which otherwise would have been extremely difficult if not impossible to recreate under low-temperature laboratory conditions (Land 1998).

In the case of dolomitization of HMC skeletal grains, they are commonly mimetically dolomitized over other mineral precursors (Bullen and Sibley 1984; Sibley 1991; Mansour and Abd-Ellatif 2013; Laya et al. 2018a). For HMC skeletal grains to retain their intricate microstructures, a high density of nucleation sites is required, which

is a result of mineralogy and reactive surface area (Sibley 1991). In HMC skeletal grains, a high density of nucleation sites is often achieved due to their higher solubility compared to other minerals (Walter 1985) and their cryptocrystalline structure (Auer and Piller 2020), which greatly increases the reactive surface area. Thus, this consistency in preservation of microstructures among HMC skeletal grains can be utilized to infer the original fossil mineralogy in ancient rocks and suggests that microstructure imparts a strong control on dolomitization.

This study addresses the following research question: *Does magnesium concentration in biogenic high-Mg calcite (HMC) affect dolomitization?* Magnesium has been known to play an important role in affecting dolomitization rates, stoichiometries, and textures (Land 1967; Bullen and Sibley 1984; Kaczmarek and Sibley 2011), but previous studies have primarily examined fluid sources of magnesium, leaving the contribution of HMC derived magnesium unclear. To answer this question, we use high temperature dolomite synthesis experiments in combination with XRD and SEM analyses to examine how magnesium concentration in biogenic HMC reactants affects 1) reaction rate, 2) stoichiometry, and 3) dolomite textures.

2.3. Methods

High-temperature dolomite synthesis experiments were conducted in Teflon-lined stainless-steel acid-digestion vessels following a similar method of Kaczmarek and Thornton (2017). Experiments were designed to test the effect of Mg concentrations of HMC skeletal grains on dolomitization reaction rate, dolomite stoichiometry, and

dolomite texture. The specific variables investigated are magnesium content of HMC reactants, reaction rate, product stoichiometry, and reactant microstructure. Reaction temperature, reactant solid size fraction, reactant solid mass, solution chemistry, and solution volume were held constant between experiments.

2.3.1. Sample preparation and screening

Six different HMC samples were investigated (**Table 2-1**). The samples are composed of different coralline red algae specimens (*Goniolithon, Lithophyllum,* and *Lithothamnion*) chosen for their ubiquity during the Neogene (Braga and Aguirre 1995; Braga and Aguirre 2001; Laya et al. 2018a). *Goniolithon* is identified as taxonomically equal with *Lithophyllum* (Guiry and Guiry 2021) , but we consider the two specimens as different separate genera for consistency with previous studies on HMC and dolomitization (Land 1967; Land and Epstein 1970; Nash et al. 2011). All samples were pulverized manually in an agate mortar and pestle and dry sieved to 63 - 75 μm size fractions using USA Standard ASTM E-11 specification testing sieves. All samples were cleaned using 2 cycles of 24-hour chemical treatment with dilute sodium hypochlorite (NaClO), 99.9% isopropyl alcohol, and de-ionized water, modified from the method used by Bischoff et al. (1983) to remove residual organic matter and minimize its effect on reactions. Prepared reactants were dried and stored in a vacuum desiccator.

Table 2-1: List of sample types used, their mineralogy, and initial $MgCO_3$ content.

Sample	Mineralogy	Type	Initial Mg Content (mol% $MgCO_3$)	Origin
Goniolithon sp.	High-Mg Calcite (HMC)	Coralline red algae (branching)	23.4	The Bahamas
Lithophyllum sp.	High-Mg Calcite (HMC)	Coralline red algae (branching)	20.1	The Bahamas
*Lithothamnion sp.**	Mixed (HMC + Aragonite)	Coralline red algae (encrusting)	17.5	The Bahamas
Corallina officinalis	High-Mg Calcite (HMC)	Coralline seaweed	12.4	Nova Scotia
Heterocentrotus mamillatus^	High-Mg Calcite (HMC)	Echinoderm	11.3	Hawaii
Mellita quinquiesperforata°	High-Mg Calcite (HMC)	Echinoderm	14.1	Florida

*Mixed mineralogy, can contain up to 30% aragonite.
^Radiols/spikes sampled. Will be referred to as sea urchins.
°Will be referred to as sand dollars.

As a check for residual organic matter in samples, the remaining organic matter content in all samples is quantified after cleaning. A UIC Coulometrics CM5011 CM5015 coulometer and a Thermo Electron Corporation FlashEA 1112 CHNS elemental analyzer were used in tandem to quantify the amount of total organic carbon (TOC) in cleaned, crushed, and sieved unreacted samples. Approximately 15 mg of sample and an excess amount of 2M HCl are reacted to evolve carbon dioxide, which is carried by N_2 carrier gas into a coulometer cell. Within the coulometer cell, a buffer solution containing a colorimetric pH indicator and a photodetector is autotitrated to quantify the amount of CO_2 released. Assuming that all inorganic carbon is present in

the sample as calcium carbonate, the amount of CO_2 released is used to calculate the total inorganic carbon (TIC) based on the following equation:

$$wt\%\ CaCO_3 = \ \mu g\ C\ \times \frac{8.333}{Sample\ Mass\ (\mu g)}$$

To obtain TOC, TIC is subtracted from the total carbon (TC) of the sample. Approximately 5 mg of sample were loaded into tin capsules, which were then combusted at 950 °C to vaporize the samples to determine elemental concentrations of carbon, hydrogen, nitrogen, and sulfur via gas chromatography. The elemental concentration (in wt. %) of carbon as measured via gas chromatography is taken as the TC of the sample. Blanks and standards were run after every 10 samples. All organic matter is assumed to be present as organic carbon; hence TOC represents the weight percentage of organic matter within the samples. Only residual amounts (<3 wt.% TOC) of organic matter are detected in all HMC reactants used (**Table 2-2**), except *Corallina officinalis* which had 6.38 wt.% TOC**.**

Table 2-2: Total organic carbon (TOC) values in weight % of all cleaned HMC samples.

Sample	Type	TOC (%)
Goniolithon sp.	Coralline Red Algae (branching)	1.82
Lithophyllum sp.	Coralline Red Algae (branching)	2.52
Lithothamnion sp.	Coralline Red Algae (encrusting)	0.52
Mellita quinquiesperforata	Echinoderm	0.36
Corallina officinalis	Coralline Seaweed	6.38
Heterocentrotus mamillatus	Echinoderm	0.44

2.3.2. High-temperature dolomite synthesis experiments

The experimental design necessitates that the vast majority of carbonate (CO_3^{2-}) ions are sourced directly from the dissolving HMC reactants. Magnesium ions, conversely, can be sourced by either the dissolving HMC reactants or the 1.0 M Mg-Ca-Cl stock solution with an initial Mg/Ca ratio of 1.0. Experimental solutions were prepared by combining 1L of deionized water and 1 mole each of reagent grade magnesium chloride ($MgCl_2 \cdot 6H_2O$) and calcium chloride ($CaCl_2 \cdot 2H_2O$). Reaction vessels were loaded with 100 mg of solid reactant and 15 ml of the stock solution. Vessels were then sealed and placed into a high precision convection oven pre-heated to 200 °C. Reaction vessels were assumed to reach 200 °C in one hour. Dolomite synthesis experiments lasted between 1 and 46 hours. Reaction vessels were periodically removed from the oven at predetermined times and forced cooled to ambient conditions in 30 minutes using compressed air. Reacted solids were filtered from reacted fluids, rinsed with de-ionized water in a vacuum flask and subsequently dried in a vacuum desiccator.

The dolomitization rate is calculated based on trendline slope for each reaction curve, which is defined by the end of the induction period (a period of after which the experiments have started, but with no products are detected with XRD) to the first datapoint with >90% product, with steeper gradients representing higher dolomitization rates. A cutoff of ~90% product is used such that we primarily capture the reaction rate of only the "replacement period" reaction phase of dolomitization (Kaczmarek and Sibley 2014). The gradients represent the amount of product precipitated per hour.

2.3.3. Powdered X-ray diffraction (XRD)

Standard powdered X-ray diffractometry techniques (Goldsmith and Graf 1958) were used to determine mineralogy and proportions of solid products. Solids were hand pulverized using an agate mortar and pestle. Powdered samples were mounted on a boron-doped silicon P-type zero background diffraction plate and analyzed using either a Rigaku Miniflex 600 or a Bruker D2 Phaser diffractometer. Both instruments use CuKα radiation (λ= 1.54184 Å). Powdered halite (NaCl) was added as an internal standard to calibrate diffraction peak positions as modified from the method of Kaczmarek and Sibley (2011).

Solid mineralogy was characterized according to three XRD-measured parameters: (i) Relative proportions of protodolomite/dolomite and HMC, (ii) Mg content of HMC reactants, (iii) Mg content of protodolomite/dolomite products. Percent Mg of initial HMC reactants was determined using the relative corrected position of the

calcite 104 peak (Zhang et al. 2010). Relative proportions of the solid reactants and products were determined using the corrected intensity ratios of the dominant XRD reflections for calcite and protodolomite/dolomite (Goldsmith and Graf 1958). Stoichiometry of the Ca-Mg-carbonate products was calculated according to the relative corrected d-spacing of the dolomite (104) peak, consistent with the method of Lumsden (1979). We follow the definition of Gaines (1977) for protodolomite, which refers to metastable single-phase rhombohedral carbonates which are imperfectly ordered. The distinction between protodolomite and dolomite is made by the XRD observation of dolomite superlattice reflection peaks, specifically the dolomite 105 peak, which is a principle order reflection peak that is absent in protodolomite but present in dolomite (Goldsmith and Graf 1958).

2.3.4. Scanning electron microscopy (SEM) and crystal size distribution (CSD)

A Phenom XL Desktop SEM and a JEOL JSM-7500F at 2 – 15 kV in backscattered electron (BSE) mode were used to image the solid reactants at a working distance of 6 - 15 mm to characterize all solids. SEM samples were imaged uncoated or coated with approximately 4 nm of carbon. Textural descriptions of the solid reactants and products are based on the criteria summarized in Flügel (2004) and Sibley and Gregg (1987). For this study, the term “texture” refers to the crystal size (and distribution of sizes), shape, orientation, and packing of dolomite rhombs (Blatt et al. 1980). Crystal size distributions were measured for the Ca-Mg-carbonate products using the longest visible axis of dolomite crystals in SEM using scaled photomicrographs in

JMicrovision 1.3.3, similar to the method used by Sibley et al. (1993). Between 150 and 400 crystals were measured for each sample along multiple linear transverses to reduce sampling bias towards larger crystals. Anhedral crystals or those without at least two observable diagonally opposed corners were excluded. Skewness and kurtosis were measured for each crystal size distribution.

2.3.5. Heterogeneity quantification

Sample microstructure was characterized and quantified by SEM observations. The relative rankings of the external surface roughness, a proxy for reactive surface area (RSA), is calculated based on image analyses of SEM observations of crushed and sieved samples at the initial stage. Specifically, each sample prior to reaction is quantified for the amount of heterogeneity according to the method described in Chappard et al. (2003), wherein each (8-bit, 256 level) grayscale SEM image is mapped and binned to 3 levels of black (0 – 85), grey (86 – 171), and white (172 – 255). The amount of heterogeneity was defined after enumerating the number of pixels for black (A_b), gray (A_g), and white (A_w) in the following equation:

$$Heterogeneity = \frac{A_b + A_w}{A_b + A_g + A_w}$$

Heterogeneity values closer to 1.0 indicate a largely uniform surface, whereas heterogeneity values closer to 0 indicate a highly heterogeneous surface.

2.4. Results

2.4.1. Reaction profile and transient phases

All dolomitization reactions follow a pattern of replacement similar to that observed in previous studies (e.g., Kaczmarek and Sibley (2014)). The model posited by Kaczmarek and Sibley (2014) describes the dolomitization reaction as a series of stages and in this study three reaction stages are primarily observed. These include (i) a period of after which the experiments have started, but with no products are detected with XRD (herein this is referred to as the induction period (Sibley et al. 1987)), (ii) a period of rapid replacement whereby the reactants are replaced by protodolomite, and (iii) a period of primary recrystallization when most of the initial reactant is exhausted (<10% remaining), wherein protodolomite is gradually replaced by ordered dolomite as evidenced by the appearance of XRD cation ordering peaks. We will refer to the reaction products that do not display cation ordering peaks as protodolomite, whereas reaction products that display cation ordering peaks will be referred to as dolomite.

2.4.2. Reaction rates and induction period

Dolomitization rate varied significantly between the different HMC reactants. The fastest reactant was completely dolomitized in almost a quarter of the time it took to completely dolomitize the slowest HMC reactant, from 8.83 to 32.78 % product/hr. (**Fig. 2-1**). *Goniolithon sp*. (23.4 mole % $MgCO_3$) exhibited the fastest reaction rate at 32.78% product/hr. These values are followed by sea urchin at 12.4% product/hr., sand dollar at

10.96% product/hr., and *Lithophyllum* at 8.83% product/hr. *Lithothamnion* exhibited the slowest reaction rate at 8.28% product/hr.

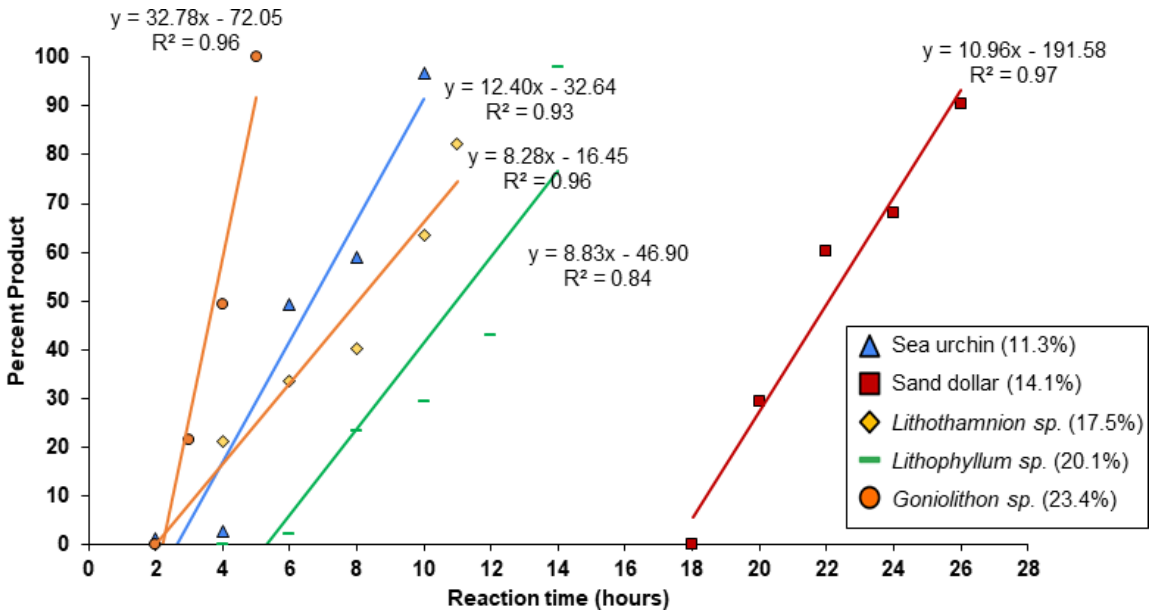

Figure 2-1: Cross plot of percent product (protodolomite, dolomite) as a function of reaction time in hours for all experiments run using HMC. Percentages in legend refer to the initial concentration of HMC in mole % $MgCO_3$ in sample tested.

The induction period for experiments using *Goniolithon sp.* yield the first protodolomite products at 3 hours, *Lithothamnion* and sea urchin samples yielded detectable protodolomite at 4 hours, *Lithophyllum* yielded detectable protodolomite at 6 hours. In contrast, sand dollar (14.1 mole % $MgCO_3$) lacked detectable protodolomite

until 20 hours. *Corallina officinalis* experiments yielded no detectable protodolomite at 46 hours, the longest experiment conducted.

2.4.3. Stoichiometry

The stoichiometry of the initial protodolomite products ranges from 42.6 to 47.4 mole % Mg (**Fig. 2-2**). *Goniolithon* experiments consistently yield the highest VHMC stoichiometry at 47.0 to 47.4 mole% $MgCO_3$., *Lithothamnion* experiments consistently produce the most calcian protodolomite at 43.0 mole% Mg to 44.6 mole% $MgCO_3$. Stoichiometry of the initial products remains largely unchanged throughout the reaction prior to 80% dolomitization, with stoichiometry varying by no more than 1 - 3 mole% Mg within a single series (**Fig. 2-2**).

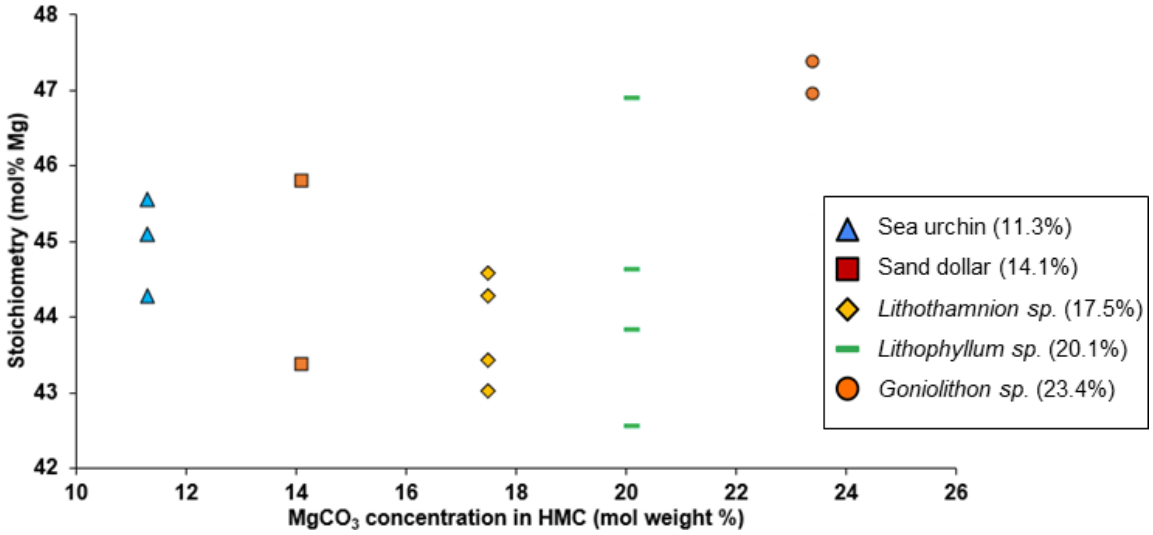

Figure 2-2: Cross plot of dolomite stoichiometry as a function of initial Mg concentration (see Table 2-1) for samples exhibiting no observable cation ordering XRD reflections (dolomite 015 peak). Percentages in legend refer to the initial concentration of HMC in mole % $MgCO_3$ in sample tested.

2.4.4. Microstructure changes and dolomite textures

2.4.4.1. Initial sample textures

Coralline red algae *Goniolithon sp.*, *Lithothamnion sp.*, *Lithophyllum sp* (**Fig. 2-3 A, B, C**) and coralline seaweed *Corallina officinalis* (**Fig. 2-3 D**) are characterized by columnar cellular structures and variable cell wall thicknesses with circular to hexagonal horizontal cross sections. However, several differences are noted. *Goniolithon* generally has larger and flatter cells (**Fig. 2-3 A**), whereas *Lithophyllum* has smaller and more elongate cells (**Fig. 2-3 B**). *Corallina* presents a similar structure to *Lithophyllum* (**Fig. 2-3 D**), with even smaller and elongated cells with cell widths of ~5 µm and cell lengths of ~35 µm. *Lithothamnion* has a very variable appearance, with generally compact cells.

These cells stack and form a network-like structure. Unique among all samples, *Lithothamnion* encrusts on and incorporates an aragonite substrate into its structure, of which aragonite makes up no more than 30% of the total mineralogy based on XRD analyses. Upon crushing, the microstructures for sand dollar, sea urchin, *Goniolithon*, *Corallina*, and *Lithophyllum* remain mostly intact. *Lithothamnion* has a superficial layer of stacked columnar cells on the aragonite substrate. However, the cellular columns are rarely preserved after pulverization, leaving only remnants of the cellular network. Echinoderms (Sand dollar, Sea urchin) universally have a fine network of interconnected HMC interspaced with round pores (stereom) (Mann 2009) (**Fig. 2-3 E, F**). Sea urchin stereom exhibit larger pore diameters (5-20 μm) than sand dollar stereom (2 - 15 μm). A more in-depth description of the biomineralization and anatomy of the microstructures described for echinoderms can be read in Smith (1990) and for coralline red algae, in Auer and Piller (2020).

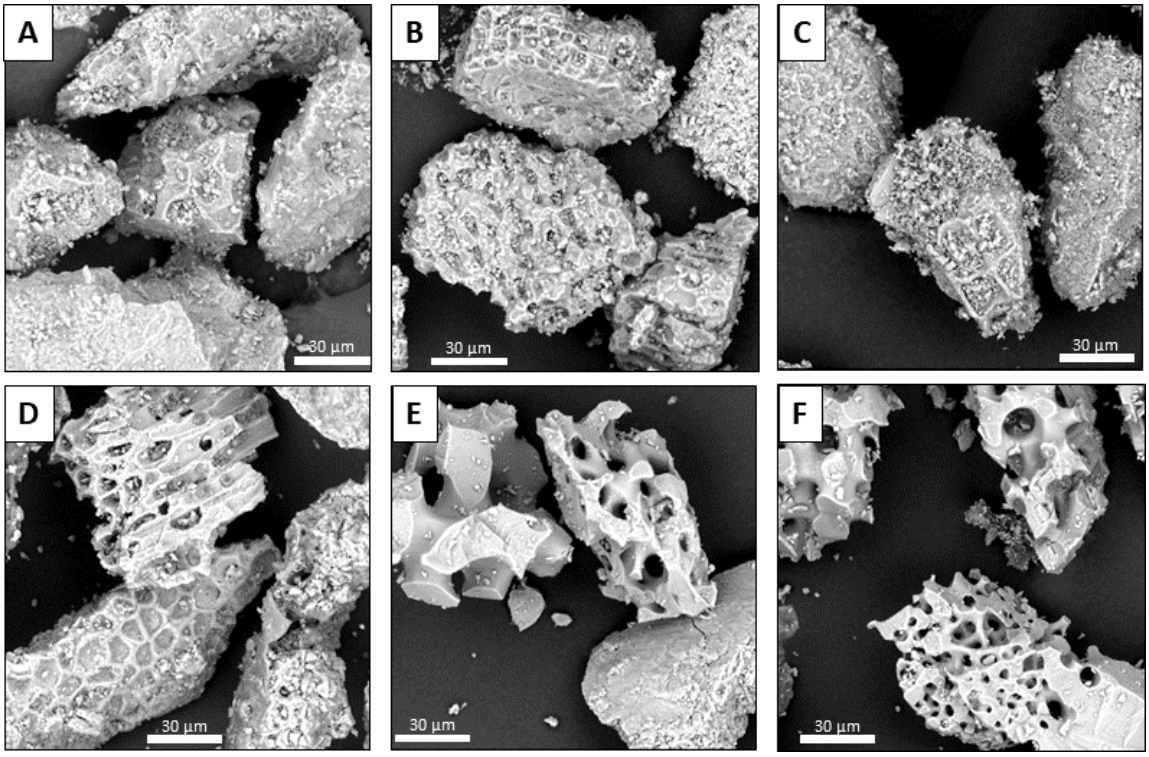

Figure 2-3: SEM photomicrographs showing pulverized and sieved samples prior to reaction. Much of the initial microstructure present is variably preserved despite pulverization. (A) *Goniolithon sp.,* (B) *Lithophyllum sp.,* (C) *Lithothamnion sp.,* (D) *Corallina officinalis,* (E) *Heterocentrotus mamillatus,* (F) *Mellita quinquiesperforata.*

Lithothamnion samples showed the highest heterogeneity value at 0.61, while the branching coralline algae (*Goniolithon*, *Lithophyllum*, and *Corallina*) display similar heterogeneity values from 0.64 to 0.67). Sand dollar samples are observed to have the lowest amount of heterogeneity among HMC samples at 0.74 (**Table 2-3**).

Table 2-3: Initial surface heterogeneity values for tested samples.

Sample	Heterogeneity
Goniolithon sp.	0.64
Lithophyllum sp.	0.64
Lithothamnion sp.	0.61
Sand dollar	0.74
Corallina officinalis	0.67
Sea urchin	0.72

2.4.4.2. Partial dolomitization

Goniolithon microstructure exhibits small changes after partial dolomitization; with few dissolution features, no change in cell structure, and very small (<1 μm) rhombic protodolomite crystals (**Fig. 2-4**). *Lithophyllum* also shows minor changes during partial dolomitization, with limited dissolution features, and no changes in cell structure. The rhombic dolomite crystals preferentially occur within the fracture planes in both *Goniolithon* and *Lithophyllum*. These protodolomite crystals are <1 μm, have a spotted mosaic fabric, planar-s habit, and show no consistent orientation (**Fig. 2-4**).

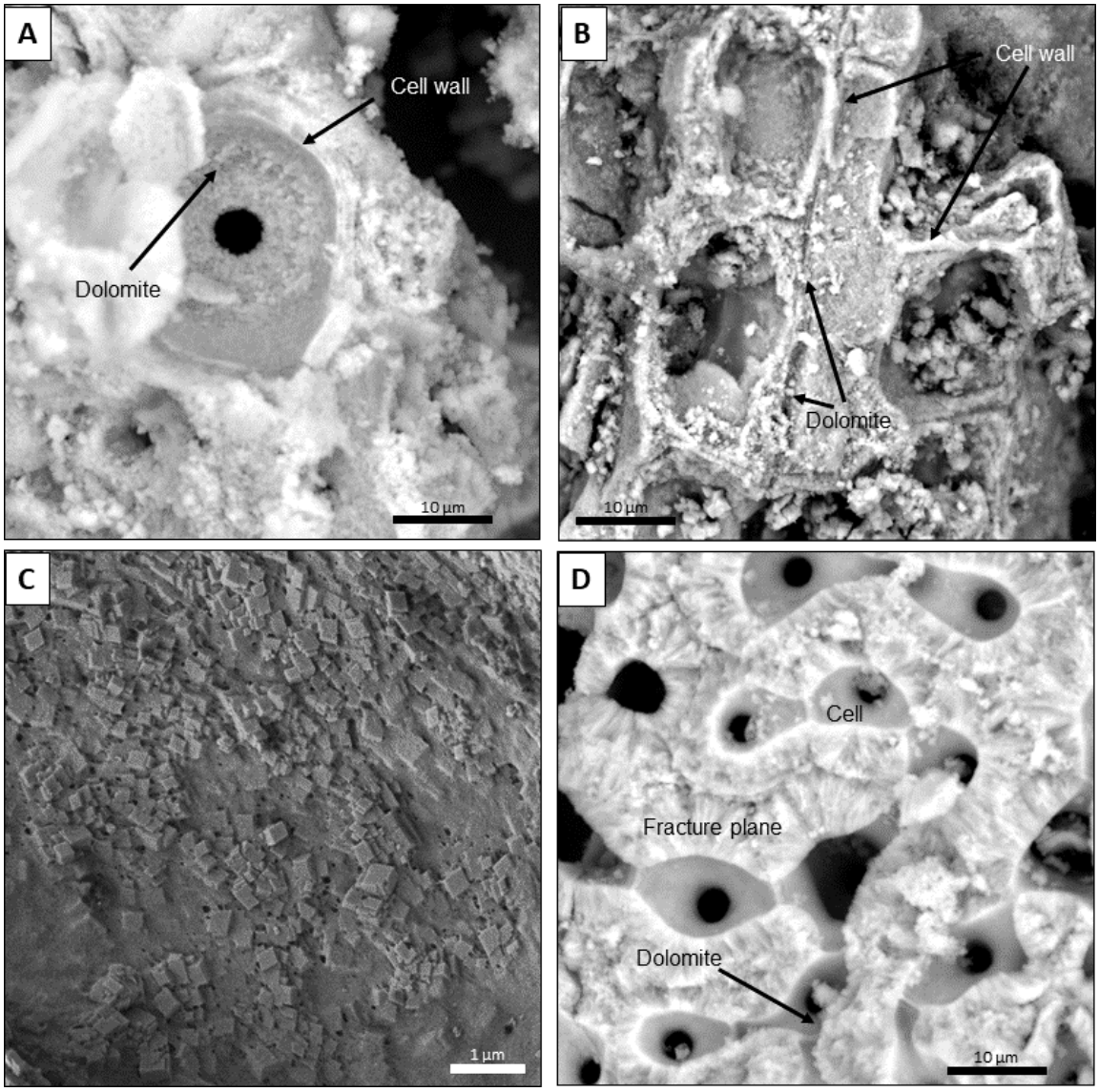

Figure 2-4: SEM micrographs of partially dolomitized *Goniolithon sp*. and *Lithophyllum sp.* (A), (B) View into *Goniolithon* cells, showing the coarsening of the initially smooth cell walls. Dolomite crystals are typically submicron, and euhedral. (C) High magnification view of *Goniolithon* sample showing dolomite crystals precipitating out of and within HMC surface. (D) View into *Lithothamnion* cells, showing the concentration of initial dolomitization within the fracture planes of the fragments.

Both echinoderms (sand dollar, sea urchin) show features indicative of intense dissolution concentrated along discontinuities in the original skeletal structure, while more indiscriminate dissolution features manifest as a rough and wrinkled appearance with peak to troughs widths of ~1 µm on skeletal surfaces **(Fig. 2-5)**. The rhombic protodolomite crystals covering the echinoderms are ~1 µm, have a sutured mosaic fabric, planar-s habit, and are aligned in a single orientation. The protodolomite crystals are most commonly present within the skeletal structure, with fewer occurring as a surface layer on the skeletal surface.

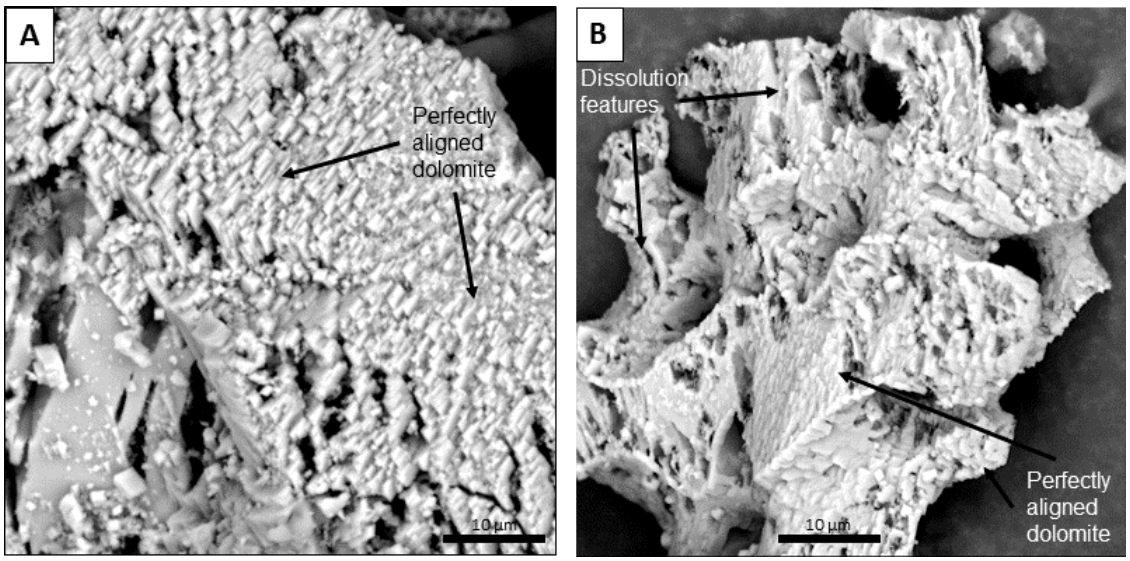

Figure 2-5: SEM micrographs of partially dolomitized sand dollar and sea urchin samples. (A) Strongly fabric-oriented dolomite crystals growing on concurrently dissolving sea urchin fragment. (B) Sand dollar sample, showing dissolution enhanced within surface fractures on stereom, with concurrent precipitation of subhedral to euhedral dolomite throughout. Subhedral to euhedral dolomite crystals forming on surface of sand dollar stereom. Note the perfect alignment of virtually all dolomite crystals.

The encrusting coralline red algae, *Lithothamnion sp.* display minute (<1 µm) dissolution features, smaller rhombic protodolomite crystals, and a higher density of crystals. These crystals are ~1 µm, exhibit a sutured mosaic fabric, planar-e habit, and are randomly orientated on the aragonite substrate; in the HMC areas the protodolomite crystals are <1 µm, display a sutured mosaic fabric, planar-s habit, and are randomly oriented (**Fig. 2-6**).

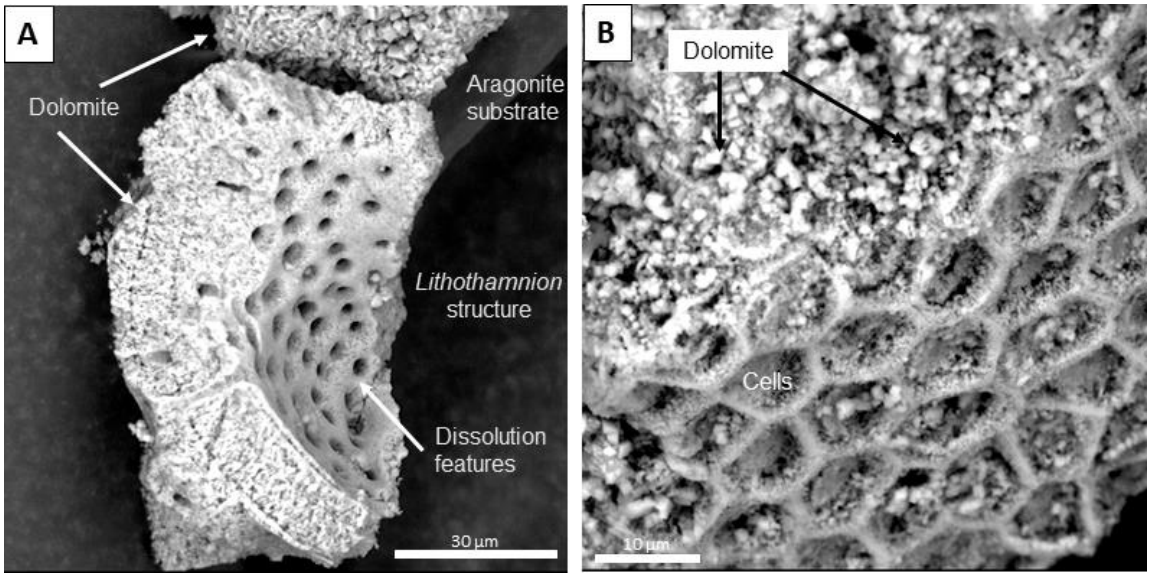

Figure 2-6: SEM micrographs of partially dolomitized *Lithothamnion sp.*. (A) (B) Well preserved cellular network of encrusting *Lithothamnion*, with very minute dissolution features throughout. Larger and more euhedral dolomite crystals appearing to preferentially form on aragonite substrate.

When partially dolomitized, the echinoderms (sand dollar, sea urchin) both exhibit similar mean crystal sizes (2 µm and 1.7 µm, respectively) with kurtosis and skewness values indicating long right tails and sharp distributions. *Lithothamnion* sample has a mean crystal size of 1.9 µm with a highly skewed distribution. *Lithophyllum* samples have a mean of 0.2 µm and a very skewed and relatively broad distribution. *Goniolithon* samples have a mean of 0.3 µm and a very skewed and very sharp distribution. (**Table 2-4**) (**Fig. 2-7**). *Corallina officinalis* samples showed no evidence of dolomitization over the entire study period.

Table 2-4: Statistical results for all crystal size distributions

Sample	Mean (µm)	Median (µm)	Standard Deviation	Skewness	Kurtosis
Partially dolomitized					
Goniolithon	0.3	0.3	0.15	2.26	7.01
Lithophyllum	0.2	0.2	0.15	1.43	1.91
Lithothamnion	1.9	1.8	0.57	0.98	2.66
Sand dollar	2	1.9	0.86	1.74	6.12
Sea urchin	1.7	1.4	1.07	1.94	4.78
Completely dolomitized					
Goniolithon	0.5	0.5	0.32	1.31	2.02
Lithophyllum	1.3	1.3	0.28	1.81	0.72
Lithothamnion	2.2	2.1	0.8	1.07	1.67
Sand dollar	2.4	2.1	1.12	1.28	1.85
Sea urchin	2.4	2.1	1.18	1.47	2.8

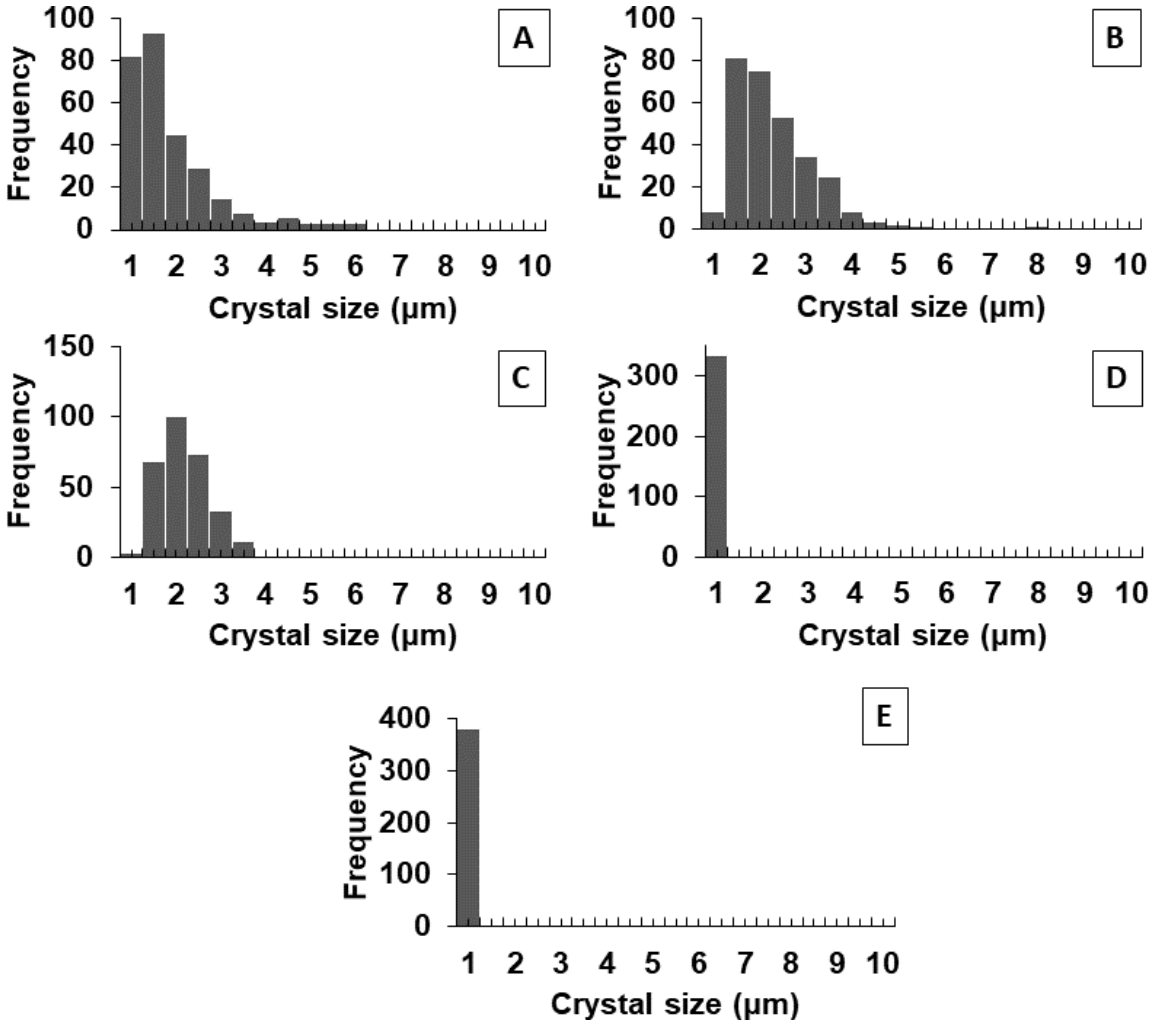

Figure 2-7: Crystal size distributions for partially dolomitized (<50% dolomitized) samples. (A) sea urchin. (B) sand dollar. (C) *Lithothamnion*. (D) *Lithophyllum*. (E) *Goniolithon*.

2.4.4.3. Complete dolomitization (>90% Products)

All reactants show a crystal size increase at complete dolomitization compared to at partial dolomitization (**Fig. 2-8**). In *Goniolithon* samples, the replacement rhombic dolomite is mimetic with an average diameter of <1 μm, present a spotted mosaic fabric, with a mix of planar-s and planar-e habit, and are randomly orientated (**Fig. 2-9**). Dolomite crystals forming in *Lithophyllum* display similar textures, with generally larger rhombic dolomite crystals than those from *Goniolithon* experiments (**Fig. 2-9**). For both branching coralline red algae, the euhedral and larger crystals are commonly located on the edges of the microstructure and along fracture planes (**Fig. 2-9 C**).

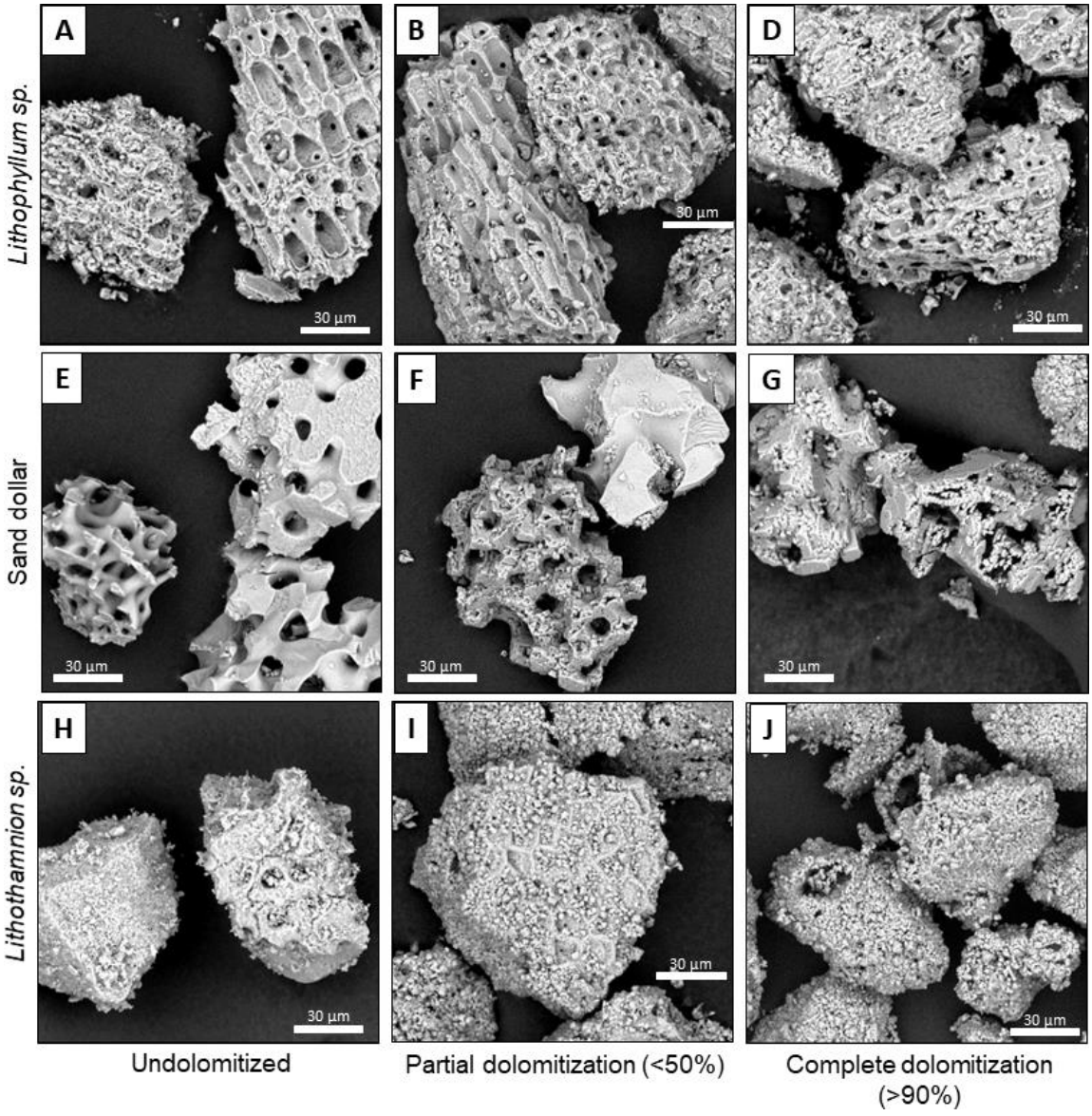

Figure 2-8: SEM photomicrographs showing undolomitized, partially dolomitized (<50% dolomitized), and fully dolomitized (>90% dolomitized) samples exhibiting changes in texture and dolomite crystal rhomb sizes as dolomitization progresses. (A), (B), and (C) display *Lithophyllum sp*., with an average of <1 µm dolomite rhombs at full dolomitization. (E), (F), and (G) display *Mellita quinquiesperforata* (Sand dollar) with an average of 3 µm dolomite rhombs at full dolomitization. (H), (I), and (J) display monocrystalline aragonite, with an average of 5 µm dolomite rhombs at full dolomitization. There is an apparent trend between the magnesium content (aragonite having the lowest at 0 mole % Mg, and *Lithophyllum sp.* having the highest in this figure at 18.9 mol % Mg) and average dolomite crystal size at full dolomitization, with lower magnesium content resulting in larger dolomite rhombs.

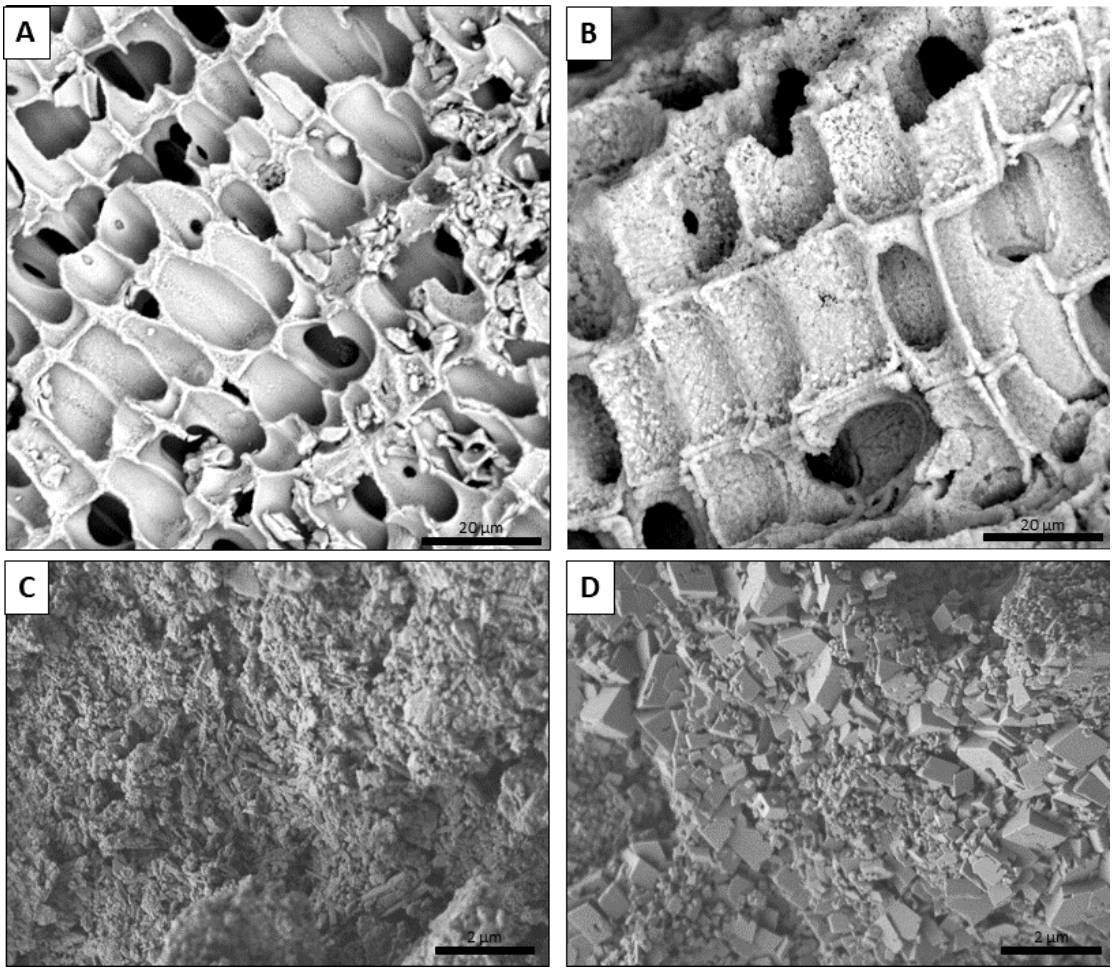

Figure 2-9: SEM micrographs of undolomitized and dolomitized *Goniolithon sp*.. (A) Undolomitized, cross sectional view showing the vertical profile of the coralline red algae cellular network. (B) Dolomitized, cross sectional view of the coralline red algae cellular network. Note the significant roughening of the surfaces upon pervasive dolomitization. The overall microstructure is still strongly recognizable. (C) High magnification view of fine calcite crystallites within *Goniolithon* structure. (D) High magnification view of dolomite crystals replacing fine calcite crystallites, resulting in overall coarsening of observable crystals.

Completely dolomitized *Lithothamnion* show rhombic dolomite crystals that are on average 3 - 4 µm, have a sutured mosaic fabric, planar-s habit, and are randomly orientated on the aragonite substrate. On the HMC cells, dolomite crystals are on average <1 µm, sutured mosaic fabric, planar-s to nonplanar habit, and are aligned in a single orientation **(Fig. 2-10)**.

Both completely dolomitized echinoderms show similar textures (**Fig. 2-11**). Dolomite crystals are on average 2 - 3 µm, rhombic, have a sutured mosaic fabric, planar-s, and are aligned in a single orientation. Hollow remnants of echinoderm fragments are also common.

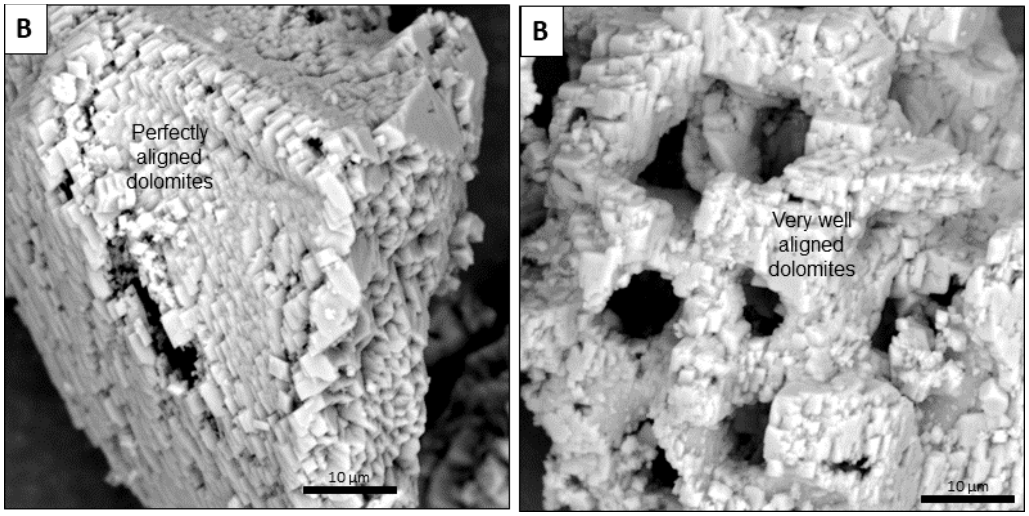

Figure 2-10: SEM micrographs of completely dolomitized sand dollar and sea urchin samples. (A) Sea urchin fragment fully replaced by perfectly aligned euhedral to subhedral dolomite. (B) Sand dollar fragment fully replaced by euhedral to subhedral dolomite. Coarse microstructure of bioclast remains somewhat preserved. Note the strongly preferred orientation of all dolomite crystals.

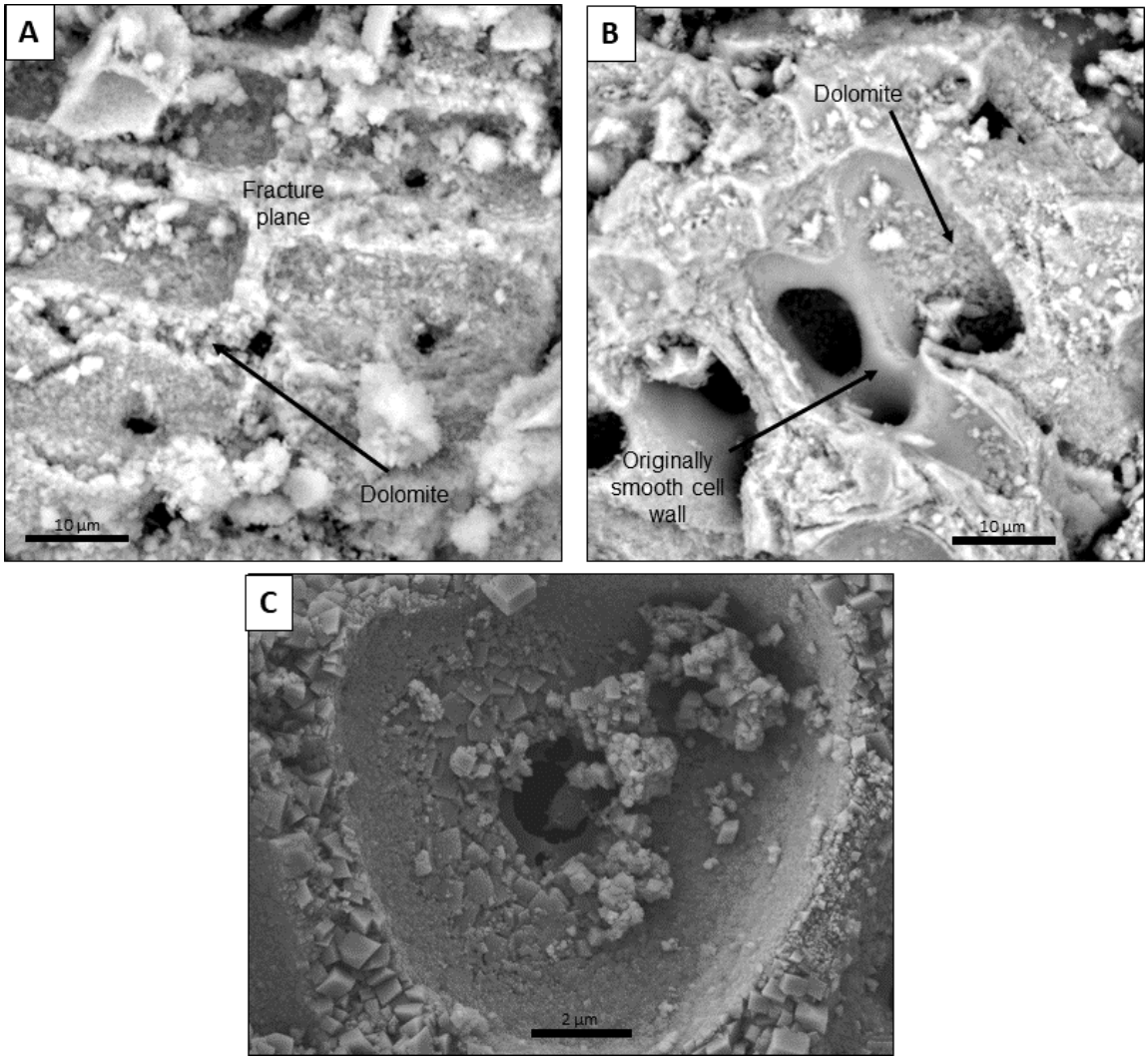

Figure 2-11: SEM micrographs of completely dolomitized *Lithophyllum sp*. and *Goniolithon sp.*. (A) *Lithophyllum* sample, view into cells, showing the largely fabric preserving nature of dolomite crystals despite the pervasive dolomitization. (B) *Goniolithon* sample, view into cells, with notable heterogeneity in where dolomite appears to be forming and distorting the originally smooth surfaces. (C) *Lithophyllum* sample, the largest euhedral to subhedral dolomite crystals appear to be concentrated within the cellular wall fracture planes.

Fully dolomitized materials have larger mean dolomite crystal sizes than their partially dolomitized counterparts (**Fig. 12**). Both echinoderms have similar mean crystal sizes (2.4 μm), with kurtosis and skewness values indicating a reduction in skewness and overall flattening of the distribution relative to at partial dolomitization. *Lithothamnion* shows a similar reduction in skewness and overall flattening in the crystal size distribution and has a mean crystal size of 2.2 μm. *Lithophyllum* experiments have a mean of 1.3 μm and a very skewed and relatively flat distribution. *Goniolithon* experiments have the smallest dolomite crystals, with a mean of 0.5 μm, and skewed and relatively flat distribution (**Table 4**). All reacted samples show unimodal distributions and are strongly skewed (skewness >0.5). Partially dolomitized samples show sharp distributions (kurtosis >3), whereas fully dolomitized samples tend to show flatter distributions (kurtosis <3) relative to their partially dolomitized counterparts (**Fig. 13**).

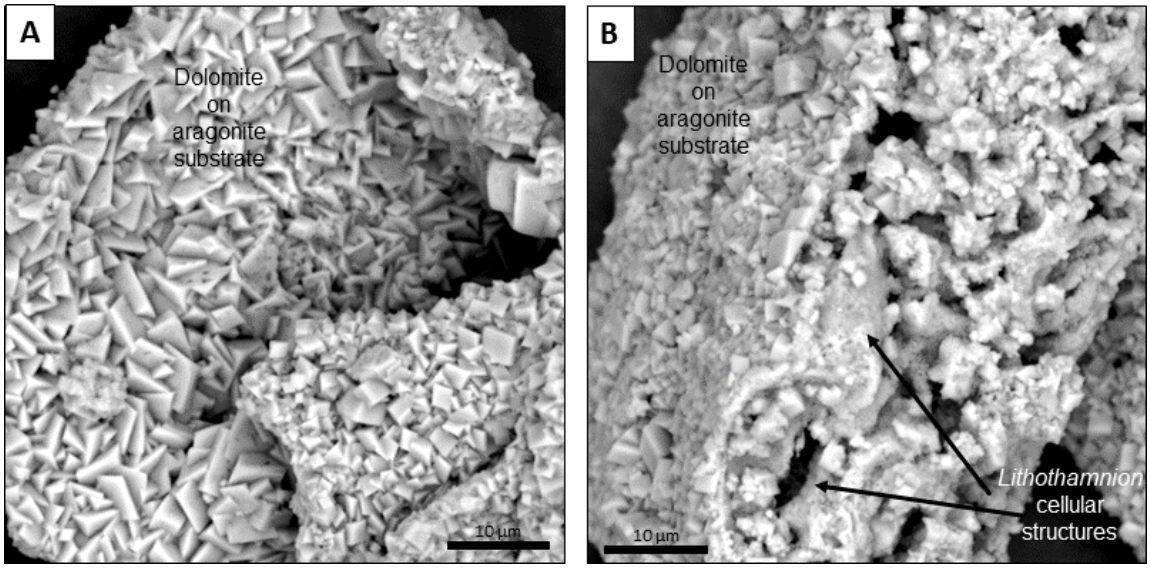

Figure 2-12: SEM micrographs of completely dolomitized *Lithothamnion sp*.. (A), (B) Partially hollowed out fragment of *Lithothamnion* with pervasive replacement by dolomite crystals. Smaller and less euhedral crystals concentrating within remnant encrusting *Lithothamnion* cellular structures, with larger and more euhedral crystals precipitating on aragonite substrate.

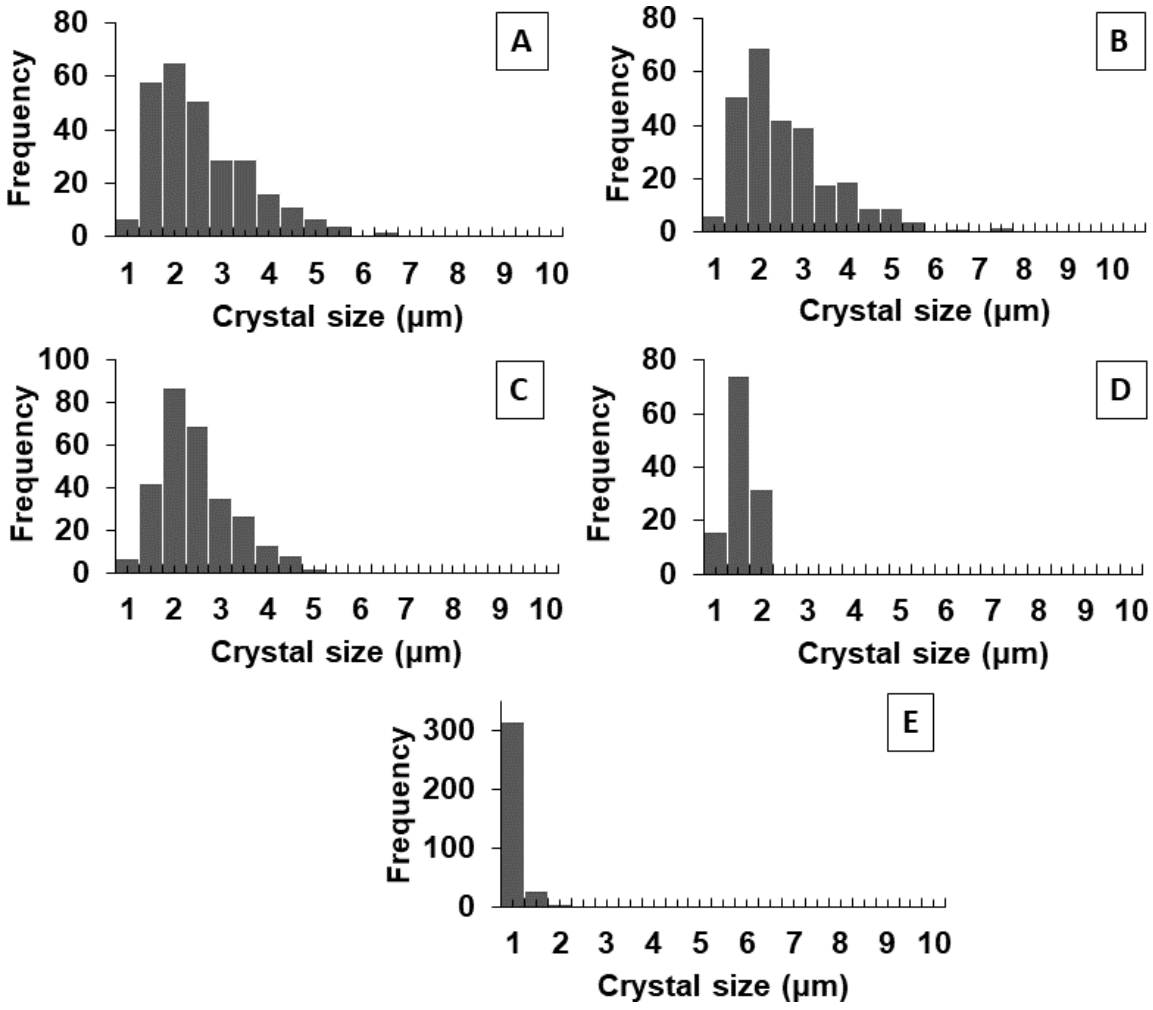

Figure 2-13: Crystal size distributions for completely (>90%) dolomitized samples. (A) sea urchin. (B) sand dollar. (C) *Lithothamnion*. (D) *Lithophyllum*. (E) *Goniolithon*.

2.5. Discussion

2.5.1. Does magnesium concentration in biogenic high-Mg calcite (HMC) affect dolomitization rate, stoichiometry, and the induction period?

The magnesium concentrations in the skeletal reactants do not correlate with dolomitization rate (**Fig. 2-1**). The initial and intuitive assumption tested here is that reactants with higher magnesium concentration would liberate more Mg into the solution during replacement, thus increasing the Mg/Ca of the solution, which has been shown experimentally to increase the rate of dolomitization (Kaczmarek and Sibley 2011). However, except for *Goniolithon* having a consistently high Mg concentration/fast dolomitization, we observe that the dolomitization rate does not follow a predictable pattern between the magnesium concentration in HMC and the rate of dolomitization.

One factor that may contribute to the lack of correlation of magnesium concentration with dolomitization rate is a non-linear relationship between the amount of Mg liberated into solution with the magnesium concentration of HMC. This was observed in a study by Land (1967) where the fluid Mg/Ca was tracked during dissolution experiments of different HMC skeletal grains (which include *Goniolithon* [23 mole % $MgCO_3$], *Amphiroa* [16 mole % $MgCO_3$], and *Lithophyllum* [14 mole % $MgCO_3$]). Measurements in the resulting solution show Mg/Ca ratios did not correspond to mol% $MgCO_3$ in the different skeletal grains. However, stabilization of *Goniolithon* to LMC in Land's (1967) study resulted in the highest Mg/Ca ratio in solution among the previously mentioned HMC skeletal grains, with Mg/Ca ratios nearly 4 times greater than both *Amphiroa* and *Lithophyllum*, despite only having approximately 30% more

Mg. The solution equilibrated with the one echinoderm (*Arbacia*, 7 mol% Mg) tested by Land (1967) ended up with a solution Mg/Ca ratio greater than either *Amphiroa* or *Lithophyllum* solutions. All these observations indicate that higher HMC magnesium concentration does not result in higher Mg/Ca ratios in solution (which implies a net increase in magnesium concentration versus [Ca] in solution). Thus, as the Mg/Ca ratio in solution strongly controls dolomitization rates (Kaczmarek and Sibley 2011), a higher magnesium concentration in HMC will not necessarily result in faster dolomitization rates.

The length of the induction period and dolomite stoichiometry do not covary with Mg concentration of the solid reactants likely due to several factors (**Fig. 2-1, 2- 2**). As previously described, there is a non-linear relationship between the magnesium concentration of HMC allochems and the magnesium concentration liberated into solution upon stabilization of HMC. As with reaction rate, dolomite stoichiometry is strongly controlled by solution Mg/Ca (Kaczmarek and Sibley 2011). Mg/Ca can increase with a net increase of magnesium concentration relative to calcium concentrations upon dissolution of HMC; dolomitization by higher solution Mg/Ca ratios generally resulting in more stoichiometric dolomite. Secondly, the induction period is shown to be a non-linear function of Mg/Ca ratio of the solution and it is less pronounced at Mg/Ca ratios greater than 1.0 (Kaczmarek and Sibley 2007). For example, sand dollar reactants have an unusually long induction period of almost 20 hours, which does not appear to be explained by Mg concentration nor microstructure considering its similarity in both with sea urchin reactants (which had an induction

period of 4 hours). This observation reaffirms the findings of Kaczmarek and Sibley (2011) that fluid Mg/Ca ratio is a strong control on both the induction period and stoichiometry

Corallina officinalis samples did not react to form any detectable protodolomite within the study period. This observation is likely due to *Corallina*'s unusually high organic content (**Table 2-2**). Previous studies have shown that organic material in natural bioclasts may slow down reaction rates of carbonates by altering the reaction kinetics of carbonate minerals (Falini et al. 1996; Morse et al. 2007). For dolomitization specifically, Gaines (1980) observed that the addition of gelatin and dilute aspartic acid slowed dolomitization, both common biological compounds. The persistence of organic material within *Corallina* used in this study despite robust cleaning procedures can be attributed to its biomineralization mechanism, which results in poorer calcification (thus higher initial organic matter content) and a much more intricate microstructure (Nash et al. 2019). More complex calcite microstructures can host inclusions of organic material even in a single crystal (Pérez-Huerta et al. 2019; 2020), which are ultimately shielded from chemical treatments due to the reduced access to the small pore throats within these microstructures. Hashim and Kaczmarek (2020) have noted similar behavior between treated and untreated carbonate allochems in calcite stabilization experiments suggesting that chemical treatments cannot eliminate all organic matter that is hosted within the microstructure of our specific skeletal reactants.

The inference that HMC reactant microstructure is a stronger control on dolomitization rate than magnesium concentration is driven by our observations showing

a correlation between dolomitization rate and surface heterogeneity (**Fig. 2-1, Table 2-3**), which is used here as a proxy for reactive surface area (RSA). The microstructure of the reactant effectively dictates the reactive surface area (RSA) that is available for dolomitization, wherein more complex microstructures or more heterogeneous surfaces would indicate more RSA. Both echinoderms (sand dollar and sea urchin), which have very similar surface heterogeneity values (0.72 & 0.74), have comparable reaction rates (12.4 % product/hr. & 11.0 % product/hr.). In contrast, the remaining coralline red algae, *Lithothamnion* and *Lithophyllum*, with heterogeneity values of 0.61 and 0.64, respectively, also have similar reaction rates (8.28 % product/hr. for *Lithothamnion,* 8.83 % product/hr. for *Lithophyllum*). Thus, our data suggest that HMC reactants with similar microstructures will have similar reaction rates regardless of their Mg concentration. This observation is consistent with the conclusion of Bullen and Sibley (1984), who suggested that selective dolomitization is more likely driven by reactant crystal size than mineralogy. In fact, RSA has been shown in multiple studies to exert a strong effect on dolomitization rates (Gaines 1980; Sibley et al. 1987).

Goniolithon consistently falls off trends in reaction rate, induction period, and stoichiometry, an observation that can be attributed to its higher efficiency at releasing Mg into solution. This increased efficiency can likely be attributed to the occurrence of brucite that naturally appears in *Goniolithon* (Schmalz 1965; Weber and Kaufman 1965; Moberly 1970), which seems to increase the skeletal grain's solubility relative to other skeletal carbonates (Schmalz 1965; Stumm and Morgan 2012). However, the presence of brucite in skeletal carbonates is not necessarily unique to *Goniolithon,* as other

coralline red algae species and corals contain brucite (Milliman et al. 1971; Buster and Holmes 2006; Nash et al. 2015). This observation indicates that there is perhaps a species dependency due to biological structures and compositions, which subsequently controls dissolution rates.

2.5.2. Dolomite textures

Though mean dolomite crystal size correlates with skeletal reactant magnesium concentration, reactant microstructure is also a contributing variable. The HMC skeletal grains with lower initial Mg concentrations correlate with larger mean dolomite crystal size ($r^2 = 0.87$). However, this relationship is less pronounced when the reactant has only been partially dolomitized ($r^2 = 0.67$), with a much larger spread in crystal sizes for a given reactant magnesium concentration **(Fig. 2-14)**. Previous work suggests that dolomite crystal sizes are a function of both nucleation densities and growth kinetics (Sibley and Gregg, 1987), with high nucleation densities generally producing smaller crystals, and low nucleation densities producing larger crystals. Nucleation density have been inferred to increase with fluid supersaturation with respect dolomite, nucleation site availability, and decreases in surface free energy (Sibley 1982). In the context of our study, supersaturation of the fluid with respect to dolomite can be controlled by either the Mg concentration of HMC or the overall solubility of the reactant, whereas availability of nucleation sites is regulated by the initial microstructure of the reactants. Our observation that protodolomite and dolomite crystal sizes decreases with increasing reactant magnesium concentration suggests that an increase in Mg concentration in the

HMC increases the nucleation rate of dolomite. However, the data also suggests that similar microstructures produce similar mean dolomite crystal sizes. For example, sand dollar and sea urchin samples, which have very similar microstructures and surface heterogeneity values (0.72 and 0.74) form similar dolomite mean crystal sizes when fully dolomitized (2.4 μm). In contrast, *Lithophyllum* and *Goniolithon* experiments which also have very similar microstructures and surface heterogeneity values (0.64 for both), show different dolomite crystal sizes (1.3 μm and 0.5 μm), possibly due to *Goniolithon*'s affinity to release Mg into solution. While *Lithothamnion* samples share similar microstructures and surface heterogeneity values with the *Lithophyllum* and *Goniolithon*, *Lithothamnion* is observed to incorporate up to 30% of aragonite into its structure, which may skew its mean dolomite crystal sizes upwards as aragonite tends to dolomitize in a fabric destructive manner which implies larger dolomite crystal sizes (Bullen and Sibley 1984).

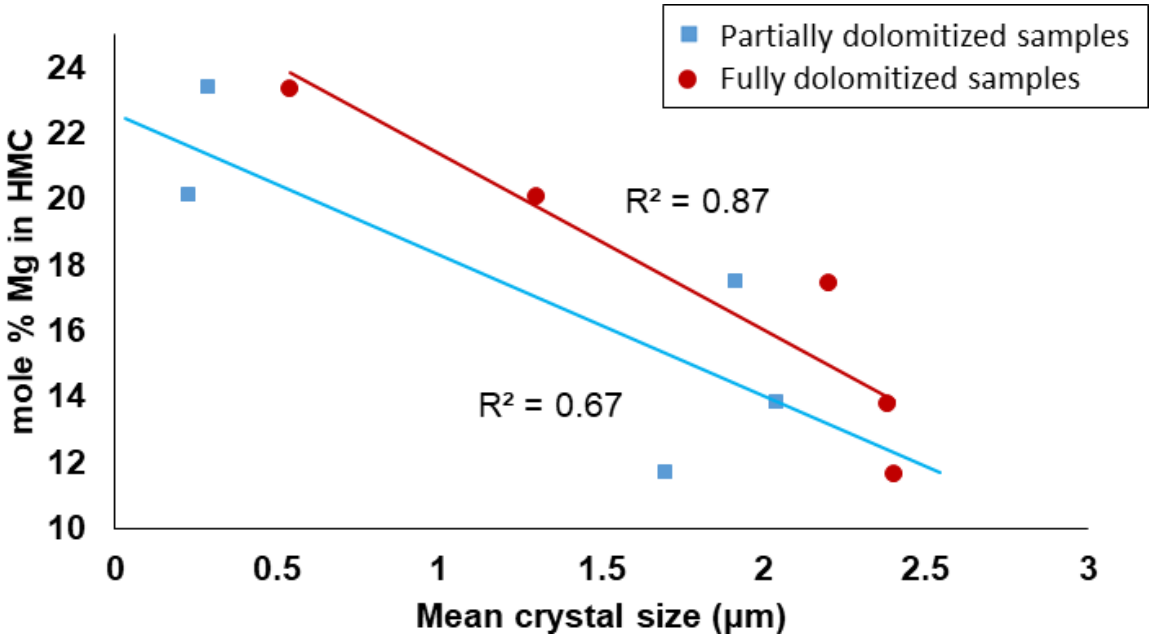

Figure 2-14: Cross plot of mean crystal size against initial bulk mole % Mg in HMC reactant for partially dolomitized and fully dolomitized samples with associated trendlines.

2.5.3. Implications for dolomitization in the Neogene

Our results suggest that the magnesium content in HMC allochems is a minor factor on the rate of dolomitization, compared to other factors such as microstructure, fluid temperature, fluid composition and organic material. This is consistent with findings from previous studies on the aforementioned factors (Gaines 1980; Bullen and Sibley 1984; Kaczmarek and Sibley 2011; Cohen and Kaczmarek 2017; Kaczmarek and Thornton 2017). In the context of ancient dolomites, the rate of dolomitization may be linked to the sequence of dolomitization of different allochems; wherein allochems that are dolomitized faster would be preferentially dolomitized in the rock record. Taken as a whole, our observations suggest that the documented link between coralline red algae

and global dolomitization events in the Neogene (Laya et al., 2018) is likely not a result of increased availability of Mg from HMC, but more likely a result of biological changes (species-dependent, with microstructure prone to dolomitization), climatic changes, or geochemical changes which affects the factors mentioned above. Another implication of our findings is that they emphasize the need to consider the diagenetic and environmental contexts, such as the species make-up of the allochems and the timing of HMC dolomitization, when interpreting natural case studies involving preferential dolomitization.

Preferential dolomitization of HMC in the geological record has been attributed to several factors. HMC skeletal grains, such as coralline red algae and foraminifera, are typically cryptocrystalline; the numerous sub-micrometer crystallites within their microstructures (Auer and Piller 2020) may provide a higher density of nucleation sites for dolomite than other allochems. Fluid Mg/Ca ratio may also be higher immediately surrounding HMC bioclasts than it is in the bulk fluid. This might be the case for *Goniolithon spp.* especially under conditions where low fluid fluxes are maintained, thereby promoting localized dolomitization within HMC skeletal grains. Land and Epstein (1970) attributed the selective dolomitization of the coralline red algae in the unusually unaltered Late Pleistocene limestone successions in to magnesium concentration build up in the surrounding pore fluids. Similarly, Miocene successions in Egypt also display selective dolomitization in coralline algae (Fig. 6a, Mansour and Abd-Ellatif 2013), but here it was inferred that the cryptocrystalline nature of the coralline algae provided more numerous nucleation sites that subsequently provided a

locally more favorable dolomitization environment for pulses of marginally dolomite supersaturated fluids (Mansour and Abd-Ellatif 2013), consistent with the finding of this study.

In contrast, HMC have also been observed to be among the last to be dolomitized under different conditions. In this case, the HMC allochems may have stabilized to LMC before any dolomitization occurs due to early freshwater diagenesis (Kocurko 1979). Low-Mg calcite (LMC) has been consistently shown to dolomitize at a slower rate than HMC and aragonite (Land 1967; Matthews and Katz 1977; Baker and Kastner 1981; Rose and Kaczmarek 2019). For example, the variably dolomitized Pleistocene "algal limestones" in San Andres, Colombia, show evidence of stabilization to LMC before dolomitization (Kocurko 1979). In those successions, there are partially dolomitized facies where coralline red algae and foraminifera bioclasts are undolomitized, but the surrounding matrix is dolomitized. Similar observations have also been reported in other Neogene carbonates (e.g., Ward and Halley 1985).

2.5.4. Diagenetic paths to selective dolomitization

Based on our observations and previous studies, we propose a conceptual model which summarizes the sequence of diagenetic events that is required for selective dolomitization of HMC (**Fig. 2-15**). Selective dolomitization of HMC occurs only under specific diagenetic and environmental conditions. It is mostly independent of the Mg content of the precursor when HMC concentrations are above a particular threshold (~14 mole% $MgCO_3$). Take the case of calcareous algae with >14 mole% $MgCO_3$. Shortly

after deposition, the onset of conditions conducive to dolomitization should occur prior to any substantial calcite stabilization of the sediments. Under conditions of very low fluid flux or diffusion dominant systems (equivalent or lower fluid to rock ratios), the calcareous algae will likely be preferentially dolomitized due to locally higher dolomite saturation and more available active sites as evidenced from the previously discussed observations by Land and Epstein (1970). Alternatively, under conditions of high fluid flux or advective transport dominant systems, if conditions are only marginal for dolomitization, however, HMC may still be selectively dolomitized as evidenced from the earlier described observations by Mansour and Abd-Ellatif (2013). In another alternative scenario, foraminifera with >14 mole% $MgCO_3$ is deposited, there is a significant period of time between the deposition of the foraminifera with the onset of conditions conducive to dolomitization, allowing for stabilization of the HMC skeleton to LMC and for the microstructure to subsequently coarsen, as evidenced from observations by Kocurko (1979) and Ward and Halley (1985). Once conditions for dolomitization are in place, the foraminifera will not be selectively dolomitized.

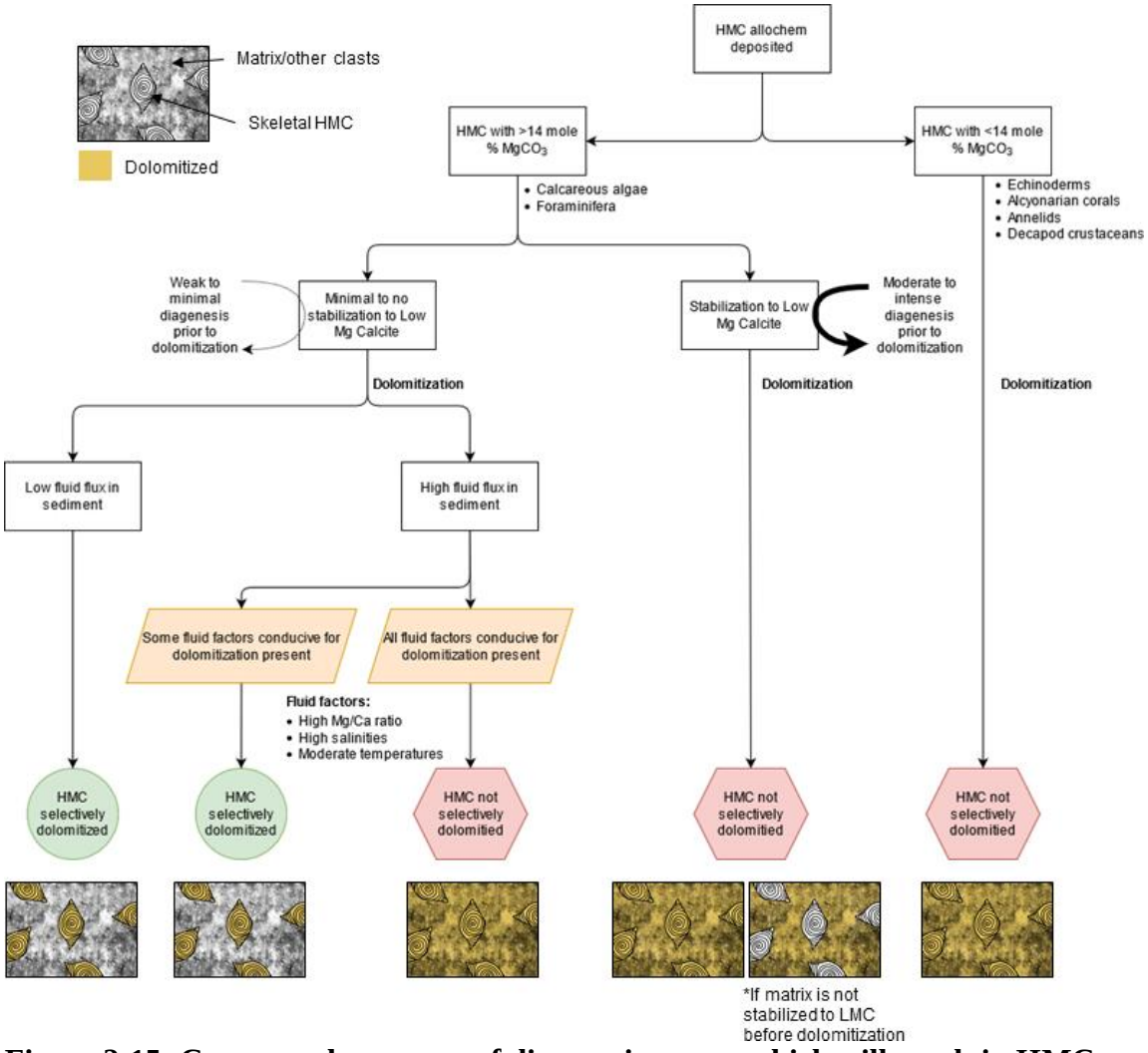

Figure 2-15: Conceptual sequence of diagenetic events which will result in HMC being selectively dolomitized and contrasting scenarios which do not selectively dolomitize HMC.

2.6. Conclusions

Results of high-temperature dolomite synthesis experiments demonstrate that the Mg concentration in biogenic HMC does not correlate with rate of dolomitization, induction period, or the stoichiometry of dolomite products except in specific cases. *Goniolithon* bioclasts appear to be exceptionally effective at liberating Mg-ions into

solution relative to other skeletal HMC grains. The data suggest that contrary to our assumptions, the concentration of Mg in skeletal HMC is not a good predictor of dolomitization rates. Rather, reactant microstructure appears to influence reaction rates to a higher degree in these highly controlled experiments. Other factors including, fluid temperature, fluid composition, organic material, have also been shown to influence laboratory dolomitization rates, but the relative contributions of each is still unclear. Our observations on dolomite texture are consistent with previous studies, wherein skeletal HMC reactant consistently yield fine crystalline mimetic dolomite that retains their original reactant microstructure. This study also provides context and describes the specific diagenetic and environmental conditions, namely preservation of HMC immediately prior to dolomitization, in which selective dolomitization of HMC could occur.

3. PREFERENTIAL DOLOMITIZATION IN MIO-PLIOCENE BIOCLASTIC CLINOFORMS ON BONAIRE ISLAND, SOUTH CARIBBEAN: INSIGHTS FROM PETROGRAPHIC AND GEOCHEMICAL ANALYSES

3.1. Synopsis

Dolomitization is defined as the replacement of calcium carbonate components (matrix or grains) for dolomite in a dissolution-precipitation process. During this process, selective dolomitization can occur; however, how and why this selectivity occurs is still in debate. Selective dolomitization can be significant in the overall dynamic of the global Mg cycle, since some rock components tend to be preferentially dolomitized; therefore, the abundance of those component can modify the magnesium balance between the ocean and sediments disrupting the cycles in certain geological times. This process can be related to the apparent correlation between global dolomitization events in the Neogene and the synchronous rise in species abundance of coralline red algae, but the underlying issue remains unclear. In the Caribbean islands, excellent examples of Neogene partially dolomitized carbonates containing coralline red algal facies have been described. These strata provide an opportunity to analyze in detail preferential dolomitization. This study attempts to understand selective dolomitization of different component (grains and matrix) especially red algal material by examining the well-preserved outcrop of partially dolomitized Mio-Pliocene succession called “Seru Grandi” in Bonaire Island, The Caribbean.

We assess the degree and timing of selective dolomitization of various carbonate components using petrographical and geochemical methods. We observe the micrite matrix is dolomitized first, followed by coralline red algae bioclasts, and subsequently all other allochems such as bivalves and echinoderms. In several cases, dolomite crystals appear to originate from within and surrounding coralline algae fragments, suggesting that dolomitization could have initiated from internally sourced magnesium of the coralline red algae's high-magnesium calcite skeleton. Collectively, our observations suggest that selective dolomitization is controlled primarily by reactive surface area of the carbonate component but is less clear if there is a dependency on mineralogy. Our observations also support a link between Neogene global dolomitization events and the rise in CRA species abundance within the same period. In addition, we document a more complex paragenetic sequence for the Seru Grandi clinoforms than previously known, with distinct differences in diagenetic effects between updip and downdip strata which demonstrates that detailed analyses of individual carbonate components can provide a more complete picture of the diagenetic history in carbonate successions in the Caribbean.

3.2. Introduction

Dolomitization is a diagenetic phenomenon wherein carbonate minerals such as calcite and aragonite are replace into dolomite through a dissolution-precipitation reaction (Machel 2004). Despite its ubiquity throughout the geologic record, there is still much controversy surrounding the process and its effects (Warren 2000; Machel 2004;

Kaczmarek et al. 2017; Petrash et al. 2017). One controversy is the occurrence of selective dolomitization, a process wherein a particular group of allochems is dolomitized whereas others are not in a partially dolomitized carbonate succession (Schlanger 1957; Buchbinder and Friedman 1970; Land and Epstein 1970; Kocurko 1979; Mansour and Abd-Ellatif 2013). Common among all models of dolomitization are the fundamental requirements for this process to occur: 1) A source of magnesium; 2) presence of calcite or aragonite; and 3) presence of hydrological gradients which allow for sufficient replenishment of Mg reactants and removal of Ca products (Adams and Rhodes 1960; Morrow 1982; Land 1985; Warren 2000; Whitaker et al. 2004). High-magnesium calcite (HMC) can be significant as it can potentially satisfy the first two requirements in and of itself as suggested for local dolomitization in deep water sediments (Swart 1993; Dix 1997; Swart and Melim 2000)

High Mg calcite (HMC) is commonly a constituent of calcareous skeletons, with lesser amounts formed as cements and ooids in marine environments (Morse and Mackenzie 1990). Among bioclasts which form biogenic HMC, coralline red algae forms skeletons with the highest concentrations of Mg contain (Morse and Mackenzie 1990), with Mg concentrations ranging from 10 - 30 mol% Mg (Chave 1952; 1954). As dolomitization happens via a dissolution-precipitation reaction (Machel 2004), Changes in reactant stability will affect the equilibrium state of the reaction by increasing or decreasing the availability of reactant ions (such as Mg^{2+} and CO_3^{2-}). HMC's stability decreases as magnesium content increases (Walter 1985). This in turn, can affect how

quickly dolomitization proceeds by changing the saturation state of dolomitization (Morse and Mackenzie 1990).

As dolomitization happens via a dissolution-precipitation reaction (Machel 2004), Changes in reactant stability will affect the equilibrium state of the reaction by increasing or decreasing the availability of reactant ions (such as Mg^{2+} and CO_3^{2-}). This in turn, can affect how quickly dolomitization proceeds by changing the saturation state of dolomitization. As an example, Kaczmarek and Sibley (2014) demonstrated this difference in dolomitization rate in laboratory experiments, where the more stable LMC reactant dolomitized more slower than aragonite reactant.

Similarly, as dolomitization is also a strongly kinetically controlled reaction, changes in reactive surface area can also change the rate at which dolomitization occurs (Sibley et al. 1987; Arvidson and Mackenzie 1999). Larger reactive surface areas will lead to faster rates of dolomitization (Sibley et al. 1987; Al-Helal et al. 2012; Budd and Park 2018; 2019). Thus, allochems which are very fine or cryptocrystalline in structure (and thus presents high surface area to volume ratio) such as in coralline red algae (Auer and Piller 2020) would be expected to preferentially dolomitize relative to other allochems . This preferential dolomitization of coralline red algae has been demonstrated by field studies such as by Mansour and Abd-Ellatif (2013), in laboratory settings as by Bullen and Sibley (1984), and also via reactive transport modelling as by Al-Helal et al. (2012).

Partially dolomitized carbonates with a variety of allochem mineralogies and microstructures display a relative timing of dolomitization between every component.

We can make initial assumptions such as High-Mg calcite should consistently be the first to be selectively dolomitized under most surface conditions, particularly for coralline red algae, due to high contain of Mg in its skeleton. However, the few studies that specifically mention dolomite selectivity do not come to coherent conclusions. However, the few studies that specifically mention dolomite selectivity do not come to the same conclusions. While there appears to be abundant examples of HMC allochems being more commonly dolomitized (Schlanger 1957; Land 1967; Land and Epstein 1970; Bullen and Sibley 1984; Saller 1984; Mansour and Abd-Ellatif 2013), there are multiple studies wherein HMC allochems are not preferentially dolomitized (Buchbinder 1979; Kocurko 1979; Ward and Halley 1985; Lucia and Major 1994a). Additionally, the Miocene saw a peak in coralline red algae species richness (Aguirre et al. 2000; Halfar and Mutti 2005) and a high abundance of dolomitization (Budd 1997b) in deposits that host these coralline red algae. Thus, a possible link has been suggested between these two trends (Laya et al. 2018c), which thus makes it relevant to investigate if these HMC bioclasts have some influence on the abundance of dolomite and if there is any preference for coralline red algae to be dolomitized before other components.

This brings us to this study's research question: *Are HMC bioclasts preferentially dolomitized?* To answer this question, we assess selective dolomitization of various carbonate components (matrix and allochems) using petrographical and geochemical methods in a Miocene succession on the island of Bonaire, The Netherlands. The outcrop, "Seru Grandi", hosts excellent exposures of partially dolomitized clinoforms

with abundant HMC skeletal grains, and multiple dolomitization fronts (Laya et al. 2021; Teoh et al. in review)

3.2.1. Geological Background

The semi-arid island of Bonaire contains abundant and well documented examples of early dolomitization (Deffeyes et al. 1965a; Sibley 1980; Budd and Mathias 2015). It is located 80 kilometers north of the Venezuelan coast and is largely low lying with a maximum elevation of 241 m above sea level (**Fig. 3-1**). Bonaire's geology can be broadly divided into five geological units: 1) Cretaceous volcanic basement (Washikemba Formation) formed of deformed volcanic rocks; 2) Eocene sandstones and siltstones (Soebi Blanco Formation); 3) Miocene-Pliocene carbonates (Seroe Domi Formation), 4) Pleistocene shallow-marine reefal carbonates, (no formal lithostratigraphic name), and 5) reefal and evaporitic deposits within Holocene-Recent hypersaline lakes (no formal lithostratigraphic name) (Alexander 1961; Deffeyes et al. 1965a; Bandoian and Murray 1974; Zapata et al. 2014; Laya et al. 2018a; Laya et al. 2021).

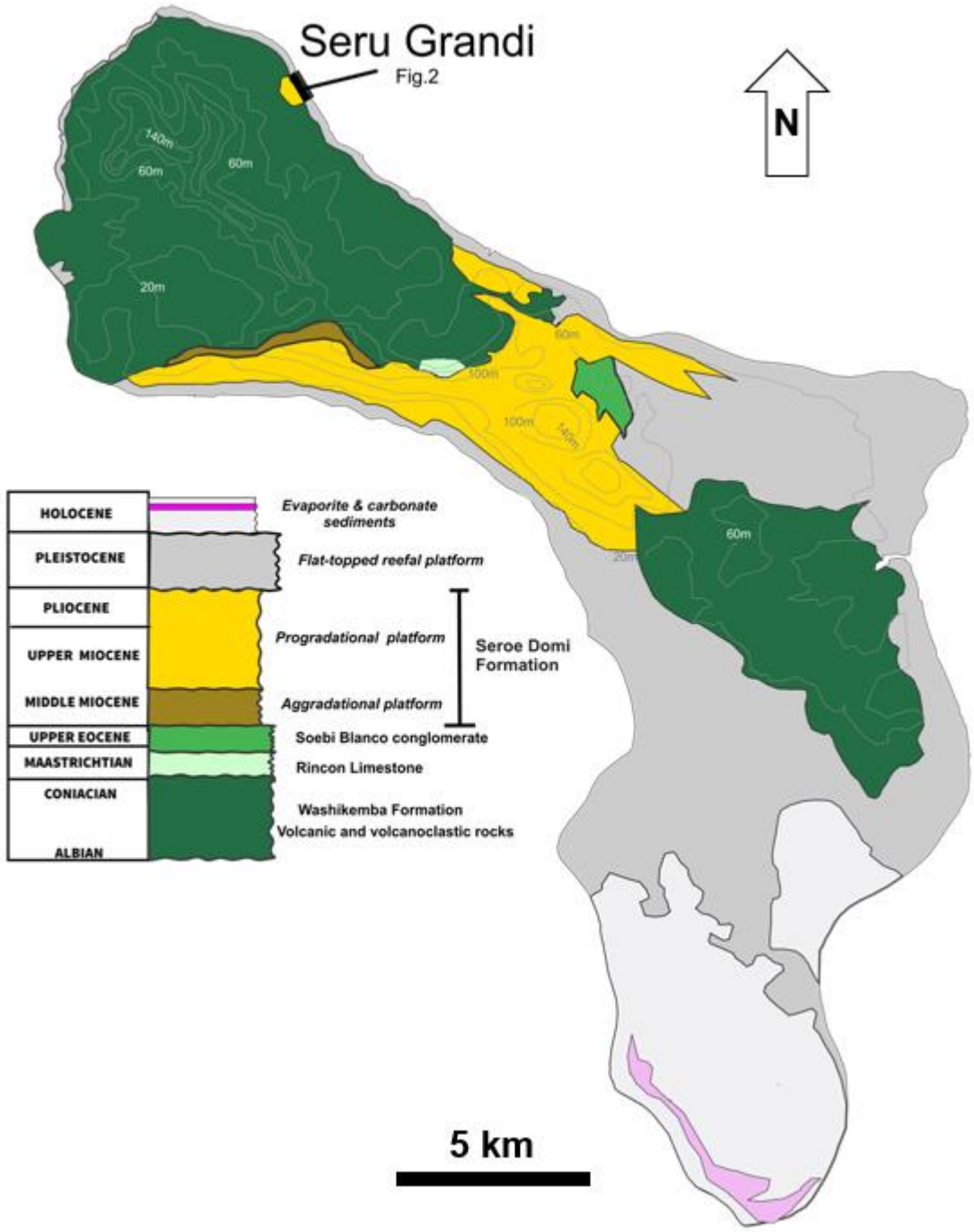

Figure 3-1: Simplified geological map and overall stratigraphy of Bonaire, with location of Seru Grandi outcrop highlighted.

The Seru Grandi outcrop is located in Washington-Slagbai National Park on the northeastern side of the island (**Fig. 3-1**). The Seru Grandi outcrop is part of The Seroe Domi Formation and consists of a Mio-Pliocene succession of partially dolomitized shallow-water carbonate clinoform deposits, offlapping a complex volcanic basement (Laya et al., 2018). It is overlain unconformably by Pleistocene structure-less reefal facies formed of calcitic coral rudstone with red algal encrustations. The Mio-Pliocene clinoforms of the Upper Seroe Domi Formation are the focus of this study and are composed primarily of coralline red algae with minor coral fragments, large benthic foraminifera, echinoids, rare bivalves, and volcanic lithic clasts. Sedimentation in the clinoforms occurred mostly in the oligophotic zone and slightly deeper water close to the platform margin (Laya et al., 2018) during a highstand phase. Four primary facies are described for these clinoforms (Laya et al., 2018): 1) large benthic foraminiferal grainstone; 2) coralgal grain/packstone; 3) encrusting red algae-rich and rhodolite grainstone/packstone, and 4) reworked red algal grain/packstone. No clear facies boundaries can be discerned; facies boundaries are characterized by gradational transitions, broadly from encrusting red algae facies updip towards bioclastic dominant facies downdip. Updip refers to the upper half sediments of an individual clinoform, whereas downdip refers to the lower half of an individual clinoform (**Fig. 3-2**). Updip is defined as the upper half of an individual clinoform package, whereas downdip is defined as the lower half of an individual clinoform package. Approximately 32 clinoform beds are exposed, with progradation from the northwest to the southeast (Laya et al., 2021).

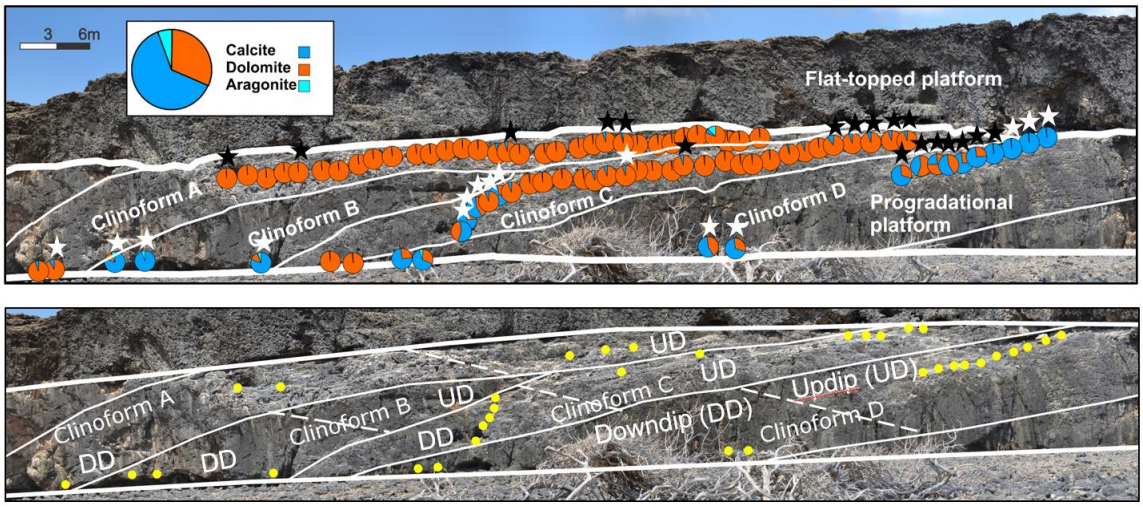

Figure 3-2: A) Panorama of Seru Grandi clinoforms, showing all sampled points, and relevant samples for this study (starred). Pie charts at each point show relative mineralogical abundance of dolomite, calcite, and aragonite of each sample as determined by XRD analyses (Modified from Laya et al. 2021). B) Panorama of Seru Grandi clinoforms, showing relevant sampled points for this study, and definition of what constitutes as updip sediments and downdip sediments (separated by dashed lines) in each clinoform.

Dolomitization of the Seroe Domi Formation is pervasive and displays sharp reaction fronts which tend to conform to individual clinoform surfaces (Laya et al., 2018; Laya et al., 2021). These Miocene-Pliocene dolomites were formed mainly as early replacement dolomite, with variable dolomite abundances in different units (Bandoian and Murray 1974; Sibley 1980; Sibley 1982; Lucia and Major 1994a; Laya et al. 2018a). Four different dolomite textures in Seru Grandi are described, with their primary differences being their mean crystal sizes and optical clarity: 1) Type 1 dolomite (<15 µm); 2) Type 2 dolomite (15-80 µm); 3) Type 3 dolomite (50-100 µm), 4) Type 4 dolomite (>100 µm) (Laya et al., 2021).

3.3. Methods

Fieldwork results and other data from the Seru Grandi outcrop (e.g., petrographic observations, geochemistry, facies scheme and porosity and permeability values) are initially reported in Laya et al. (2018) and Laya et al. (2021). For the present study, only partially dolomitized and select undolomitized and completely dolomitized samples of the Seru Grandi outcrop are analyzed in detail (**Fig. 3-2**).

A total of 35 core plugs were shortlisted from 3 (1-m interval) lateral transects and subsequently reprocessed for thin section petrography, stable isotope geochemistry analysis, and powdered XRD analysis (**Table 3-1**). In addition, full slide thin section images were captured from thin sections using a Nikon 8000 ED slide scanner. Following, detailed petrographic analysis of polished thin sections was conducted using an Olympus BX53MTRF microscope in tandem with Olympus Stream Essentials 2.1. software. Cathodoluminescence (CL) petrography was performed using a Technosyn Cold Cathode Luminescence Model 8200 MKII to determine crystal evolution and dolomite rim evolution. The Dunham (1962) classification scheme as modified by Embry and Klovan (1971) was used to describe and characterize rock textures. In-depth descriptions of facies and carbonate components are documented in Laya et al., (2018). Alizarin-red staining was used to identify dolomitized and undolomitized allochems within thin sections.

Table 3-1: Mineralogies as derived from XRD analysis and bulk stable isotope geochemistry for all selected samples.

Sample	$\delta^{13}C$ (VPDB)	$\delta^{18}O$ (VPDB)	Dolomite	Calcite	Aragonite
Line 1 SG_1	1.53	2.25	86.79%	13.21%	0.00%
Line 1 SG_18	0.76	2.09	93.76%	6.24%	0.00%
Line 1 SG_2	0.96	2.48	93.06%	6.94%	0.00%
Line 1 SG_24	0.35	1.94	88.72%	11.28%	0.00%
Line 1 SG_25	1.11	1.97	93.05%	5.91%	1.03%
Line 1 SG_33	-1.89	-0.61	76.16%	23.84%	0.00%
Line 1 SG_34	0.21	1.72	80.91%	19.09%	0.00%
Line 1 SG_35	-0.38	-0.11	45.54%	54.46%	0.00%
Line 1 SG_36	1.45	2.59	94.95%	5.05%	0.00%
Line 1 SG_37	-0.34	-0.29	43.34%	56.66%	0.00%
Line 1 SG_4	1.92	2.65	93.43%	6.57%	0.00%
Line 1 SG_5	1.96	3.18	91.76%	8.24%	0.00%
Line 1 SG_6	1.5	2.9	87.59%	12.41%	0.00%
Line 1 WDG 1_1	-2.8	-3.15	0.40%	57.92%	41.68%
Line 1 WDG_1_0	-6.12	-3.17	5.57%	77.12%	17.31%
Line 1 WDG_1_2	-0.6	-1.77	12.06%	87.94%	0.00%
Line 2 SG_14	3.06	3.65	94.82%	2.20%	2.98%
Line 2 SG_16	2.65	3.69	92.30%	7.70%	0.00%
Line 2 SG_22	1.87	2.51	93.72%	6.28%	0.00%
Line 2 SG_44	-8.58	-2.55	8.77%	75.81%	15.42%
Line 2 SG_45	2.63	3.17	91.41%	8.59%	0.00%
Line 2 SG_6	4.17	2.43	80.63%	6.15%	13.22%
Line 3 SG_1	-0.91	-2.48	2.18%	97.82%	0.00%
Line 3 SG_10	-2.8	-1.41	29.49%	70.51%	0.00%
Line 3 SG_11	0.04	-1.28	34.47%	65.53%	0.00%
Line 3 SG_2	-1.76	-1.93	0.34%	99.66%	0.00%
Line 3 SG_3	-1.08	-1.48	0.40%	99.60%	0.00%
Line 3 SG_4	-1.31	-1.93	0.31%	99.69%	0.00%
Line 3 SG_5	-0.22	-0.98	20.33%	79.67%	0.00%
Line 3 SG_6	-0.58	-1.22	11.67%	88.33%	0.00%
Line 3 SG_7	-1.44	-1.11	37.71%	62.29%	0.00%
Line 3 SG_8	0.75	1.86	77.47%	22.53%	0.00%
Line 3 SG_9	0.00	0.34	52.65%	47.35%	0.00%
Line 3 WDG_3_1	-2.03	-2.71	30.53%	61.58%	7.89%
Line 3 WDG_3_2	-2.52	-2.15	23.46%	76.54%	0.00%

Quantification of the selectivity of dolomitization within a sample was conducted using standard point counting techniques on samples stained by Alizarin-Red (Flügel 2004). 300 randomized points were observed and classified for each sample using JMicrovision 1.3.3. The following classes were used: 1) Dolomitized coralline red algae; 2) dolomitized other allochem; 3) dolomitized matrix; 4) undolomitized coralline red algae; 5) undolomitized other allochem; 6) undolomitized matrix. Due to the difficulty in discerning the matrix from very fine drusy calcite cements, no distinction is made between the two when point counting. Whether a component is considered selectively dolomitized is determined by the normalized difference between the dolomitized class and the same undolomitized class, which we will define as "Selectivity" and is obtained by the following equation:

$$Selectivity\ (\%) = \frac{(A_{Dolomitized} - A_{Undolomitized})}{(A_{Dolomitized} + A_{Undolomitized})} \times 100$$

Where $A_{Dolomitized}$ represents the proportion of the dolomitized class, and $A_{Undolomitized}$ represents the proportion of the same class, but undolomitized.

Negative values indicate component is less likely to be selectively dolomitized, whereas positive values indicate component is more likely to be selectively dolomitized. For example, if a sample has 20% dolomitized coralline red algae, but only 10% undolomitized coralline red algae, the coralline red algae component is considered to have a selectivity of 33% (normalized to the total amount of CRA, which in this example

is 30%, with a difference of 10%). Samples which do not display any selective dolomitization (i.e., are entirely calcitic or entirely dolomitic) are not point counted.

Powdered X-ray Diffraction (XRD) was used to quantify the variation in abundance and the nature of dolomitization within the outcrop. A larger dataset and more thorough analysis of the mineralogy data presented here can be found in Laya et al. (2021). Bulk rock samples were examined using standard powder X-ray diffraction (XRD) analyses in the Carbonate Petrology and Characterization Laboratory at Western Michigan University and in the Department of Soil and Crops at Texas A&M University with Bruker D8 ADVANCE diffractometers (CuKα radiation) collected with a 2θ range of 20° to 60°, a step size of 0.01°. Standard powdered XRD techniques (Goldsmith and Graf 1958) were used to quantify the abundance of aragonite, calcite, and dolomite. Peak positions were calibrated using powdered fluorite (CaF_2) as an internal standard to account for 2θ offsets. Percent dolomite was calculated using the peak intensity ratio method proposed by Royse et al. (1971).

Eighteen core and billet samples obtained from Seru Grandi were identified for additional geochemical analysis. Microsampling of coralline red algae clasts and bulk whole-rock analyses were conducted to obtain oxygen and carbon stable isotopes; 100 - 200 micrograms of powder were collected in triplicate using a dental drill on specifically coralline red algae clasts. In bulk whole-rock analyses, a portion of the core sample is cut and crushed in an agate mortar and pestle. Measurement were carried out in the Geosciences Stable Isotope Facility at Texas A&M University using a ThermoFisher Scientific Kiel IV Carbonate device coupled to a MAT 253 isotope ratio mass

spectrometer to obtain $\delta^{13}C$ and $\delta^{18}O$ measurements relative to Pee Dee Belemnite (VPDB) with an analytical precision of 0.04‰ for $\delta^{13}C$ and 0.08‰ for $\delta^{18}O$.

Samples were analyzed for calcium (Ca), magnesium (Mg), and strontium (Sr) by a Laser-Ablation Inductively Coupled Plasma Mass Spectrometer (LA-ICP-MS) in the Radiogenic Isotope Geosciences Laboratory at Texas A&M University. Specifically, both dolomitized and undolomitized CRA, micritic matrix, and cements were targeted for sampling. High purity argon and helium were used as carrier gasses. NIST 610, NIST 612, and MACS-3 standards were use as references and for calibration of instrument. Raw data reduction was completed using Iolite software (Paton et al. 2011). Results are reported in parts per million (ppm) and in moles (Supplementary Table 2).

3.4. Results

3.4.1. Facies and component descriptions

The Seru Grandi clinoforms consist broadly of grainstone and packstone facies that are dominated by coralline red algae (CRA) as the allochem component. Two forms of CRA are observed, encrusting and bioclastic CRA. Encrusting CRA (**Fig. 3-3 A**) are observed within updip sections of the clinoforms, and consist of different taxa which include *Sporolithon sp., Spongites sp., Lithothamnion sp., and Neogoniolithon sp.*. Bioclastic CRA (**Fig. 3-3 B, C**) are observed within downdip sections of the clinoforms, with similar taxa as that observed in encrusting CRA, but with more abundant branching forms in varying degrees of fragmentation and abrasion. Minor amounts of other allochems include large benthic foraminifera, coral fragments, echinoid fragments, and rare brachiopods, gastropods, and bivalves are present in the succession. Carbonate mud is observed filling the intergranular pore spaces as a matrix component. A more detailed description of the facies mentioned here can be found in Laya et al. (2018a).

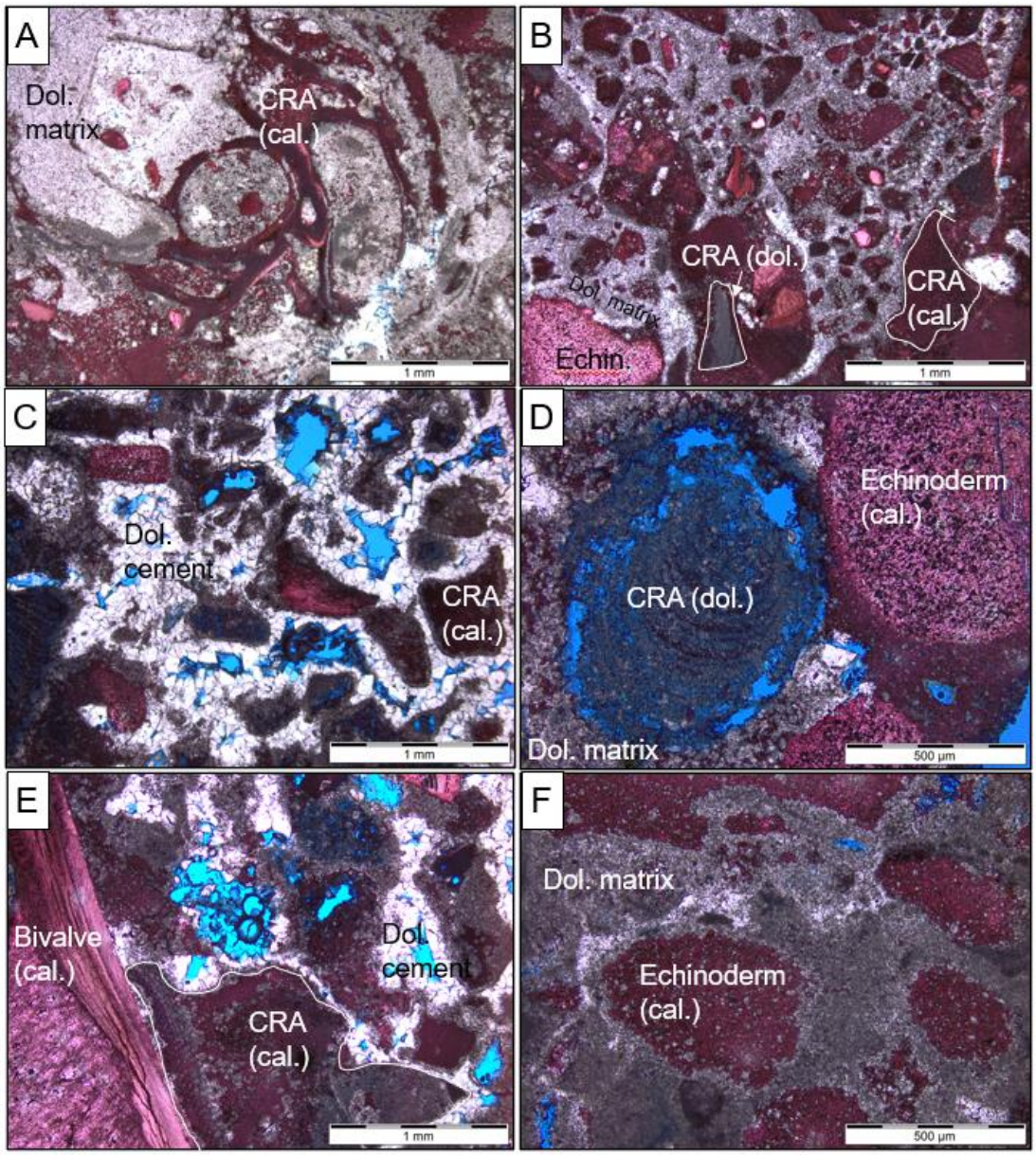

Figure 3-3: Plane polarized microscope sample images of Alizarin-Red stained thin sections showing a wide variety of selective dolomitization examples. (A) Undolomitized coralline red algae (CRA) (red) surrounded by completely dolomitized micrite matrix. (B) Undolomitized CRA (red) and other clasts (Echinoids (Echin) and foraminfera) surrounded by completely dolomitized micrite matrix. Some CRA observed to be dolomitized. (C). Undolomitized CRA (red) and other clasts (Echinoids (Echin.) and foraminfera) surrounded by dolomite cement. (D). Dolomitized coralline red algae surrounded by dolomitized matrix next to undolomitized echinoderm. (E) Variably dolomitized CRA and undolomitized bivalve within a dolomitized matrix. (F) Undolomitized echinoderms (red) surrounded by a matrix of dolomitized micrite matrix.

3.4.2. Replacement dolomite

For this study we used the dolomite types defined previously by Laya et al. (2021). Dolomite occurs abundantly in the Type 1 form (<15 μm), with anhedral crystal boundaries, as mimetic replacement of formerly HMC skeletal grains such as benthic foraminifera, coralline red algae, and echinoids. Replacement of the muddy micritic matrix also results in Type 1 dolomite. Type 2 dolomites (15–80 μm), with subhedral habits and minimal zonation, can also be observed interspaced within bioclasts and matrix components. Origination of dolomite crystals within each allochem varies according to allochem type. In CRA, small (<20 μm) dolomite crystals are often observed to precipitate from within the cores of CRA, rather than from the periphery of CRA allochems (**Fig. 3-4 A, B, D**). This is in contrast with the micritic matrix, which often displays a gradient of dolomite crystal densities which appear to run from one part of the thin section to the other (**Fig. 3-4 C**). In some cases, a gradient of dolomite crystal densities can be observed to emanate from CRA allochems (**Fig. 3-4 E**).

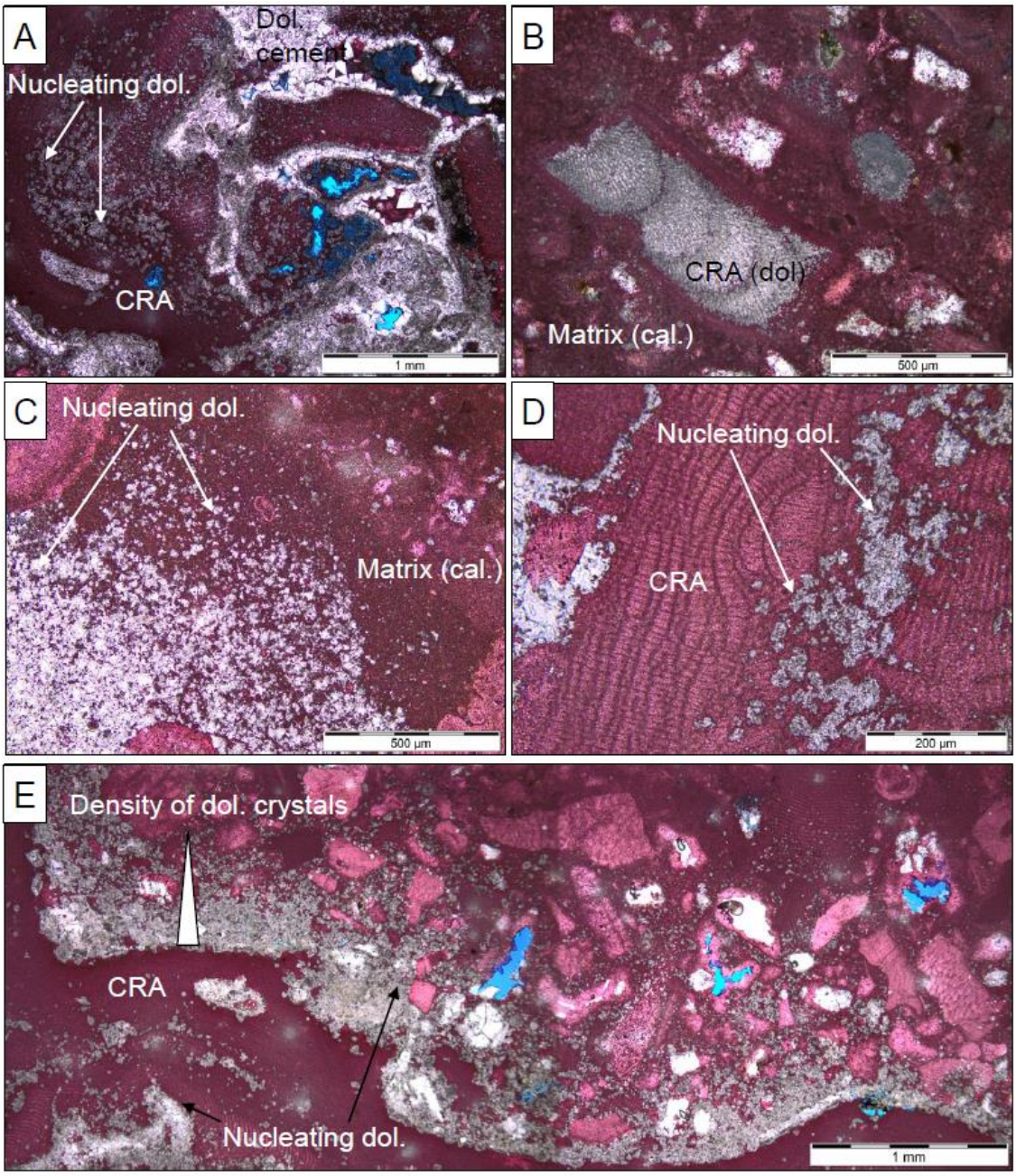

Figure 3-4: Plane polarized microscope sample images of Alizarin-Red stained thin sections showing variations in how dolomite crystals nucleate in coralline red algae (CRA) and in the micritic matrix. (A)(B) Dolomite crystals nucleating from within CRA clasts and gradually radiating outwards. (C) Dolomite crystals nucleating within micrite matrix, with a crystal density gradient from bottom left to bottom right of image. (D) Close up of nucleating dolomite crystals within CRA, showing an increasing density of dolomite crystals in micrite matrix with increasing proximity to coralline red algae grain.

3.4.3. Cements and other diagenetic features

Bladed cements occur as overgrowth rims ranging from 50 to 100 μm on allochem fragments. Drusy cements are often observed as finer (10 μm – 60 μm) than bladed cements, and fill the intergranular pore, intragranular pores (as in coral cavities) and moldic pores where available. Stalagtitic cements of 40 – 80 μm are occasionally observed primarily within moldic pores. Moldic pores are common and appear to formerly contain benthic foraminifera and coralline red algae based on observations of partially dissolution of those bioclasts. These partially dissolved bioclasts also contain abundant micropores ranging in size from 5 – 100 μm.

Cements show distinct differences between updip and downdip sediments (**Fig. 3-5**). Specifically, cements within updip sediments are commonly euhedral to subhedral dolomite (Type 4), 100 - 400 μm in size, with little to no calcite cements (**Fig. 3-5 A, B**). Within downdip sediments, cements are a mix of calcite and dolomite cements (Type 3), displaying anhedral to subhedral habits, and usually <50 μm in size. Calcite often occurs as drusy spar filling voids. Under CL, updip samples with large euhedral dolomite cements show 5 - 7 alternating luminescent and dark bands within individual dolomite crystals (**Fig. 3-6**). Downdip dolomite cements were too small to properly observe any variations in dark and light bands under CL. In several samples, all dolomite observed within a thin-section is in the form of pore-filling cements, particularly within downdip sections, with minimal to no dolomite observed (<5% based on point counting observations) within the micritic matrix or any other allochems. Within the same section

updip, where no dolomitization is observed, poorly formed calcite cements can be observed (**Fig. 3-7**).

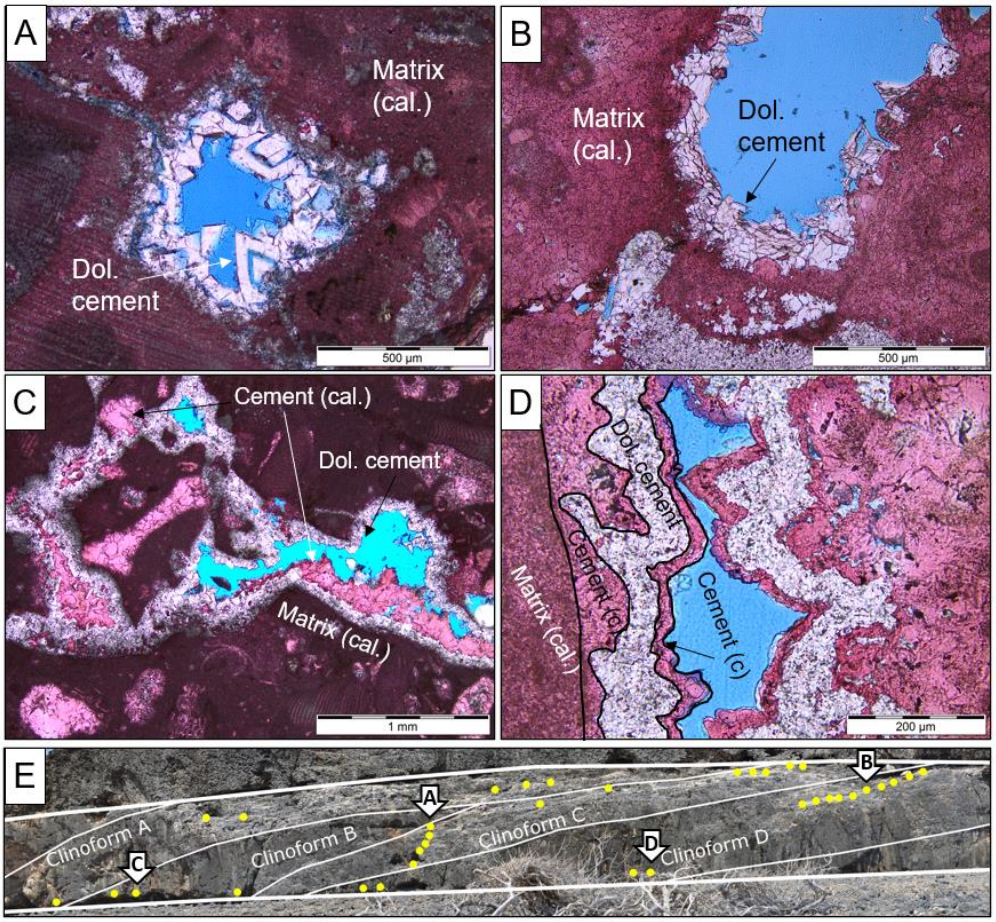

Figure 3-5: Plane polarized microscope sample images of Alizarin-Red stained thin sections showing variations in cement mineralogy and relationships between updip (A, B) and downdip (C, D) section. (A) Close up view of euhedral dolomite cements growing within a pore surrounded by calcitic matrix. Note the occurrence of visible "gap" within dolomite (dol.) cement, likely indicating multiple growth stages. (B) Close up of subhedral dolomite (dol) cement growing within a pore surrounded by calcitic matrix. (C) Close up of anhedral dolomite (dol.) and calcite (cal.) cements growing within a pore surrounded by calcitic matrix. Calcite cement appears to grow after dolomite cements. (D) View of anhedral dolomite (dol.) and calcite (cal.) cements growing within a pore surrounded by calcitic matrix. Note the multi-stage growth of dolomite and calcite. (E) Overview of clinoforms and sampled locations, with arrows indicating location of each thin section photo (A, B, C, D) on clinoform indicated.

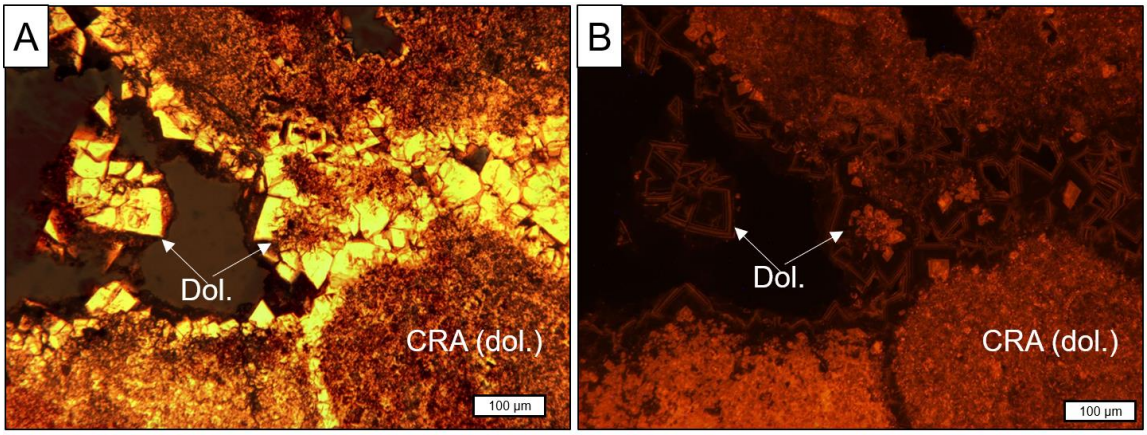

Figure 3-6: Thin section image of dolomitized sample. (A) Plane-polarized image showing extensive replacement dolomite (dol.) within coralline red algae (CRA) clasts with overgrowths of dolomite cement. (B) CL image of (A) showing the luminescent nature of replacement dolomite and alternating luminescent and dark bands within the dolomite cement overgrowths.

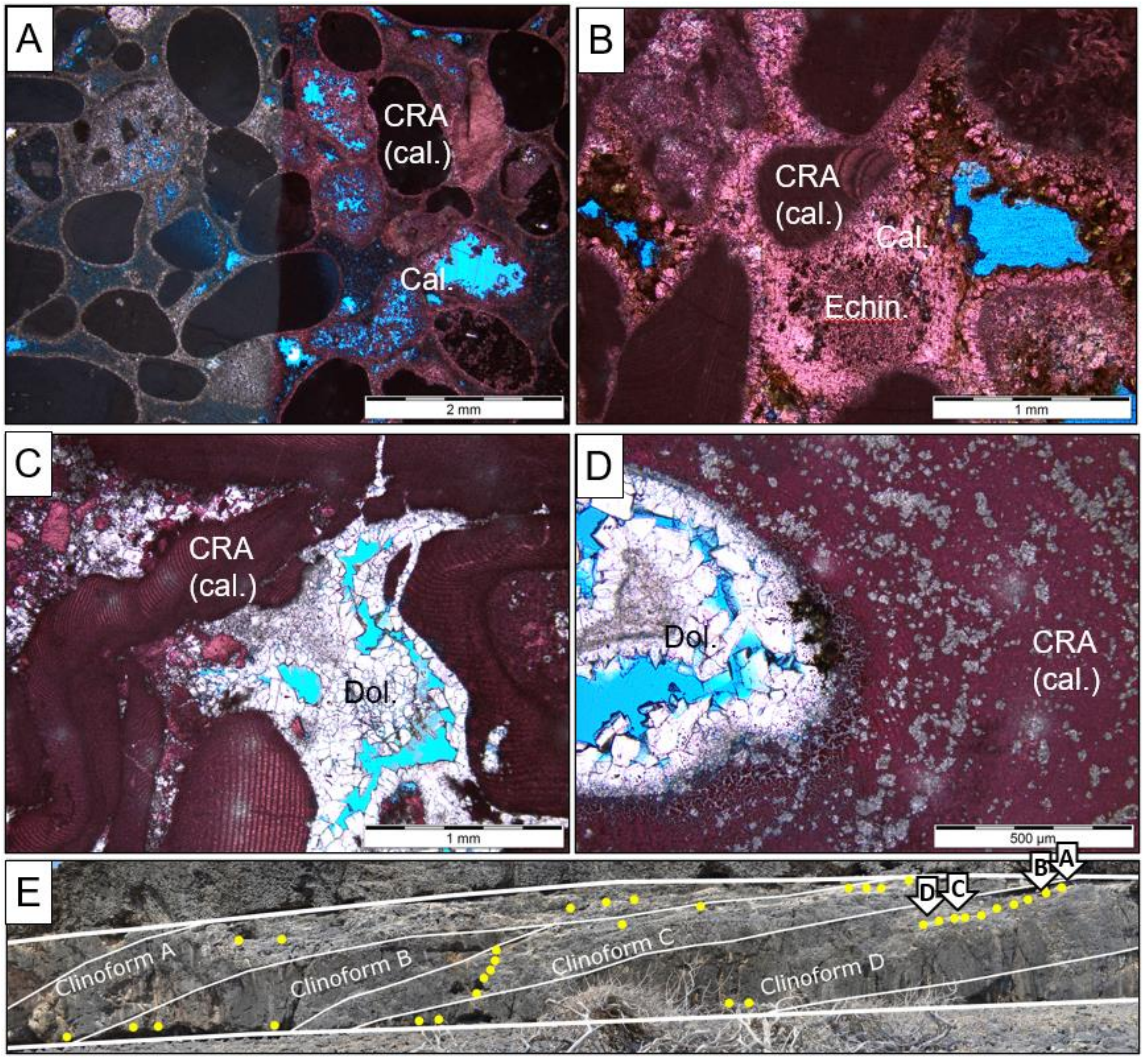

Figure 3-7: Plane polarized microscope sample images of Alizarin-Red stained thin sections showing variations in cement mineralogy updip (A, B) and downdip (C, D) section. (A) View of undolomitized coralline red algae with several moldic pores that have been filled in with calcite cements. (B) View of undolomitized coralline red algae (CRA) and echinoderms (Echin.) surrounded by calcite cements and neomorphosed micrite. (C) View of undolomitized coralline red algae with intergranular pores filled with dolomite cements. (D). View of undolomitized coralline red algae with the beginnings of dolomite nucleating within, and a pore space filled within dolomite cement. (E) Overview of clinoforms and sampled locations, with arrows indicating location of each thin section photo (A, B, C, D) on clinoform indicated.

3.4.4. Quantification of dolomite selectivity

Dolomitized coralline red algae have abundances ranging 0% to 43%, with an average of 13% and standard deviation of 0.14, whereas undolomitized coralline red algae have abundances ranging from 5% to 58%, with an average of 30% and standard deviation of 0.18. Dolomitized matrix have abundances ranging from 8% to 40%, with an average of 25% and standard deviation of 0.10, whereas undolomitized matrix have abundances ranging from 3% to 38%, with an average of 17% and standard deviation of 0.08. Dolomitized other allochems (echinoderms, bivalves, coral fragments) have abundances ranging from 0% to 7%, with an average of 1% and standard deviation of 0.02, whereas undolomitized other allochems have abundances ranging from 4% to 31%, with an average of 15% and standard deviation of 0.08 (**Fig. 3-8, Supplementary Table 1**).

Selectivity of partially dolomitized samples show that coralline red algae and other allochems are not preferentially dolomitized on average (-36% and -88% average selectivity), in contrast with the matrix component (17% average selectivity) (**Fig. 3-8**). Coralline red algae show a maximum selectivity of 89% and a minimum selectivity of -100%, with a standard deviation of 0.66. Other allochems show a maximum selectivity of 19% and a minimum selectivity of -100%, with a standard deviation of 0.33. Matrix shows a maximum selectivity of 82% and a minimum of -33%, with a standard deviation of 0.32. Of the 14 samples point counted, the matrix was observed to be selectively dolomitized in 9 samples, while CRA was observed to be selectively dolomitized in 4 samples. Other allochems were not selectively dolomitized.

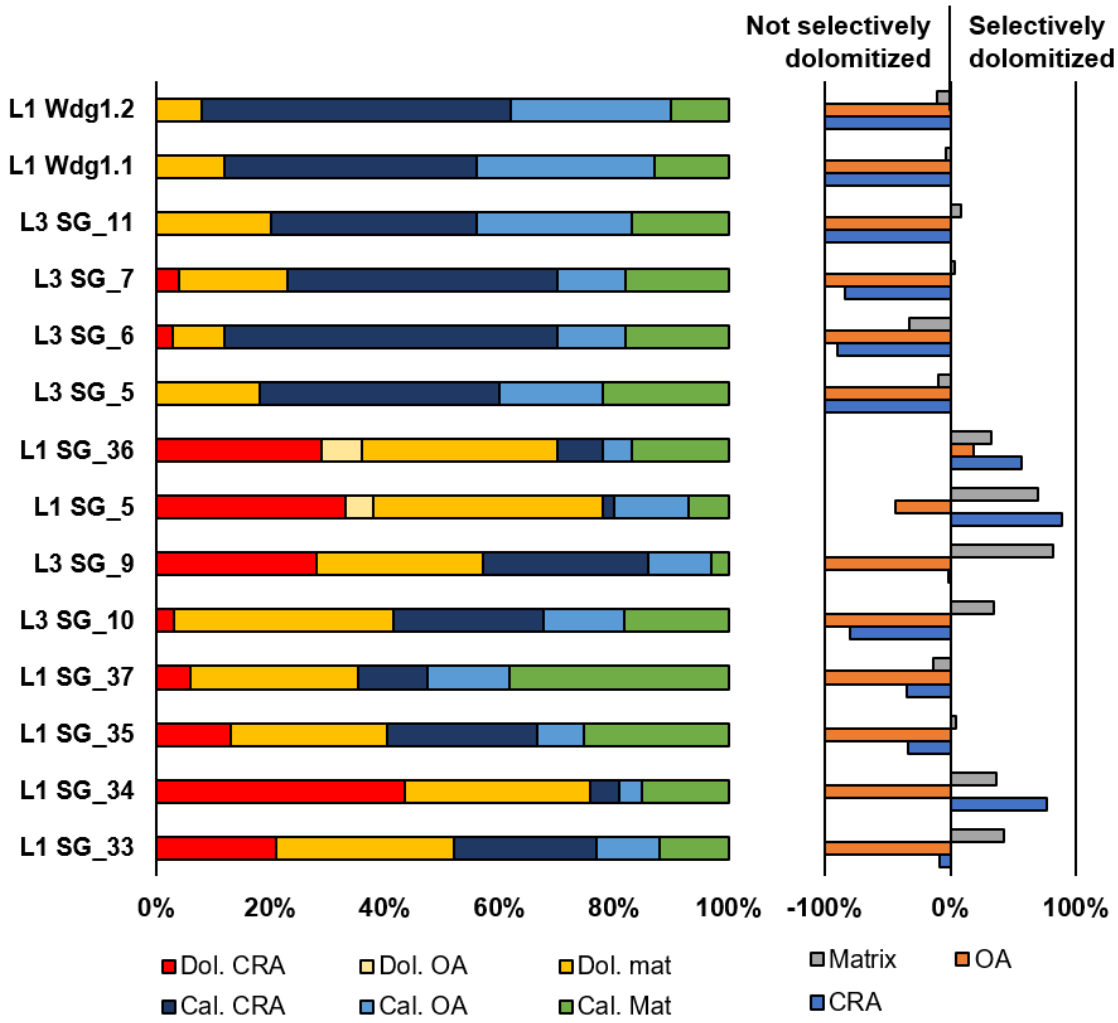

Figure 3-8: Selective dolomitization point counting results, showing relative proportions of dolomitized coralline red algae (Dol. CRA), dolomitized other allochems (Dol. OA), and dolomitized matrix (Dol. Mat) with their undolomitized counterparts (Cal. CRA, Cal. OA, Cal. Mat). A normalized difference for each component is calculated to determine if component is selectively dolomitized, with positive values indicating selective dolomitization and negative values indicating no selective dolomitization.

3.4.5. Stable isotope geochemistry

Stable isotope geochemistry trends for both bulk and coralline red algae are largely similar (**Fig. 3-9**), with $\delta^{18}O$ values averaging at -1.40 ‰ and 2.92‰ for limestone and dolomite CRA samples respectively and -1.91 ‰ and 2.24 ‰ for limestone and dolomite bulk samples, respectively. $\delta^{13}C$ show average values of -0.78‰ and 2.26‰ for limestone and dolomite CRA samples respectively and -1.59 ‰ and 1.47 ‰ for limestone and dolomite samples respectively. $\delta^{18}O$ co-varies with $\delta^{13}C$, particularly at higher $\delta^{18}O$ and $\delta^{13}C$. $\delta^{18}O$ and $\delta^{13}C$ values increases as dolomite abundance increases within the samples (**Fig. 3-9 B, C**)

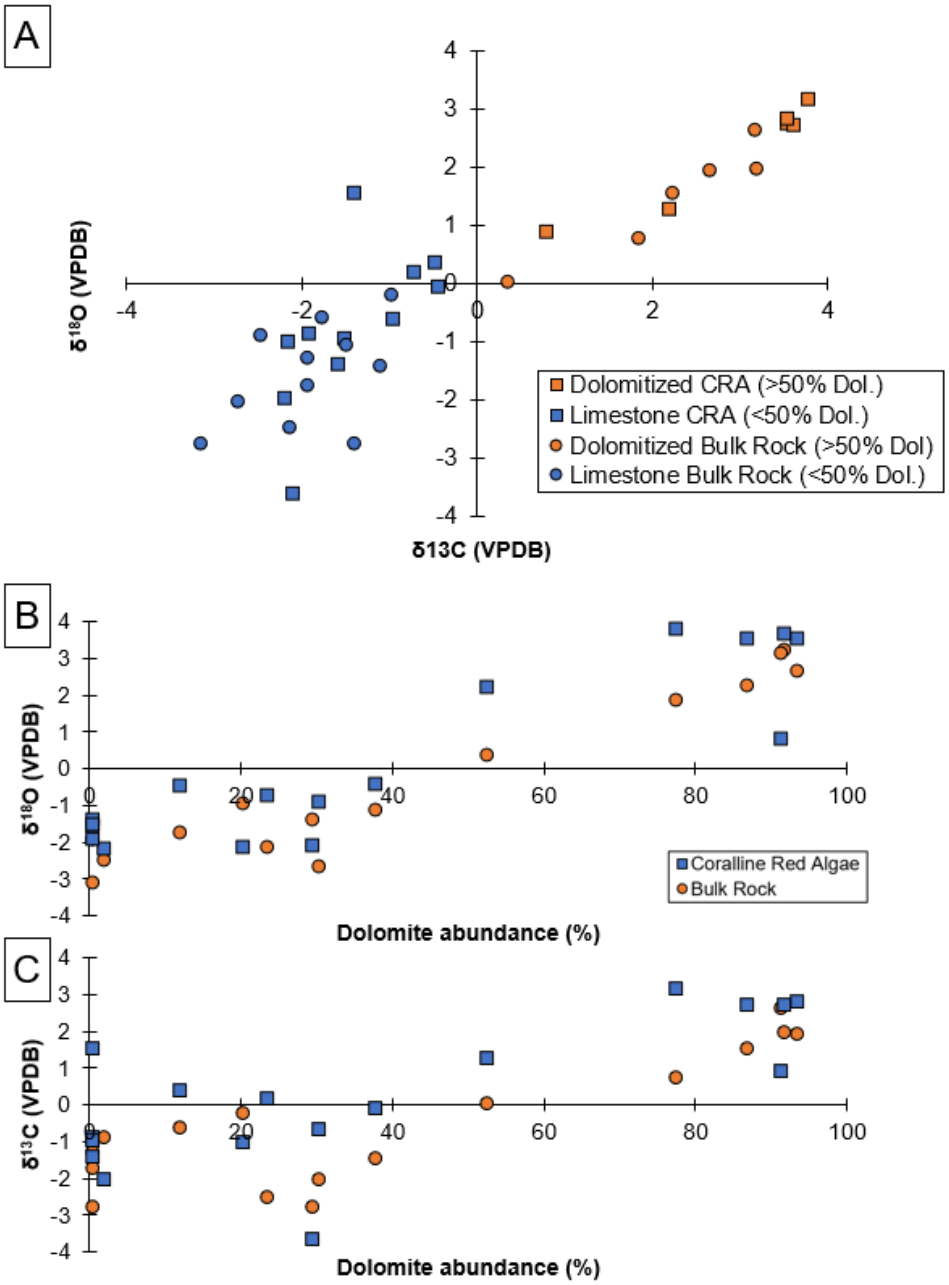

Figure 3-9: $\delta^{13}C$ and $\delta^{18}O$ stable isotope cross-plot for bulk samples (orange and blue circles) and targeted coralline red algae clasts (orange and blue squares), all reported relative to Pee Dee Belemnite (PDB). Both coralline red algae and bulk rock show similar values and trends across all ranges. (A) Crossplot of $\delta^{13}C$ and $\delta^{18}O$ for both bulk samples and coralline algae clasts. (B) Plot of $\delta^{18}O$ and dolomite abundance. Higher abundances of dolomite correlate with higher enrichment of $\delta^{18}O$. (C) Plot of $\delta^{13}C$ and dolomite abundance. Higher abundances of dolomite correlate with higher enrichment of $\delta^{13}C$.

3.4.6. Major and trace element geochemistry

Dolomitized CRA have the widest range of Mg/Ca (ppm/ppm) ratios, with a minimum of 0.21 and a maximum of 0.58, with an average of 0.42 and standard deviation (SD) of 0.079. Dolomite cements have a smaller Mg/Ca range of 0.39 to 0.52, with an average of 0.45 and SD of 0.028. Dolomitized matrix has the smallest range of Mg/Ca ratios, with a minimum of 0.32 and a maximum of 0.45, with an average of 0.42 and SD of 0.029. Calcitic components have generally very low Mg/Ca ratios of 0.01 to 0.07, with an overall mean value of 0.02 and SD of 0.015 (**Fig. 3-10, Supplementary Table 2**).

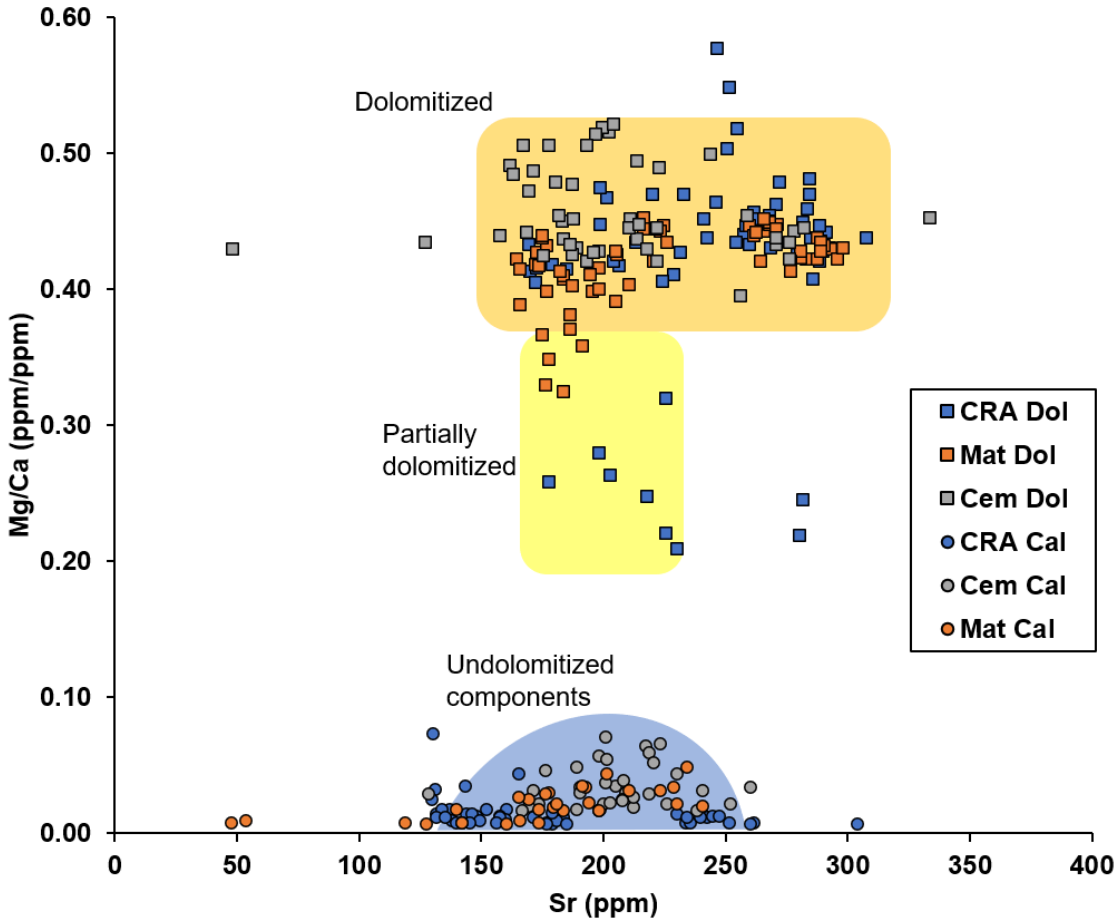

Figure 3-10: LA-ICP-MS geochemistry crossplot of Mg/Ca ratios and Sr concentration on specific components. Dolomitized (not stained) components as squares, undolomitized (stained) components as circles. CRA Dol = Dolomitized coralline red algae, Mat Dol = Dolomitized matrix, Cem Dol = Dolomitized cement. CRA Cal = undolomitized coralline red algae, Mat Cal = undolomitized matrix, Cem Cal = undolomitized cement, L&M Cem = Lucia and Major (1994) Mg/Ca and Sr crossplot results for dolomite cements in Goto Meer, L&M Rep = Lucia and Major (1994) Mg/Ca and Sr crossplot results for replacement dolomite in Goto Meer.

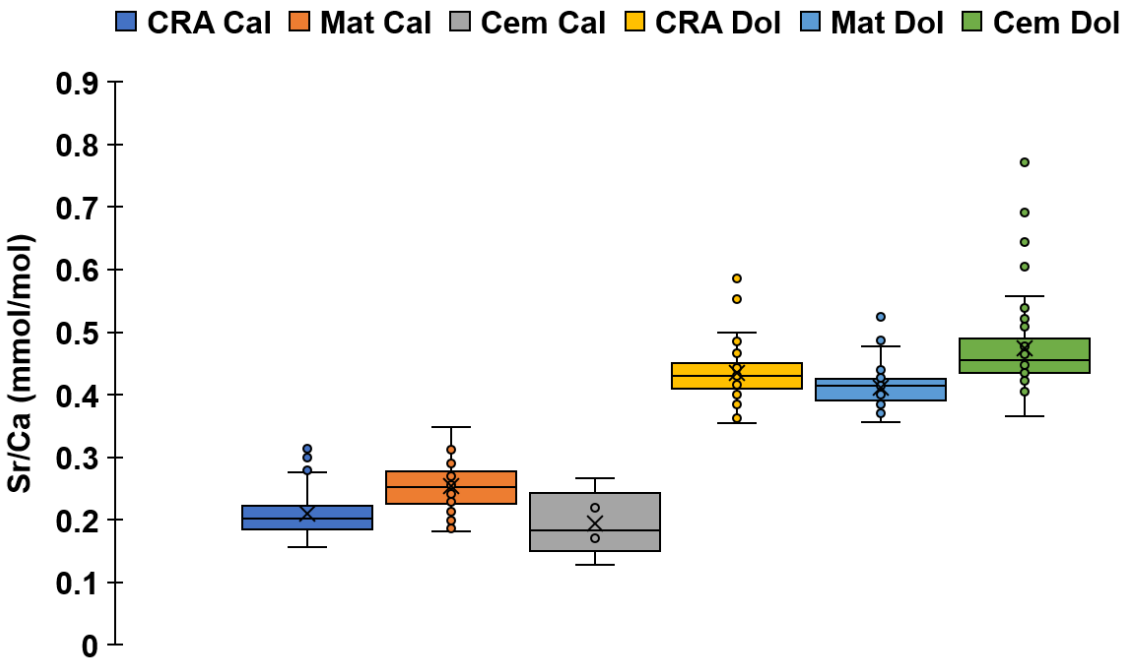

Figure 3-11: LA-ICP-MS geochemistry distributions of Sr/Ca values on dolomitized and undolomitized components. CRA Dol = Dolomitized coralline red algae, Mat Dol = Dolomitized matrix, Cem Dol = Dolomitized cement. CRA Cal = undolomitized coralline red algae, Mat Cal = undolomitized matrix, Cem Cal = undolomitized cement.

Strontium (Sr) concentrations in dolomitized components range between 48 ppm to 333 ppm, with dolomitized coralline red algae containing the highest average Sr concentration among all components (242 ppm, SD of 38.3), followed by the dolomitized matrix (226 ppm, SD of 45.4), with the dolomitized component having the lowest average Sr concentrations (205 ppm, SD of 46.2). Undolomitized components have similar Sr concentration ranges of between 47 ppm and 336 ppm. Both undolomitized cement and micritic matrix contain the highest average Sr concentration among all components (200 ppm, SD of 32.2 and 61.1 for cement and matrix

respectively), with the CRA component having the lowest average Sr concentrations (181 ppm, SD of 46.4) (**Fig. 3-10**).

In calcitic samples, the matrix show the highest Sr/Ca (mmol/mol) ratios with an average of 0.25, followed by CRA with an average of 0.21, and lastly the cement component at 0.19. Dolomitized samples show generally larger Sr/Ca ratios than undolomitized samples, with dolomitized CRA, cement, and matrix showing averages of 0.43, 0.47, and 0.41 respectively (SD of 0.039, 0.066, and 0.029 respectively) (**Fig.** 3-**11**).

3.5. Discussion

3.5.1. Are HMC bioclasts preferentially dolomitized?

Selectivity values in Seru Grandi outcrop favor matrix following red algae bioclast over all other components. To explain those observation, we suggest two main controls including 1) mineralogy or 2) reactive surface area. Mineralogy is likely to be a driven factor due to stability and reactivity of the component as we discussed in the introduction. The matrix in the study strata is deposited as aragonite, based on the relative higher Sr values within the micrite matrix which implies aragonite precursor (Tucker and Wright 1990). However, if we assumed that bioclasts with higher Mg concentration would result in preferential dolomitization. We would expect CRA to be the most consistently selectively dolomitized among all carbonate components, (Chave 1954). But, in fact this is not the case in those deposits, in contrast, micrite consistently is more selectively dolomitized, followed by CRA, which imply that aragonite precursor

could have influenced this process. However, our stable isotope observations point towards stabilization of all components to LMC prior to reflux dolomitization (**Fig. 9**) Correspondingly, at the same conditions (temperature and fluid chemistry) reactive surface area would have significant control in selective dolomitization. In general, micrite would present high reactive surface area relative to other components since its consistently small size (<63 μm) and thus larger surface area to volume ratio (Constantz 1986). As dolomitization proceeds via a dissolution-precipitation reaction (Machel 2004), and that the dissolution of calcite/aragonite exponentially increases with decreasing grain size, with particles measuring <1 μm in diameter having activity values up to 8 times more than particles with 1000 μm (Chave and Schmalz 1966). On the other hand, CRA are composed of cryptocrystalline crystallites (~10 nm)(Auer and Piller 2020) which greatly increases the reactive surface area as well, making CRA likely to be also high reactive. However, matrix displays microporosity that allows higher rock-fluid interactions, in contrast to a tight packing of nanocrystalline structure of the red algae preventing and reducing the interaction with the pore fluids. Other allochems do show large crystals in their structures (Constantz 1986; Smith 1990), and therefore would have significantly smaller reactive surface areas. In summary, aragonitic matrix with high reactive area is the prefer component to dolomitized first, following by HMC red algae skeleton.

This relationship of higher surface areas resulting in more dolomitization is consistent with previous studies such as Murray and Lucia (1967), whom observed that the dolomite distribution within the Mississippian Turner Valley Formation in Alberta,

Canada, is controlled by the distribution of micrite; wherein higher occurrences of micrite correlated with higher abundances of dolomite; and reactive transport model tests by Al-Helal et al. (2012) and Whitaker and Xiao (2010). Bullen and Sibley (1984) similarly suggested that selective dolomitization is more likely driven by reactant crystal size than mineralogy based on their laboratory dolomite synthesis experiments.

3.5.2. Differences in diagenesis within clinoforms

Dolomite replacements and cements vary within clinoform strata, which reflect the evolution of the dolomitizing fluids. Within updip strata dolomite crystals are larger (100-400 μm) and more euhedral (**Fig. 3-5**), which aligns to the proposed mesohaline reflux dolomitization model by Laya et al. (2021) and the theoretical model proposed by Adams and Rhodes (1960); Saller and Henderson (1998). In the reflux model, dolomitizing fluids will be sourced from modified seawater, and will flow downwards and outwards towards the coast according to a hydrodynamic created by density gradient (Budd 1997b; Saller and Henderson 1998; Whitaker et al. 2004; Jones and Xiao 2005). As this fluid interacts with the carbonate sediments, the Mg within these fluids will gradually be consumed, leading to progressively lower dolomite supersaturation state as the fluid evolves with distance from the source(Saller and Henderson 1998; Jones and Xiao 2005; Al-Helal et al. 2012). As dolomite crystal habits are a function of the supersaturation of dolomite and availability of Mg, (Sibley et al. 1993).

Dolomite crystals forming proximal to the dolomitizing fluid source should be larger and more euhedral than dolomite crystals forming distal to the dolomitizing fluid as we observe in the clinoforms.

Additionally, several samples do not show replacement dolomite but contain abundant dolomite cements instead **(Fig. 3-8 C).** The replacement process usually requires an undersaturation of calcite/aragonite for dissolution to occur, which subsequently increases the saturation state of dolomite which allows for it to precipitate in the precursor's place (Morse and Mackenzie 1990). However, in the case of only dolomite cements, dolomitizing fluid conditions may be supersaturated with respect to dolomite but not undersaturated with respect to calcite and aragonite, thereby precluding the dissolution reaction from occurring (Morse and Mackenzie 1990).

Calcite cements variations may also reflect changes in fluid geochemistry post-dolomitization. We observe the occurrence of meteoric stalagtitic and isopachous calcite cements within the downdip strata growing over dolomite cements; no calcite cements are observed to overgrow dolomite cements in updip sections (**Fig. 3-5 C, D**). After the last major sea-level fall, deposition and dolomitization of the Seru Grandi clinoforms ceased at approximately 4 mya (Laya et al. 2018a). While high frequency, high amplitude sea level variations after the Miocene may allow for late marine calcite cements (and are very rarely observed) to form within downdip pores whilst leaving updip pores unaffected, only one major flooding event during the Pleistocene MI5e is recorded to affect Bonaire after the deposition of the Seru Grandi clinoforms (Engel et al. 2013; Felis et al. 2015; Laya et al. 2018b; Rixhon et al. 2018). Additionally, our

stable isotope (**Fig. 3-12**), trace element observations (**Fig. 3-11**), and petrographic observations (**Fig.** 3-5**)** strongly support a late meteoric diagenesis overprinting. Thus, the absence of calcite cements growing on dolomite cements in updip strata may instead be a result of variations in the water table as a result of the aforementioned sea level variations, which thus causes variations in part of the sediments undergo vadose or phreatic diagenesis (Tucker and Wright 1990). Sediments above the water table (usually updip) in the vadose zone are more likely to be undersaturated with respect to calcite, whereas sediments below the water table (usually downdip) in the phreatic zone are more likely to be saturated with respect to calcite. This is evidenced by the often isopachous nature of meteoric cements in downdip cements (**Fig. 3-5 D**)

3.5.3. High-Mg calcite as a source of Mg for dolomitization

Local source dolomitization as a result of Mg sourced from coralline red algae is inferred based on petrographic observations of dolomite occurring within coralline red algae (CRA) grains rather than on the periphery of the grains (**Fig. 3-4**) and also crystals appearing to emanate from CRA grains (**Fig. 3-4 E**). These observations suggest that the occurrence of dolomite nucleation is within the core of these skeletal grains implying an internal sourcing of Mg which can enrich the fluids causing supersaturation with respect to dolomite. Upon stabilization to LMC, HMC such as CRA can liberate appreciable amounts of Mg into the surrounding pore waters, as demonstrated by stabilization experiments by Land (1967). These porewaters would have a locally higher Mg/Ca ratio of fluids, which would thus increase the supersaturation of dolomite (Morse and

Mackenzie 1990; Kaczmarek and Sibley 2011) immediately surrounding the CRA and within CRA grains, causing precipitation of dolomite immediately surrounding and within CRA grains as observed in our samples.

We would expect most of the intragranular surfaces (surfaces within intragranular pores) within CRA to be initially unaffected by external fluids due to their isolation and/or highly constricted pore throats (<1 μm) within CRA microstructures. As dolomitization at surface conditions typically require substantial time scales in the order of 10k to 100k years (Machel 2004), the porewaters immediately surrounding the CRA must remain stagnant for similar timescales. These stagnant porewater conditions could be the case since, the generally red algae structure is a tight crystalline packing and show low porosity and permeability. This is also the case in values of permeability of the Seru Grandi strata presented by Laya et al. (2021). Similar conditions have also been observed by Land and Epstein (1970) in the Late Pleistocene limestone successions of Jamaica, wherein coralline red algae are observed to be selectively dolomitized.

3.5.4. Geochemical interpretations for timing and origin of diagenetic events

Stabilization of coralline red algae (CRA) to low-magnesium calcite (LMC) likely occurred prior to dolomitization. In the case of coralline red algae (CRA), vital effects during biomineralization of their HMC cells typically result in their skeletons having depleted $\delta^{18}O$ values between -4 to -2‰ (Wefer and Berger 1991). Additionally, dolomitization would result in an enrichment of approximately 3.0‰ at 25 C (Land

1992). Thus, we would expect to observe generally more depleted values dolomite $\delta^{18}O$ values in CRA relative to the bulk sediment if they were to be dolomitized prior to any isotopic re-equilibration from diagenesis (**Fig. 3-12**). However, that is not the case; CRA clasts do not show any meaningful difference in stable isotope values relative to the bulk rock for both limestone and dolomite samples (**Fig. 3-9**). This suggests that prior to dolomitization, CRA clasts have likely undergone sufficient diagenesis to convert their HMC skeletons into LMC, which would re-equilibrate their stable isotope composition to be closer to the marine fluids at the time which are enriched in $\delta^{18}O$ (-2 ‰ to 0 ‰ VPDB for Upper Miocene sea-surface $\delta^{18}O$ values (Grossman 2012) relative to the HMC CRA skeleton. (Laya et al. 2021)

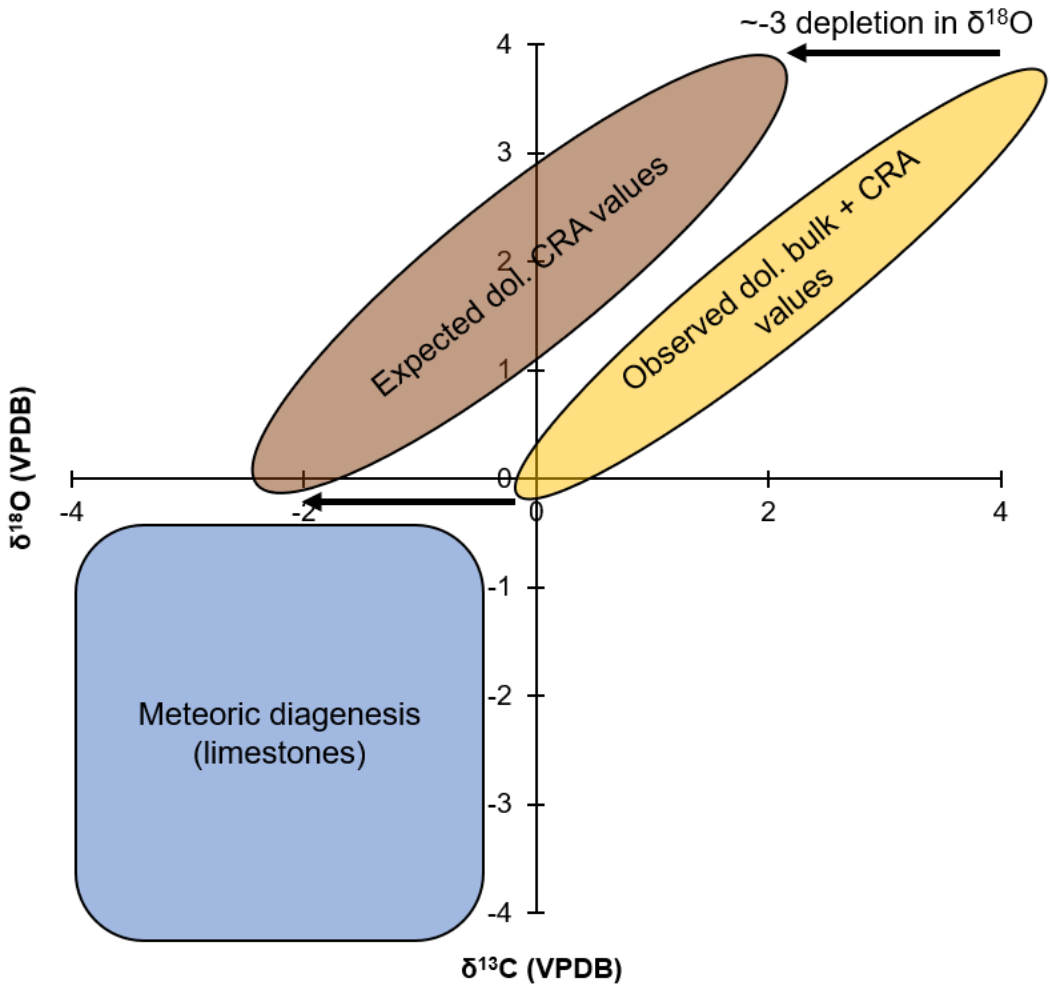

Figure 3-12: Range of observed bulk and coralline red algae (CRA) $\delta^{13}C$ and $\delta^{18}O$ stable isotope values and expected range of dolomitized CRA values if no stabilization of CRA from HMC to LMC has occurred prior to dolomitization and field of values for limestones affected by meteoric diagenesis.

Trace element and stable isotope geochemistry data also suggest that meteoric diagenesis has overprinted the Seru Grandi clinoforms (**Fig. 3-11, Fig. 3-12)**. This is based on the relatively depleted $\delta^{18}O$ values (<0 ‰ VPDB), and low Sr/Ca ratios of calcites (<50% dolomite) samples. Relative to fluids of marine origin, meteoric fluids are depleted in ^{18}O and Sr. Thus, meteoric diagenesis often imparts depleted $\delta^{18}O$ values

and low Sr/Ca ratios, whereas marine diagenesis will have $\delta^{18}O$ which are close to 0 (James and Jones 2015).

The range of Mg/Ca and Sr/Ca values of dolomitized and undolomitized components can also be indicative of the precursor mineralogy and amount of dolomitization. For example, the dolomitized matrix shows the smallest values (range and averages) Mg/Ca values (average of 0.42 (ppm/ppm)). Additionally, undolomitized micritic matrix also has the highest Sr/Ca ratio among all undolomitized components, suggesting that, the micrite matrix initially was deposited as aragonite, which is known that contains 10 times more Sr within its crystal lattice relative to calcite preserved its higher Sr concentration after stabilization (Baker 1986; Baker and Bloomer 1988; Swart and Guzikowski 1988; Swart and Burns 1990; Banner 1995; Kramer et al. 2000; Melim et al. 2002). The consistently low Mg/Ca values of undolomitized CRA also indicate that there is no preservation of the original HMC of the CRA skeletons in the present day, which has been known to occur under exceptional diagenetic conditions such as those in the Late Pleistocene limestone successions of Jamaica (Land and Epstein 1970). Dolomite cement is also observed to have generally higher Mg/Ca ratios relative to other components (**Fig. 3-13)**. This is consistent with the model of reflux dolomitization, wherein more intensely dolomitized sediments will begin to undergo dolomite cementation and therefore be more stoichiometric. This finding is similar to that of Lucia and Major (1994) in separate outcrop on Bonaire, wherein they also demonstrate that Mg/Ca ratios are elevated in dolomite cements relative to replacement dolomite.

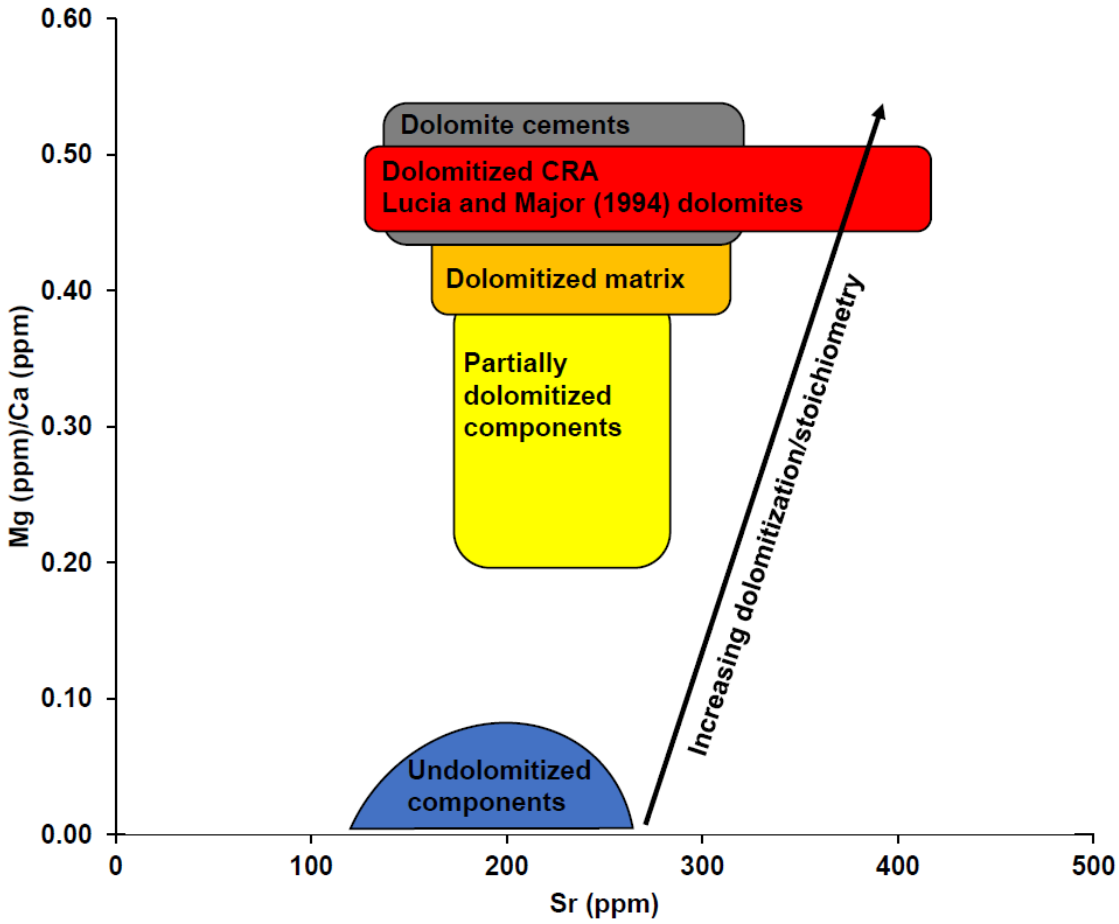

Figure 3-13: Mg/Ca (ppm/ppm) and Sr (ppm) fields showing generalized fields for undolomitized, partially dolomitized, and dolomitized components. Increasing dolomitization is reflected in elemental data as an increase in Mg/Ca ratio, and to a lesser extent, and increase in Sr concentrations.

The Sr/Ca ratios of the different dolomitized components also show distinctly different distribution ranges (**Fig. 3-11**). This can indicate the relative timing of dolomitization for the different components, as the Sr concentration in dolomite is a function of the Sr/Ca ratio of the dolomitizing fluid and distribution coefficient

(Vahrenkamp and Swart 1990; Lu and Meyers 1998). Thus, the differences in distributions indicate that the components did not dolomitize homogeneously nor all at once, which further supports the idea of preferential dolomitization.

3.5.5. Paragenetic sequence of Seru Grandi clinoforms

Based on our observations and building upon previous research (Laya et al. 2018a; Laya et al. 2021), we propose two different paragenetic sequences within the Seru Grandi clinoforms; one for updip clinoform sediments and another for downdip clinoform sediments (**Fig. 3-2, Fig. 3-14**). In both settings, as initially proposed by Laya et al., (2021), the diagenetic history begins in a shallow marine setting, with local thin bladed rims of cement and minor micritization of grains.

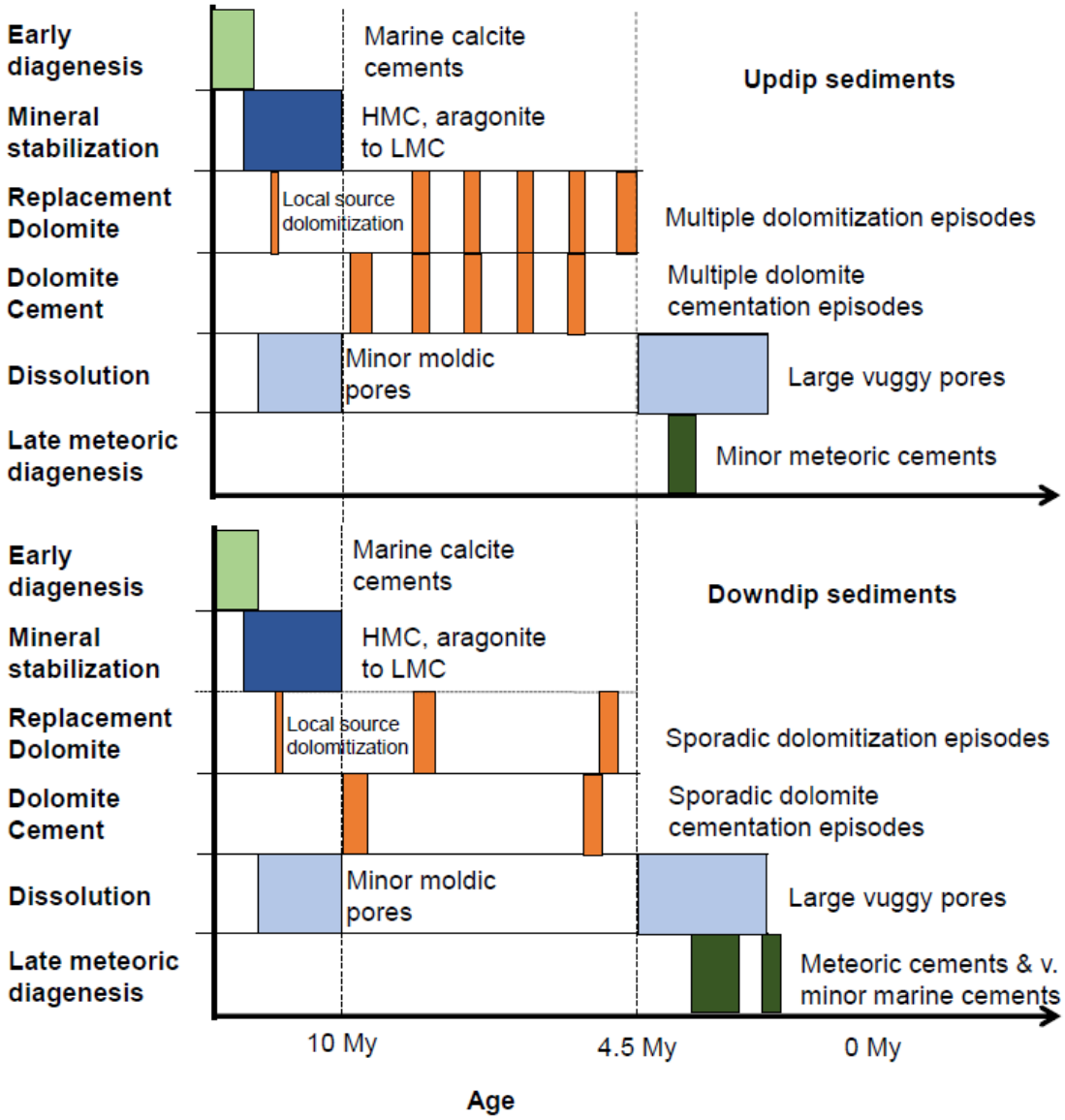

Figure 3-14: Paragenesis of Seru Grandi clinoforms showing relative timing for diagenetic events within updip and downdip sections. Absolute ages of events derived from Laya et al. (2018) and Laya et al. (2021).

Our stable isotope observations (**Fig. 3-9, 3-12**) suggest that mineral stabilization of HMC and aragonite to LMC occurs shortly after and in parallel with early marine diagenesis and prior to any major dolomitization. Brief periods of exposure during this

period lead to meteoric diagenesis dominating, leading to the formation of minor moldic pores via dissolution of certain bioclasts.

Updip sediments were affected by more dolomitization episodes as they are located more proximal to the source of dolomitization fluids, which in this case, is mesohaline reflux (Laya et al. 2021). At least 5 separate dolomitization events are recorded in updip sediments, based on CL observations (**Fig. 3-6**). Downdip sediments had dolomitization episodes as those rocks are in distal location from the source of dolomitizing fluids which resulted in fluids depleted in Mg and thus lower dolomite saturation of the dolomitizing fluids (Laya et al. 2021).

After a significant drop in relative sea-levels after 4.5 My paired with gradual tectonic uplifting (Hippolyte and Mann 2011), the succession was exposed to meteoric diagenetic processes as evidenced by the depleted (<-1 ‰ VPDB) oxygen isotope values which are still in effect to present day, forming abundant large vuggy pores. Meteoric cements filled pores and fractures, with overgrowths occurring on preexisting dolomite cements within downdip sections (**Fig. 3-5**).

3.6. Conclusions

Selective dolomitization is observed within partially dolomitized samples of the Seru Grandi, Bonaire. However, HMC allochems are not consistently selectively dolomitized as initially thought. The micrite matrix is most likely to be dolomitized first, followed by coralline red algae, and subsequently all other allochems (echinoderms, bivalves, coral fragments) are likely to be among the last to be dolomitized. However,

when extending this observation to sediments involving only grainstones and very mud-poor packstones, coralline red algae would indeed be more likely to be dolomitized relative to other allochems. We also show dolomite distribution at grain scale that suggests sufficient internal sourcing of Mg from coralline red algae could be responsible initiate and sustain small-scale local dolomitization, which supports a link between Neogene global dolomitization events and the rise in CRA species abundance within the same period. Trace and major element data also demonstrate that the micritic matrix is initially deposited as aragonite, and that there is no preservation of HMC in the CRA skeletons. Additionally, we describe a more complex paragenetic sequence for the Seru Grandi clinoforms than previously known, with distinct differences in diagenetic effects between updip and downdip strata due to the evolution of diagenetic fluids as they permeate through the clinoform strata and the position of the water table controlled by sea-level during the Neogene and Holocene. Collectively, our observations show that selective dolomitization in ancient rocks does not strongly depend on magnesium concentration of the components, but more so the available surface area of the carbonate component, and that detailed analyses of individual carbonate components can provide a more complete picture of the diagenetic history in carbonate successions.

4. THE EFFECTS OF DOLOMITE GEOBODIES WITHIN CARBONATE CLINOFORMS ON FLUID FLOW AND CONNECTIVITY: INSIGHTS FROM AN OUTCROP ANALOGUE ON BONAIRE, THE NETHERLANDS

4.1. Synopsis

Carbonate clinoforms are often challenging to characterize and model due to their complex geometries and additional heterogeneity introduced by diagenetic processes. Dolomitization can influence petrophysical properties resulting in either an increase or reduction in porosity and permeability of the host rock and forms geobodies of varied shapes depending on pre-dolomitization permeability patterns and dolomitization mechanism. Therefore, in partially or fully dolomitized successions, the prediction of fluid flow behavior is not trivial. This study uses a well-studied outcrop analogue of Mio-Pliocene partially dolomitized clinoforms at Seru Grandi (Bonaire) to better understand fluid flow in different dolomitization scenarios. Clinothems consist of heterogeneous coralline algal facies overlying bioclastic facies, with dolomite geobodies truncated on their upper and lower bounds by clinoform surfaces. Digital outcrop models were used to characterize geometry and spatial relationship of facies and heterogeneity, such as clinoform dip, length, height, and spacing. Multiple realizations of clinoform and dolomite body geometries are modelled using a surface-based modelling (SBM) approach coupled with an unstructured mesh flow simulator (IC-FERST). Two scenarios are considered, in which dolomitization has resulted in either a decrease in porosity and permeability as observed in outcrop, or a relative increase of porosity and permeability

values as a potential subsurface scenario. Flow simulation results reveal an exponential relationship between water breakthrough times and flow rates versus dolomite proportions. Additionally, the arrangement of the dolomite bodies (aligned vs. disjoined) exhibits very similar fluid flow behavior across a wide range of dolomite proportions. Sensitivity of flow behavior to the geological models is strongly dependent on dolomite permeability relative to precursor limestone. Dolomite body arrangement is more important for flow behavior at high dolomite proportions for low permeability dolomite, or at low dolomite proportions for high permeability dolomite. This study emphasizes the significance of having a good understanding of the dolomitization mechanism and dolomite body geometries, reducing uncertainty in dolomite distribution, petrophysical properties, and, therefore, fluid flow behavior.

4.2. Introduction

Clinoforms in carbonate subsurface reservoirs are widespread (Pierson et al. 2010) and are frequently affected by partial or complete dolomitization (George and Stiles 1978; Sun 1994). However, the impact dolomitization has on effective flow behavior of such clinoform intervals is not well understood. Using the an outcrop analogue (Seru Grandi) of carbonate clinoform deposits in Bonaire, The Netherlands, as an example (Laya et al. 2021), flow behavior in multiple dolomitization scenarios are tested using geological modelling and simulation, considering dolomite proportion and dolomite bodies as baffles versus conduits. Grid-free modelling approach with fully

unstructured tetrahedral simulation meshes (Jacquemyn et al, 2019) is used to overcome key adverse grid-effects associated with modelling and simulating dipping geometries (clinoforms), pinchouts (facies boundaries) and dolomite bodies (complex geometries) on cornerpoint grids.

Clinoforms are defined as sigmodal strata with m to km scales typically deposited in subaqueous environments, which are formed by the progradation of sediments as a result of the complex interplay between tectonics, eustasy, sediment supply and preexisting topography (Henriksen et al. 2011; Laya et al. 2018b; Patruno and Helland-Hansen 2018). The sediment/rocks bounded by clinoforms are referred to as clinothems (Rich 1951; Steel et al. 2002). Commonly, clinoforms show an asymmetrical sigmoidal shape, which are bounded by bedding planes (Rich 1951). Thickness between bounding surfaces varies greatly depending on the scale of the deposits (Thorne 1995; Pomar et al. 2004; Thomas et al. 2021). For example, Thomas et al. (2021) document 15 – 20 m thick clinoforms in the Paris Basin within the Jurassic Oolite Blanche Formation, which have been interpreted as giant migrating dunes within a shoreface depositional environment. Similarly, Pomar et al. (2004) observe 10-15 m thick dolomitized clinoforms dipping at 12–20° with alternating bedsets of red algal rudstones and bioclastic grainstones within the Miocene Lower Bar Unit of Menorca. Large scale (1000's to 100's m) examples include the Great Bahamas Bank (GBB) (Anselmetti et al. 2000) and the Kardiva Platform in the Maldives (Betzler et al. 2013). At the km scale, carbonate clinoforms have historically been highly-productive reservoirs such as those in the Wasson and Means fields in the Permian Basin, Texas (Schneider 1943; George and

Stiles 1978), or the Jurassic Smackover Formation in north Louisiana (Handford and Baria 2007). At present, both relatively underdeveloped basins such as the Northern Carnarvon basin in Northwest Australia (Tesch et al. 2018) and the currently producing Late Aptian Upper Shu'aiba Formation (Pierson et al. 2010) have sizeable carbonate clinoforms, which may host significant petroleum reserves. However, their geometry also provides additional challenges to predicting the behavior of fluid flow and overall recovery within such deposits (Strohmenger et al. 2006; Adams et al. 2011).

Dolomite geobodies can form minor to extensive baffles (Lucia and Major, 1994) or conduits (Weyl, 1960) to fluid flow. The origin of these dolomite geobodies can give an indication as to whether they will act as baffles or conduits; while each dolomitization model (for example, hydrothermal, reflux, burial, and geothermal) can produce dolomites which can be either destructive or constructive for porosity and permeability (Machel 2004; Whitaker et al. 2004), the distribution and extent of porosity and permeability changes can vary from model to model. Therefore, the net effect of dolomite being more permeable or less permeable than the precursor limestone will also vary depending on dolomitization model. When these dolomite geobodies are superimposed onto a clinoform system, these geobodies can form complex geometries, which will ultimately impact the productivity of a reservoir. Prominent examples of this process are the dolomitized reservoirs in the Middle East, such as the Jurassic Arab-D Member of the Ghawar field in Saudi Arabia, which shows dolomitic facies (70 – 100% dolomite) with permeability values 1 to 2 orders of magnitude higher than a comparable mudstone/wackestone facies of the same porosity (Cantrell et al. 2004; Yakhiyayev et al.

2016) (Davis et al. 1997). Additionally, Arab-D dolomite reservoirs show high permeability zones cross-cutting stratigraphic boundaries, while in other instances, dolomites act as permeability barriers (Cantrell et al., 2004). Dolomitization also can "homogenize" the precursor limestone as in Karachaganak field, Kazakhstan and in the Permo-Triassic Khuff Formation in Qatar, by reducing the range of porosity and permeability values in dolomitized intervals (Bashari 2005; Yakhiyayev et al. 2016). In summary, dolomite bodies can focalize flow into conduits or act as flow baffles, modifying the flow routes within any given reservoir therefore leading to early water breakthrough and bypassed oil. Therefore, understanding processes related to dolomitization will provide a significant tool to predict reservoir performance.

Flow simulations can facilitate in the understanding and prediction of fluid flow behavior in reservoirs. However, conventional cornerpoint grid-based simulators are not well-suited to accurately compute flow behavior of dolomitized clinoforms. Dipping surfaces would result either in stair-stepped geometries and thus require a very high-resolution grid for accurate representation, or in very skewed clinoform-parallel grid cells and thus reduced simulation quality or even non-physical simulation results. These grid effects are widely recognized in similar studies of flow behavior in clinoforms, both in carbonates and siliciclastics (Jackson et al. 2009; Adams et al. 2011). Truncation of facies boundaries and clinoforms causes a high number of pinchouts to be present, also negatively impacting simulation quality. By changing the number and location of dolomite bodies, it is also not known a priori where baffles or zones of good connectivity will be. Designing an appropriate grid that would preserve bodies and honor

clinoform dips and pinchouts for each model realization is not trivial. Therefore, we are using a surface-based geological modelling approach (Jackson et al. 2014) that represents the geometries accurately by using grid-free surfaces (Jacquemyn et al. 2019). As the geology is modelled free from any grid, small features, such as baffles, pathways between dolomite bodies, dipping surfaces, and pinch-outs between facies boundaries and clinothems are preserved. Flow simulation using unstructured tetrahedral meshes ensures geological representation is honored while maintaining high simulation quality by dynamically adapting the mesh to flow behavior throughout the simulation (Jackson et al. 2015; Salinas et al. 2017a; Salinas et al. 2017b).

The aim of this study is to assess the impact *of dolomite geobodies and their abundance on flow behavior in carbonate clinoforms.* To answer this question, we have the following research objectives: 1) Quantitatively describe clinoform geometries and spatial arrangement of dolomite geobodies in the Seru Grandi outcrop; 2) Integrate rock property data and interpretations (dolomitization model, facies distributions, porosity and permeability) from this study (scenario 1, dolomite forms baffles) and previous studies (scenario 2, dolomite forms conduits); 3) Use the descriptions and data to build geological models and fluid flow characterization using surface-based modelling flow simulation for a range of dolomite abundances

To achieve these objectives, we will explore clinoform dimensions and rock properties of the Seru Grandi outcrop in Bonaire, The Netherlands, as our key analogue to understand the effect of dolomite bodies within clinoforms and how it impacts flow

behavior. The outcrop has excellent exposures of very well preserved partially dolomitized meter-scale carbonate clinoforms displaying multiple dolomitization fronts and has been extensively characterized (Laya et al. 2018a; Laya et al. 2021).

4.2.1. Geological background of the outcrop analogue

The island of Bonaire is located in the southern Caribbean Sea, 90 km north of the Venezuelan coast. The geology of Bonaire comprises four primary stratigraphic units: 1) Cretaceous volcanic basement (Washikemba Formation) formed of deformed volcanic rocks; 2) Eocene sandstones and siltstones (Soebi Blanco Formation); 3) Miocene-Pliocene carbonates (Seroe Domi Formation), and 4) Pleistocene shallow-marine reefal carbonates, (no formal lithostratigraphic name), and 5) Reefal and evaporitic deposits within Holocene-Recent hypersaline lakes (no formal lithostratigraphic name), (**Fig. 4-1**) (Alexander 1961; Deffeyes et al. 1965b; Bandoian and Murray 1974; Zapata et al. 2014; Laya et al. 2018b; Laya et al. 2021).

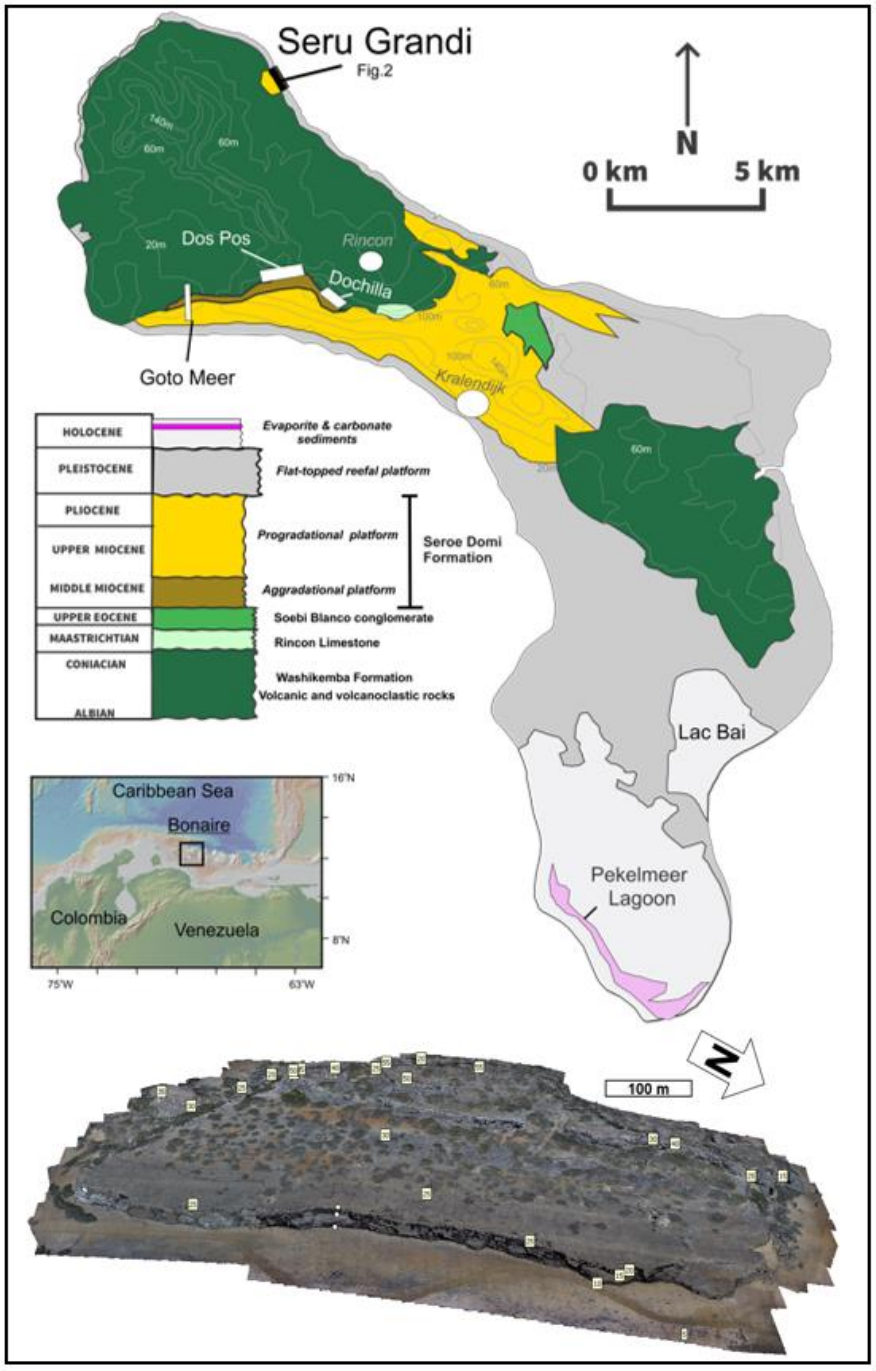

Figure 4-1: Simplified geological map of Bonaire, with location of Bonaire within the Caribbean Sea, location of the Seru Grandi outcrop highlighted, associated Seroe Domi Formation outcrops, direction of progradation for Seru Grandi clinoforms, and overall stratigraphy (Above). Digital outcrop model (DOM) of Seru Grandi outcrop with associated elevation markers (Below). Modified from Laya et al. (2021).

The Seroe Domi Formation has been subdivided into two informal units, an older member (aggradational platform) and the younger member (progradational platform), which are separated by an angular unconformity (Laya et al. 2018b; Laya et al. 2021). This study focuses on a Mio-Pliocene (progradational platform) outcrop of the Seroe Domi Formation. The outcrop analogue is named "Seru Grandi" and is formed of a succession of shallow-water carbonate deposits, overlying a complex volcanic basement (Laya et al. 2018a) (**Fig. 4-1, 4-2)**. The study outcrop presents a dip-parallel cross section through a series of clinoform in a ~800m long exposure parallel to the north area of the eastern coast (Laya et al. 2021).

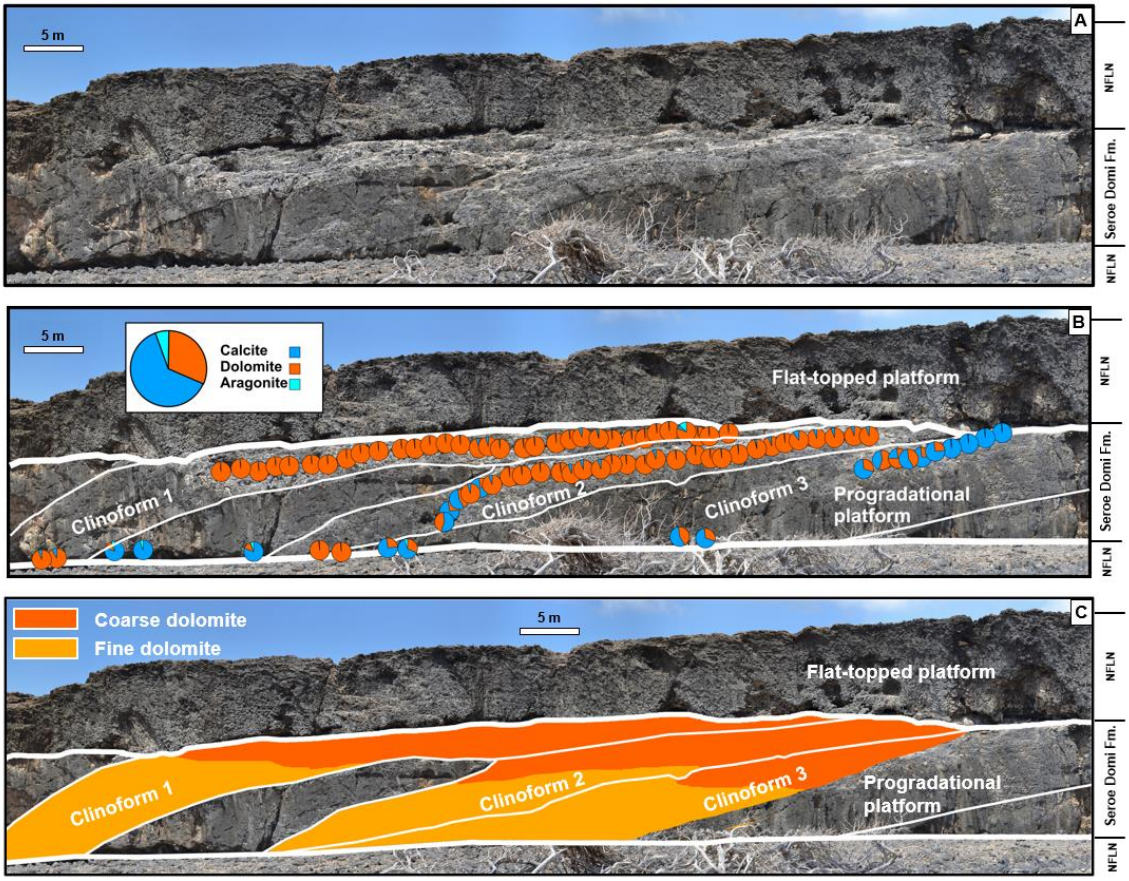

Figure 4-2: Photomosaics of Seru Grandi outcrop. NFLN = No formal lithostratigraphic name. A) Uninterpreted photomosaic of outcrop face. B) Distribution of mineralogies along sampled clinoforms. Modified from Laya et al. (2021) C) Distribution of dolomite textures.

The Seru Grandi clinoforms are interpreted as subaqueous shelf edge clinoforms in the classification proposed by Patruno and Helland-Hansen (2018) and adapted for carbonate depositional successions. The progradational clinoforms are composed primarily of calcareous coralline red algae with minor coral fragments, large benthic foraminifera, echinoids, rare bivalves, and volcanic lithic clasts. Individual clinothems

exhibit lateral changes in facies, with the updip section consisting predominantly of encrusting red algae and rhodolith-rich facies, grading downslope over 15-20 m into a bioclastic facies (**Fig. 4-2, 4-3**). The overlying Pleistocene section consists of structure-less reefal facies formed of calcitic coral rudstone with red algal encrustations. The contact between the two units is an erosional unconformity which shows an irregular karstified surface representing a depositional hiatus of ~1 My (**Fig. 4-2, 4-3**) (Laya et al. 2018a).

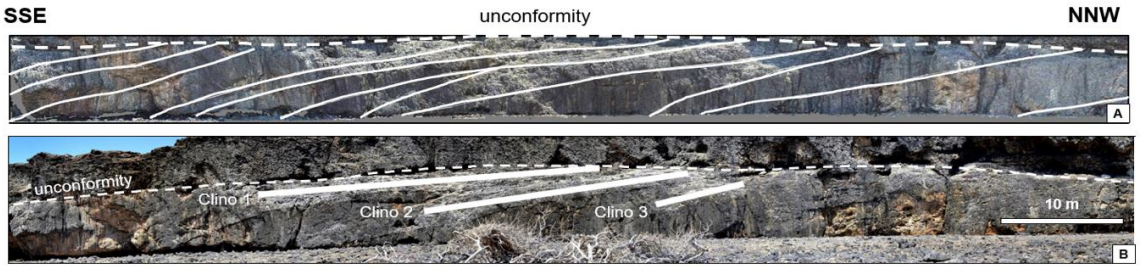

Figure 4-3: Photomosaic of outcrop face. A) Panorama of the Seru Grandi clinoforms, with interpreted clinothem surfaces. B) Inset showing set of clinothems where in-depth field sampling was conducted, and lateral transects sampled.

The clinoform strata of Seru Grandi show a relatively short diagenetic history. Initially, a brief marine diagenesis stage that is characterized by thin bladed rims and micritized grains. Subsequentially, multiple stages of mesohaline dolomitization occurred which intermittently dolomitized the clinoforms penecontemperaneously, leading to the sharp clinoform surface-bound characteristic of the dolomite geobodies

(Laya et al. 2021). Final subaerial exposure, late meteoric diagenesis, and mineral stabilization can be attributed to the most recent sea-level fall (Sulaica 2015; Laya et al. 2021). Dolomitization of the Seroe Domi Formation is pervasive and displays sharp reaction fronts which tend to conform to individual clinoform surfaces (Laya et al. 2018a; Laya et al. 2021). These Miocene-Pliocene dolomites were formed mainly as early replacement dolomite, with variable dolomite abundances in different units (Bandoian and Murray 1974; Sibley 1980; Sibley 1982; Lucia and Major 1994b; Laya et al. 2018b).

Sedimentation in the progradational platform occurred mostly in the oligophotic zone and slightly deeper water close to the platform margin (Laya et al. 2018b). Dolomite texture in Seru Grandi outcrop presents four different types, from fine crystalline (<15 μm) to coarse crystalline cements (>100 μm) (Laya et al. 2021). Different dolomite types are associated with various dolomitization stages when slightly denser fluids (mesohaline) sunk into the individual clinoforms. Distribution of the dolomite type shows that fine crystalline replacement dolomite dominated the updip areas of the clinoform in contrast, coarser dolomite cements which are common downdip (Laya et al. 2021).

Laya et al. (2018a) reported four facies on the progradational platform to describe both limestone and dolomite units; however, for this study, only three lithofacies are adopted from the Seru Grandi outcrop, 1) Coralgal grainstone/packstone and reworked red algal-rich grainstone/packstones are merged and referred to as bioclastic limestone in this study; 2) Encrusting red algal-rich grainstone/packstone are

referred to as encrusting/rhodolitic or encrusting algae limestone in this study, and 3) all dolomitized facies are merged to be referred to as the dolomite facies in this study

4.3. Methods and datasets

To achieve our research objectives, we apply the following workflow. Firstly, partially dolomitized carbonate clinoform geometries were quantified based on outcrop observations and DOMs and their associated petrophysical properties measured. Surface based geological model realizations are then produced based on the outcrop measurements. Dolomite distribution and quantification were based on the outcrop observations, sampling, and statistical analyses. Uncertainty in the amount of dolomitization in the entire outcrop is addressed by generating multiple realizations of varying dolomite abundances within these geological models. Two scenarios are tested within the geological framework. In the first scenario, the dolomite geobodies are less permeable (corresponding to outcrop samples), and in the second alternative scenario, the dolomite geobodies are more permeable than their equivalent limestone. Flow simulations tested these two scenarios to determine fluid flow behavior as a function of dolomite geobody abundance. Details on methods and procedures step by step are explained in the following subsections.

4.3.1. Outcrop characterization and sampling

Fieldwork results and other data from the Seru Grandi outcrop (e.g., petrographic observations, geochemistry, facies scheme and porosity and permeability values) are initially reported in Laya et al. (2021) and Laya et al. (2018a)

A total of 101 plugs (12-45 cm length, 5 cm diameter) plugs were collected from 3 high-resolution (1-m interval) lateral transects and subsequently reprocessed for thin section petrography, powdered XRD analysis, helium porosity analysis, and core water flooding permeability analysis. In addition, 101 petrographic images were captured from thin sections using a Nikon 8000 ED Coolscan scanner and additional microphotographs were taken with an Olympus BX53MTRF petrographic microscope. The Choquette and Pray (1970) pore classification scheme was used to describe pore types. We used semiquantitative estimations on pore types abundances based on visual estimations charts published by Matthew et al. (1991)

Porosity measurements of the outcrop were obtained using a helium porosimeter from 101 1 x 1-inch cylindrical plugs at Kansas University. Permeability values were obtained via a core water flooding permeameter (Ghosh 2013) from 27 1 x 1-inch plug samples in the Texas A&M Harold Vince Department of Petroleum Engineering. 5 plugs were oriented horizontally (parallel to the bedding surface), whereas 22 plugs were oriented vertically (perpendicular to the bedding surface). A system of injection pumps, core holders, hydraulic accumulators, hydraulic accumulators, and pressure regulators were used to determine the permeability of each sample by measuring the pressure

differential between the upstream and downstream pressures on either side of the core and utilizing the Darcy equation:

$$K = \frac{Q\mu L}{A\Delta P}$$

Where K = permeability, Q = flow rate, μ= fluid viscosity, L = core length, A = core cross sectional area, and ΔP= pressure differential between the upstream and downstream pressure on either side of the core. Distilled water was used, and flow rate is carefully controlled using digital flow meters.

4.3.2. Digital outcrop model and clinoform geometries

A digital outcrop model (DOM) (**Fig. 4-1**) was produced from high-resolution orthomosaics and GigaPan Images for stratigraphic analysis. A combination of drone-based and traditional field description image sets was acquired to construct 3D outcrop models using photogrammetry techniques with a 1.2 cm/pixel resolution. Data to build the models were obtained via customized UAV flights from a commercial vendor. Photogrammetry models were calibrated with Trimble r10 and netR9 RTK GPS/Glonass setup for surveying field sites, which allowed for <10 cm/pixel resolution. The DOM contains 563 876 points and measures 810 m x 463 m, with the highest point at 55 m.

A 3D digital outcrop model was created for this study which allowed detailed geometrical measurements (at ~10 cm resolution) of the clinoform deposits. The geometrical measurements were taken to capture variations in clinoforms scale, internal facies boundaries, and dolomite body location with their corresponding petrophysical

properties. Also, these data were used to constrain multiple stochastic realizations of 3D surface-based geological models at a similar scale to the outcrop (~interwell scale).

Clinoform dimensions were obtained and recorded from detailed measurements of clinoform heights, clinoform lengths, clinoform bottom, and top angles (**Fig. 4-4**) from the digital outcrop model (DOM). Clinoform length is defined as the distance between the base terminations of one clinoform to the top termination intersecting the unconformity and represents a minimum length (as clinoforms continue to variable depths down to the volcanic basement beneath the level of the wave-cut platform). Clinoform height is defined as the vertical distance between the top termination intersecting the unconformity of a clinoform to base termination intersecting the wave-cut platform. Clinoform spacing is defined as the horizontal length between the base termination of two successive clinoforms (**Fig. 4-4**). Clinoform bottom angle (also referred to as toe angle) is defined as the angle between the horizontal base termination and the clinoform boundary, whereas clinoform top angle is defined as the angle between the horizontal top termination and the clinoform boundary.

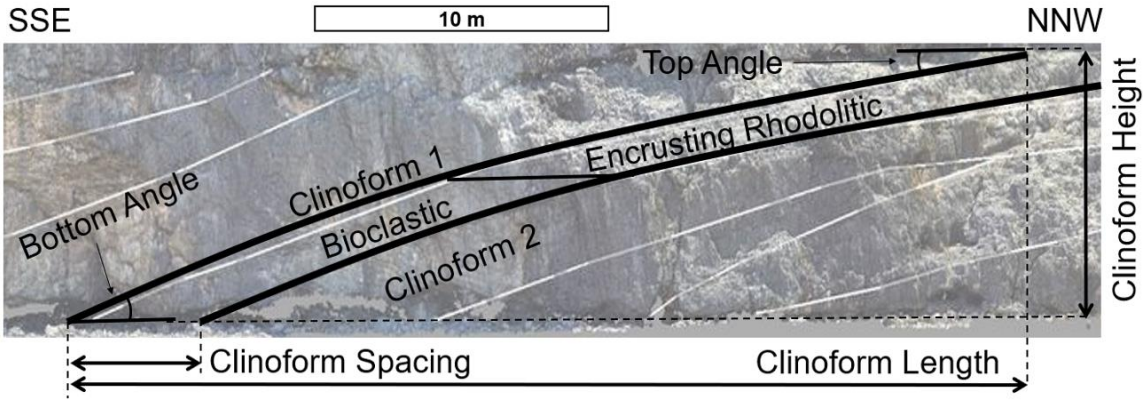

Figure 4-4: Simplified diagram showing different clinoform geometry parameters measured on outcrop.

Outcrop geometry quantifications are plotted to obtain distributions of best fit for each clinoform measurement. Clinoform dimensions, spacing, and angles are then stochastically sampled from their respective distributions to produce multiple stochastic realizations of surface-based reservoir models at a similar scale to the outcrops (grid-cell to interwell scale).

4.3.3. Surface-based modelling

Surface-based modelling and simulation is an approach to subsurface modelling that represents all heterogeneity that will impact flow by its bounding surfaces (Jackson et al. 2014; Jacquemyn et al. 2019). By using grid-free surfaces (Jacquemyn et al. 2019) that do not depend on a pre-defined grid, no compromises need to be made in terms of the resolution and thus, small features are preserved that would otherwise be lost (e.g.,

sub-grid cell size baffles or fluid pathways). The surface-based model thus provides a geologically and geometrically realistic representation of the heterogeneity whilst preserving connectivity. Models are built hierarchically, subdividing the model further until all relevant heterogeneity is represented (Jacquemyn et al., 2019). Hierarchy is derived from outcrop observations (e.g. dolomite bodies are confined in clinothems). Internally geological domains bounded by surfaces can thus be considered homogeneous, and additional internal surfaces are introduced if further spatially-correlated heterogeneity exists (Osman et al. 2020).

Surface templates are designed based on outcrop observations or geometrical concepts. These templates are then scaled, shaped, and transformed by a set of parameters that can ideally be measured directly from outcrop or be derived from geometrical databases (Jacquemyn et al., 2019). Where possible, parameters are expressed relative to the level of hierarchy they represent, for example, clinoform dip and spacing, facies boundary position is defined as fraction of clinothem height, to minimize interference between scenarios at different scales. Multiple stochastic realizations are built by sampling parameter distributions observed in outcrop.

Based on the outcrop description, 3D geometrical templates are created to represent the different features, i.e. clinoforms (**Fig. 4-4**), facies boundaries and dolomite bodies. The cross-section template for clinoforms is directly based on the outcrop and is shaped by its spacing, height, angle at the top, and angle at the toe (**Fig. 4-4**). A linear map view trajectory of the clinoforms is used, based on GPR data captured behind the main vertical outcrop (Bowling et al., 2018). Facies boundaries within clinoforms are

challenging to distinguish from the outcrop directly. Therefore, an offshore-dipping planar cross section template for these facies boundaries is used, combined with the clinoform map view trajectory. The position and dip of the facies boundary is defined by the height of its intersections with bounding clinoform surfaces. Similarly, the shape of dolomite bodies cannot be clearly derived from the outcrop. An elongated ellipsoidal shape is used consistent with Simms (1984), which is tilted parallel to clinoform surfaces. Multiple dolomite bodies will be introduced to increase the dolomite proportion in the model.

4.3.4. Surface-based dynamic flow simulation

Flow simulations are run in IC-FERST, which solves flow using double control volume finite elements on dynamically adapting unstructured tetrahedral meshes (Jackson et al., 2015; Salinas et al., 2017a; Salinas et al., 2017b). The grid-free surface-based representation is discretized by an unstructured tetrahedral mesh that conforms to the geometry and thus preserves any surfaces that represent heterogeneity (in this case, dipping clinoform surfaces, facies boundaries and dolomite bodies). Because the mesh is unstructured, it allows the use of small elements for small features where needed, but also very large elements where possible, without affecting resolution elsewhere in the model. Using conventional pillar-grids and rectangular grid cells would result in either stair-stepping of the clinoforms and dolomite body surfaces (or any other dipping or curved surface) or very skewed grid cells that would drastically limit the quality of the simulation results. Dynamic mesh optimization will update the mesh throughout

simulation to optimize flow results, by locally refining (e.g. around waterfront, pressure drops) and coarsening where possible (Salinas et al. 2018). Mesh refinement ensures high quality simulations, while coarsening reduces element count and thus improves simulation efficiency.

4.3.5. Flow simulation - Rock-fluid properties and production scheme

Lateral waterflooding simulations between opposing model sides are set up to test the impact of different degrees of dolomitization on fluid flow behavior. Because outcrop data is mainly parallel to depositional dip, flow simulations are executed along depositional dip direction. Initially, the model is oil-filled, and water is injected from one face (updip) at a fixed pressure and fluids are produced from the opposite face (downdip) at a fixed pressure. All other faces are assumed no-flow boundaries. The pressure differential is set to 70 kPa/m. As average permeability will vary drastically with increasing degrees of dolomitization, simulations are run up to 15 years to ensure water breakthrough is reached for all simulations. Water breakthrough is achieved when any part of the water-front originating from the injection face intersects with any part of the production face. Fluid properties and relative permeability properties are summarized in **Table 4-1**.

Table 4-1: Overview of fluid, rock and simulation properties

Fluid properties	**Water**	**Oil**
Density [kg/m^3]	1000	800
Compressibility	Incompressible	Incompressible
Viscosity [P]	0.001	0.004
Rel. perm. max	0.3	0.8
Rel. perm. Corey exponent	2	2
Immobile fraction	0.2	0.2
Boundary conditions		
Injection phase %	100	0
Injector	West face	
Injection pressure [Pa]	6.0E+07	
Producer	East face	
Production pressure [Pa]	3.0E+07	
Pressure gradient [Pa/m]	7.0E+04	

Figure 4-5 shows a summary of the workflow used for this end-to-end methodology for surface-based geological modelling and subsurface flow characterization. A schematic diagram summarizing the dimensions, flow boundaries, and overall configuration of the different facies can be seen in **Figure 4-6**.

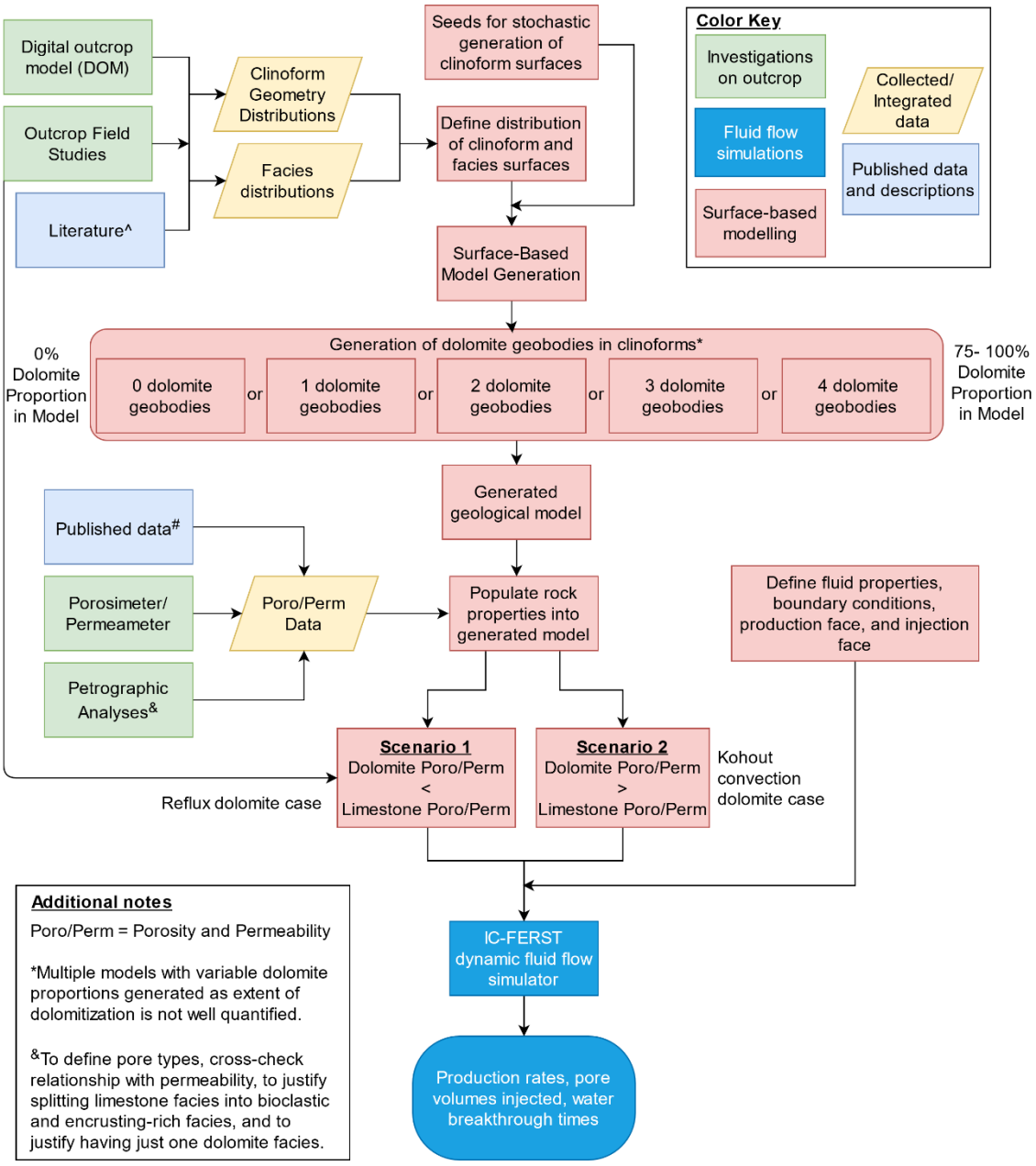

Figure 4-5: Flow chart of workflow used for holistic end-to-end methodology for geological modelling and subsurface flow characterization using surface-based modelling and fluid flow simulations. ^Laya et al. (2018), Laya et al. (2021), and Simms et al. (1984). #Budd and Mathias (2015), Lucia and Major (1994), and Ehrenberg et al. (2006).

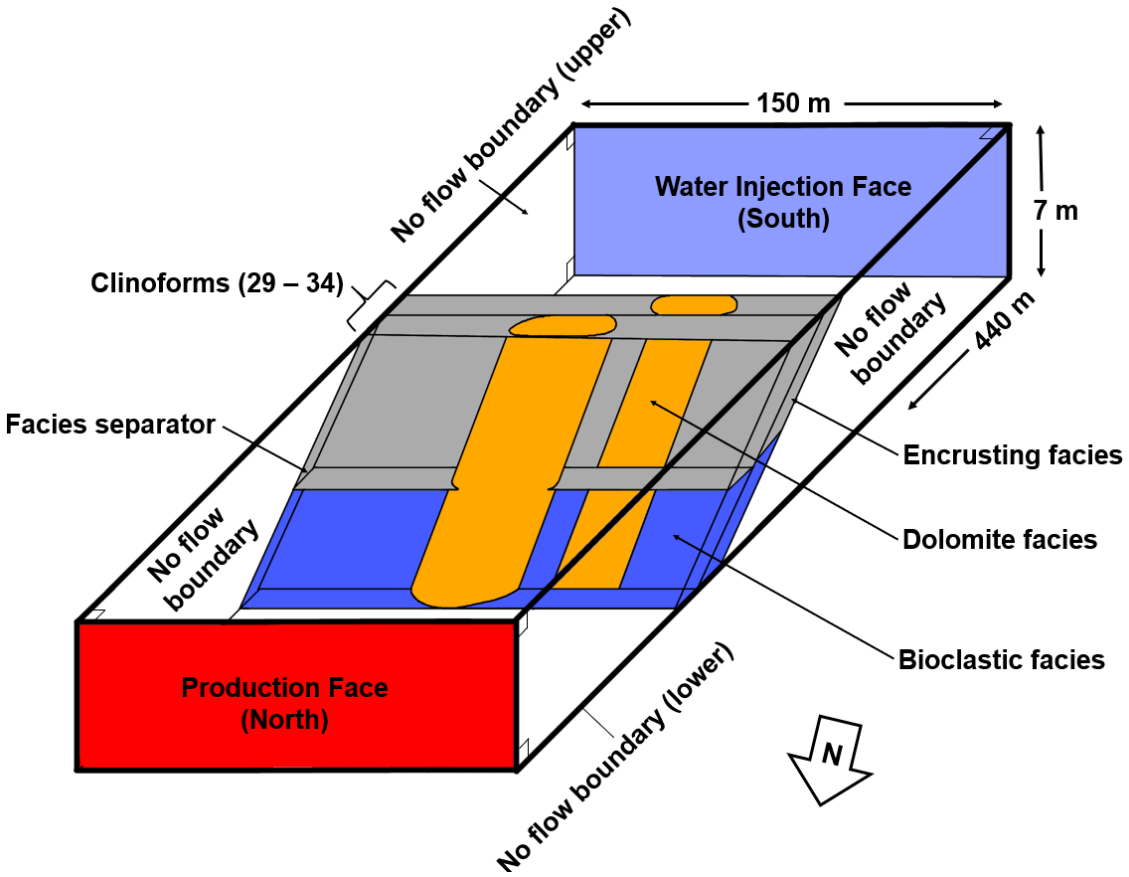

Figure 4-6: Schematic of generated surface-based geological model, showing dimensions of model, flow boundaries, production face, injection face, and general configuration of facies within clinoforms.

4.4. Results

4.4.1. Clinoform dimensions

A total of 32 clinoforms with variable bed-geometries are identified in the Seru Grandi outcrop, with an east/southeast dip. The clinoform dimensions are summarized (**Fig. 4-7**) with their distributions fitted to probability distributions (**Table 4-3**). Clinoform spacing mostly closely fit a gamma distribution, with a median of 11.4 m, standard deviation of 13.1 m, and a mean of 16.0 m. Clinoform length shows a close fit

with a lognormal distribution, with a median of 30.8 m, standard deviation of 13.2 m, and a mean of 33.0 m. Clinoform height fits best with a normal distribution, with a median of 8.7 m, a standard deviation of 1.7 m, and a mean of 8.8 m. Clinoform toe angles and top angles both show best fit with chi distributions, with medians of 16.4° and 12.2° respectively, standard deviations of 8.0 m and 7.2 m respectively, and means of 17.4° and 13.1° respectively.

Table 4-2: Probability distributions of best fit and associated distribution

	Spacing	**Length (m)**	**Height**	**Bottom angle**	**Top angle**
Distribution	Gamma	Lognormal	Normal	Chi	Chi
μ/A	1.1	3.4	8.8	-	-
σ/B	14.0	0.4	1.7	13.5	10.5

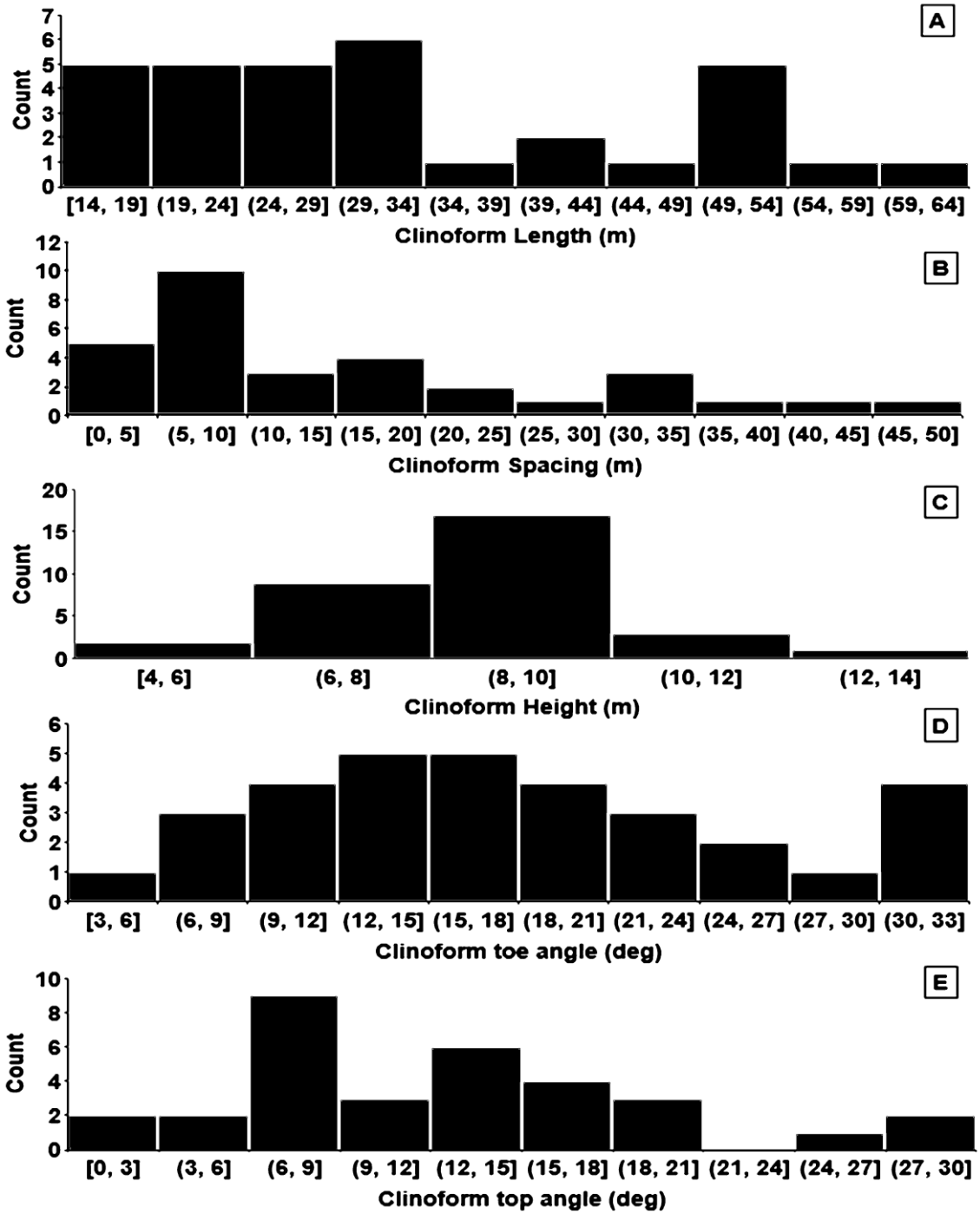

Figure 4-7: Histograms of clinoform outcrop measurements, count referring to frequency of a range of measurements. A) Clinoform length; B) Clinoform spacing; C) Clinoform height; D) Clinoform toe angle; E) Clinoform top angle.

4.4.2. Limestone and dolomite facies descriptions

The Seru Grandi clinoforms contain two clearly identifiable facies within the context of this study; an encrusting red algae/rhodolith rich facies with boundstone and packstone textures which is generally located within the updip sediments of individual clinoforms, and a bioclastic facies with grainstone and packstone textures generally located within the downdip sediments. In both facies, coralline red algae are the dominant component, with minor amounts of coral fragments, foraminifera, and echinoids. Micritic mud is observed filling the intergranular pore spaces as a matrix component.

In dolomitized sections, replacement dolomite often occurs as anhedral to subhedral crystals (<15 μm) mimetically replacing coralline red algae, foraminifera, and echinoid grains. Within updip sediments, dolomite crystals appear coarser (15 – 80 μm) with more subhederal to euhedral habits. Pore-filling dolomite cements are also more common within updip sections relative to downdip sediments, with the largest (100 – 400 μm) dolomite crystals observed closest to the unconformity separating the progradational platform from the flat-topped platform (**Fig. 4-2 C**). A more thorough description of the limestone and dolomite facies described herein can be found in Laya et al. (2018a) and Laya et al. (2021) respectively.

4.4.3. Porosity and permeability of Seru Grandi outcrop

In the bioclastic facies (**Fig. 4-8, A)**, interparticle porosity make up the bulk of observed pore types (50%), with lesser amounts of moldic (35%) porosity, and intraparticle porosity (15%) (**Fig. 4-9**). Interparticle and moldic porosity is generally poorly connected with mostly isolated pores. In the encrusting red algae rich facies (**Fig. 4-8, B**), intraparticle porosity makes up 50% of all observed pore types, with moldic porosity and interparticle porosity both making up 25% of all observed pore types. Similar to what was observed in the bioclastic facies, none of the pore types appear to be well connected. These two facies are calcitic based on XRD analyses. Based on these pore characterization and textural observations, we define two limestone facies for the simulations in this study. In dolomitized samples, pore types and distributions tend to homogenize only intracrystalline and interparticle porosity occurrence (**Fig. 4-9, C, D**). Thus, for simulations and the objective of this study, we combined all dolomitized facies into just one facies.

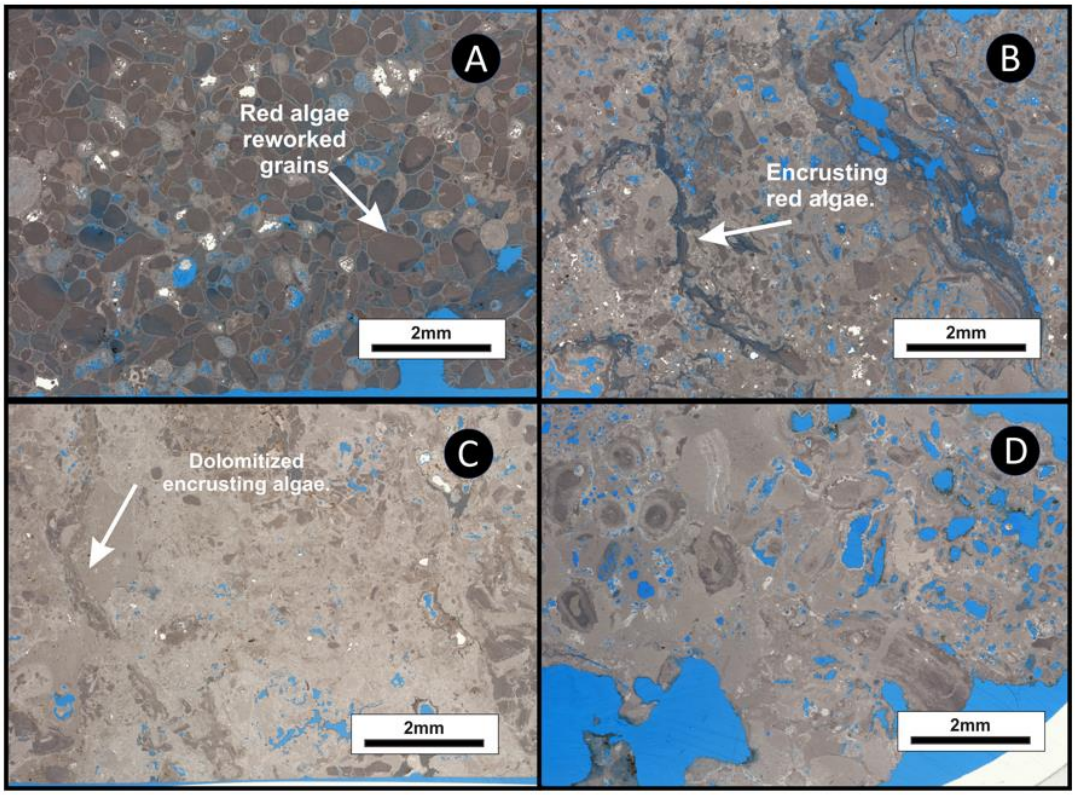

Figure 4-8: Thin section images from facies associated with clinoforms at Seru Grandi outcrop. A) Bioclastic facies, displaying a largely grainstone to packstone texture. B) Encrusting red algae facies, displaying largely boundstone to packstone texture. C), D) Dolomitized encrusting facies and dolomitized bioclastic facies respectively; dolomitization is mostly non-fabric destructive, with pervasive changes in overall color, and some pore-filling dolomite cements.

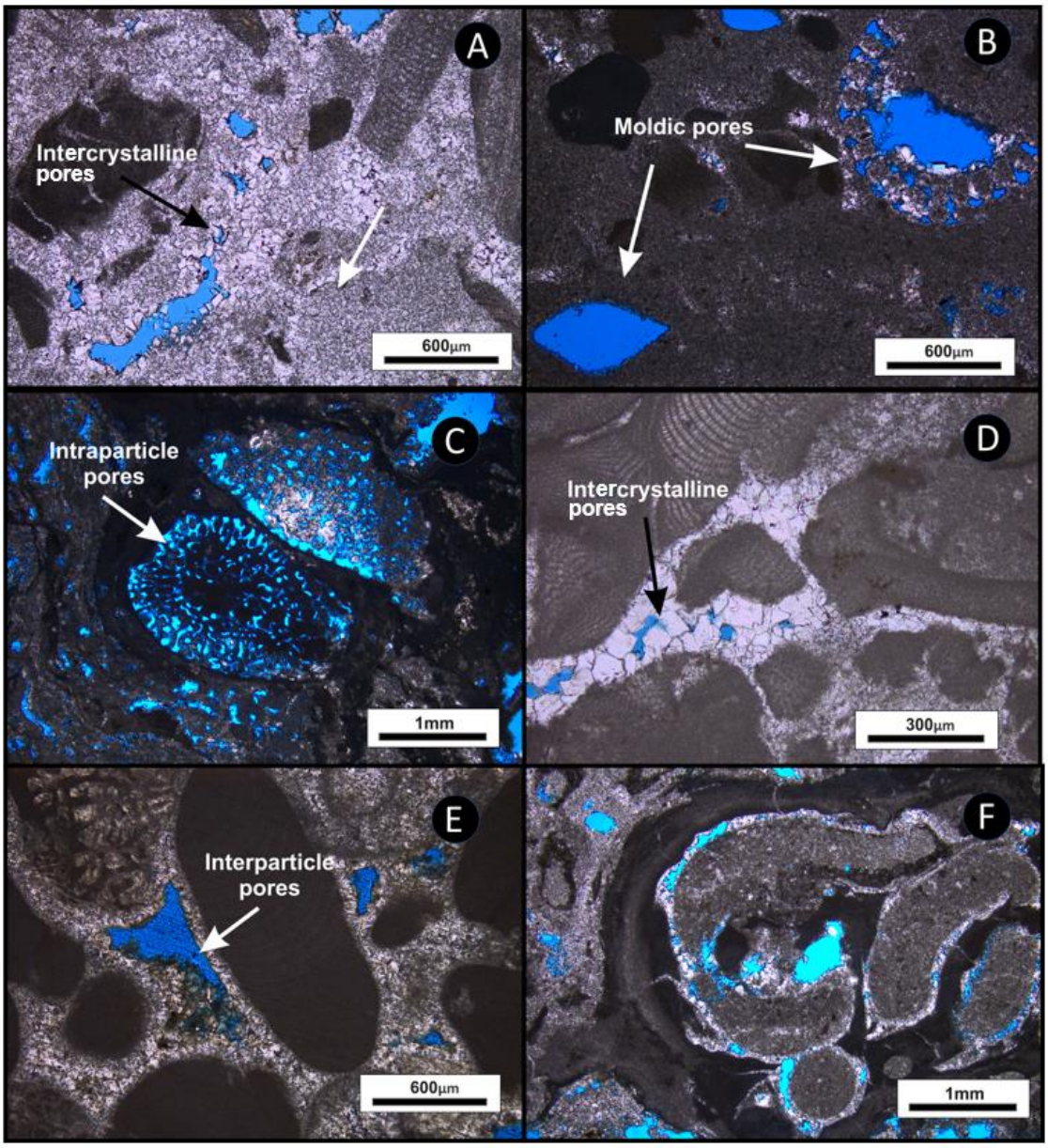

Figure 4-9: Pore types identified in Seru Grandi clinoforms . A) Intercrystalline porosity within a fully dolomitized bioclastic facies sample. Largest crystals typically within moldic pores; B) Moldic porosity within a bioclastic facies sample. No preferentially dissolution noted within the different bioclasts noted. C) Intraparticle porosity within an encrusting facies sample. Example shown is of a benthic foraminifera. D) Intercrystalline porosity within a fully dolomitized bioclastic facies sample. Note the fabric preservation of coralline red algae clasts, with original microstructures still clearly discernible. E) Interparticle porosity within a bioclastic facies sample. F) Mixture of interparticle and intraparticle porosities within an encrusting facies sample.

Porosity from core plugs varies from 4-24% (Standard deviation (SD) = 4.23), whereas permeability measurements show values ranging from 0.02 mD to 17 mD (SD = 3.48) for Seru Grandi samples (Fig. 8; Laya et al, 2021). When split by facies, encrusting facies have similar permeabilities (0.028 mD, SD = 0.15) compared to bioclast facies (0.030 mD, SD = 0.02), whereas bioclast facies have on average lower porosity values (7.1%, SD = 2.48) than encrusting red algae facies (10.3%, SD = 3.25). Within the dolomite facies, porosity and permeability is marginally higher (10.8%, 0.048 md) than either limestone facies (**Table 4-3**).

Table 4-3: Porosity and permeability data of Seru Grandi outcrop.

Sample	Facies	Mineralogy	Permeability (mD)	Porosity (%)
Line 1 SG1	Encrusting	Dolomite	0.04	9.1
Line 1 SG12	Encrusting	Dolomite	0.6	7.3
Line 1 SG18	Encrusting	Dolomite	0.01	10.9
Line 1 SG24	Bioclastic	Dolomite	0.01	11.4
Line 1 SG28	Bioclastic	Dolomite	4.87	14
Line 1 SG32	Encrusting	Dolomite	17.67	24.6
Line 1 SG34	Encrusting	Dolomite	0.07	10
Line 1 SG36	Encrusting	Dolomite	0.04	14.5
Line 1 SG39	Encrusting	Dolomite	0.06	10.4
Line 1 SG6	Bioclastic	Dolomite	0.03	9.1
Line 1 Wedge2	Encrusting	Limestone	0.06	6.2
Line 2 SG10	Bioclastic	Dolomite	0.01	13.2
Line 2 SG16	Encrusting	Dolomite	0.01	6
Line 2 SG23	Bioclastic	Dolomite	0.004	5.9
Line 2 SG28	Bioclastic	Dolomite	0.09	13.2
Line 2 SG35	Bioclastic	Dolomite	0.01	9.2
Line 2 SG39	Bioclastic	Dolomite	0.01	7.9
Line 2 SG42	Bioclastic	Dolomite	0.27	11.7
Line 2 SG45	Bioclastic	Dolomite	0.03	6.5
Line 2 SG6	Bioclastic	Dolomite	0.41	5.3
Line 3 SG11	Bioclastic	Limestone	0.06	6
Line 3 SG12	Encrusting	Limestone	0.01	7
Line 3 SG2	Bioclastic	Limestone	0.004	4.4
Line 3 SG4	Bioclastic	Limestone	0.01	6.7
Line 3 SG6	Bioclastic	Limestone	0.07	9.6
Line 3 SG8	Encrusting	Dolomite	0.06	15.3
Line 3 SG9	Encrusting	Limestone	0.01	9

4.4.4. Defining porosity and permeability for geological model and flow simulations

Seru Grandi's porosity and permeability measurements were compared with other published data from Bonaire for a more robust understanding of the petrophysics and reliable data to use in our simulations. Data from other Bonaire outcrops (**Fig. 4-1**) of similar age and lithology including Goto Meer and Dos Pos from Lucia and Major (1994a) and detailed Dos Pos outcrop sampling from (Budd and Mathias 2015) were combined with our Seru Grandi dataset **(Fig. 4-10**). Our dataset overlaps with previously published datasets but shows a distinctly lower mean porosity and permeability.

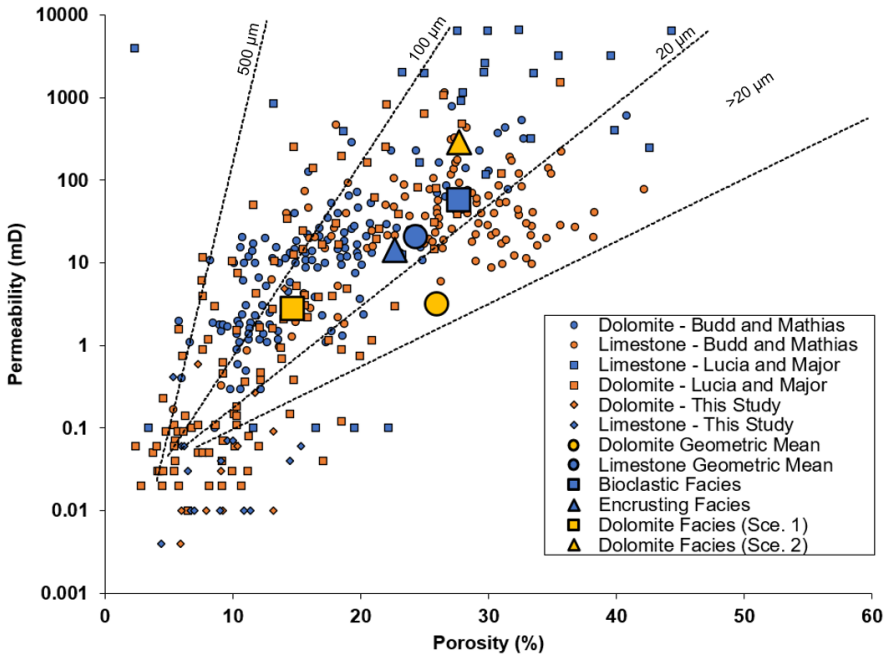

Figure 4-10: Porosity and permeability crossplot for Bonaire limestone and dolomite samples, with their respective means. Porosity and permeability values used in this study indicated as enlarged square and triangle markers. Sce. 1 = Scenario 1. Sce. 2 = Scenario 2. Porosity-permeability fields as defined by Lucia (1995) included. Data from this study, Budd and Mathias (2015), and Lucia and Major (1994).

In the combined literature and our own results, Bonaire limestone samples have a mean porosity of 25.2% and a geometric mean permeability of 28.5 mD. Petrophysical results for limestone facies derived from the literature are not linked to facies descriptions. Based on the petrographic descriptions and porosity and permeability distributions in Seru Grandi limestones, the encrusting facies is expected to have lower flow properties than bioclastic limestone facies. To reflect this difference between facies, a modifier of –10% and 50% is applied to the average Bonaire limestone porosity and permeability respectively for the encrusting facies (22.7%, 14.3 mD), whereas a modifier of +10% and 100% is applied to the average Bonaire limestone porosity and permeability respectively for the bioclastic facies (27.7, 57.0 mD). Bonaire dolomite samples have a mean porosity of 14.7% and a geometric mean permeability of 2.7 mD and is assumed to be independent of their precursor limestone **(Table 4-4**). These values form the porosity and permeability conditions used for all Scenario 1 simulations, wherein dolomite bodies have lower porosity and permeability values than their equivalent limestone precursors.

Table 4-4: Mean porosity and permeability values for all limestone facies and dolomite facies in Bonaire based on measurements from this study, Lucia and Major (1994), and Budd and Mathias (2015).

	Scenario 1		Scenario 2	
Facies	**Porosity (%)**	**Permeability (mD)**	**Porosity (%)**	**Permeability (mD)**
All limestone	25.2	28.5	25.2	28.5
Bioclastic	27.7	57	27.7	57
Encrusting/Rhodolitic	22.7	14.3	22.7	14.3
Dolomite	14.7	2.8	27.7	285

Scenario 2 considers a situation where dolomitization improves flow properties is considered. In this scenario, dolomite permeability is increased 1000%, and porosity increased by 10% (27.7%, 285 mD) relative to mean limestone values (25.2%, 28.5 mD) based on porosity and permeability observations from Ehrenberg et al (2006) (**Supplementary figure 2**). Porosity and permeability values for each scenario are listed in **Table 4-4.**

4.4.5. Surface-based geological models

Multiple realizations of surface-based models are generated from the geometrical templates of clinoforms, facies boundaries (**Fig. 4-4**) and ellipsoidal dolomite bodies. Clinoform surfaces are shaped based on the distribution of measured outcrop parameters listed in **Table 4-3**. As the position and dip of facies boundaries and size of dolomite

bodies cannot be clearly derived from DOM directly, these are based on qualitative outcrop observations and assumptions summarized by the distributions listed in **Table 4-2**. Outcrop sampling indicates the facies boundary between bioclastic and encrusting/rhodolitic facies sits roughly halfway of the clinoform height, slightly dipping offshore. Overall dolomite proportions are varied by changing the number of dolomite bodies per clinothem between 0 and 4. Respective dolomite body size distributions are chosen to increase the overall dolomite proportion by 20% when an additional dolomite body is added to each clinothem (**Fig. 4-11 c-f**). The geometrical parameter distributions are then sampled stochastically to shape individual surfaces when they are inserted into a model realization.

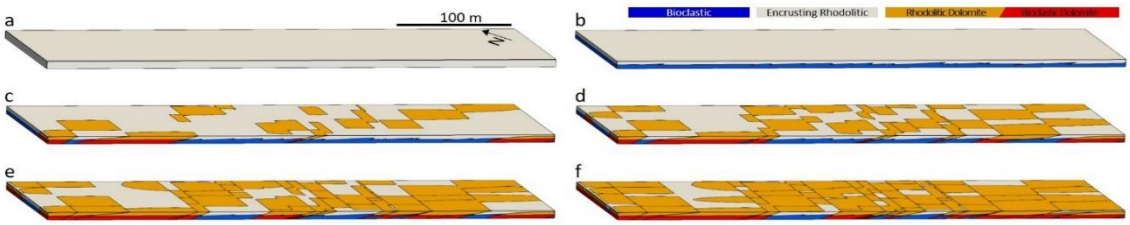

Figure 4-11: Overview of surface-based modelling workflow. a) Model boundary; b) clinoforms and facies boundaries added; c) 1 dolomite body added per clinothems; d) 2 dolomite bodies added per clinothem; e) 3 dolomite bodies added per clinothem; f) 4 dolomite bodies added per clinothem.

Models cover a similar domain as the outcrop, measuring 440 m long, by 150 m wide, by 7 m high (**Fig. 4-5 a**). Surfaces are inserted into the model hierarchically and sequentially. First, all clinoforms surfaces are successively placed in the model, subdividing the model domain into clinothem volumes. Clinothem volumes are then further subdivided by facies boundary surfaces, that separate the lower (bioclastic; blue) and upper (encrusting/rhodolitic; light-grey) parts of the clinothems (**Fig. 4-11 b**). Dolomite body bounding surfaces then subdivide each of the facies volumes into dolomitized (inside dolomite bounding surfaces) and non-dolomitized (outside dolomite bounding surfaces) domains. This results in separate volumes for bioclastic, dolomitized bioclastic, encrusting rhodolitic and dolomitized encrusting/rhodolitic facies (**Fig. 4-11 c-f**).

As no clear petrophysical difference is observed between dolomitized bioclastic facies and dolomitized encrusting algal-rich facies, these are merged into single dolomite bodies (**Fig. 4-12**). No spatial short or long-range patterns are observed in petrophysical properties of the Seroe Domi limestone facies (Budd & Mathias, 2015). As non-spatially correlated variability of porosity and permeability has limited impact on flow (Jennings Jr and Ward 2000; Osman et al. 2020), no further modelling of porosity and permeability is necessary. Dolomite petrophysical properties exhibit a lateral oscillatory pattern of ~16 m (Budd & Matthias, 2015), which is equal to measured clinoform spacing average (mean for gamma distribution: 15.4m; **Table 4-3**). Therefore, we can assume this pattern is the result of dolomite being bound in and individual clinoform and no further

heterogeneity modelling is needed within dolomite bodies, and a uniform porosity and permeability is assigned.

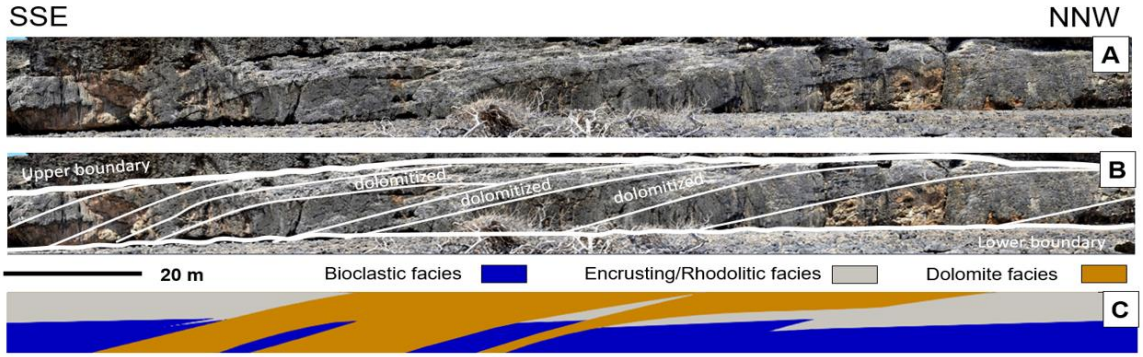

Figure 4-12: Visual comparison of a section of Seru Grandi outcrop with one of the model realization cross sections, showing reproducibility of the complex clinoform geometries within the models.

In total 10 stochastic realizations were made representing clinoforms and facies boundaries only, using a seed number for the random number generator to ensure the same model could be repeated. In each of these realization, clinoform spacing, length, height and angles were varied (sampled from the distribution obtained from outcrop analysis). For each realization, the number of dolomite bodies was increased step-by-step from 0 to 4 dolomite bodies per clinothem. This totals 50 different models, plus 1 to represent complete dolomitization.

4.4.6. Flow simulations and results

4.4.6.1. Scenario 1: Dolomitization reducing flow properties

In the studied outcrop (Scenario 1), dolomitization has caused a reduction in porosity (-58%) and permeability (-90%) from its precursor limestone (refer to **Table 4-4**). The oil production rate of non-dolomitized clinoforms show a gradually increasing plateau level until water breakthrough occurs at around 2.5 years (**Fig. 4-13 a**). At breakthrough, oil production rates drop steeply and is followed by a gradual decrease. After 10 years of production, a second drop in production rate is present. With increasing dolomite proportions, the observed plateau rates are reduced, and water breakthrough is delayed up to 12 years for very high dolomite proportions of 89%. After breakthrough, the decline in oil production rate is more gradual and often consists of multiple steps rather than a smooth decrease. Cumulative oil production (**Fig. 4-13 c**) evolution over time shows linear behavior to breakthrough, followed by an initial sharp break at 2.5 years, and a second more gentle break at approximately 10 years. With increasing dolomite proportion, the cumulative production curves are smoothed (no more sharp breaks) and tend to a completely linear behavior for the full production interval.

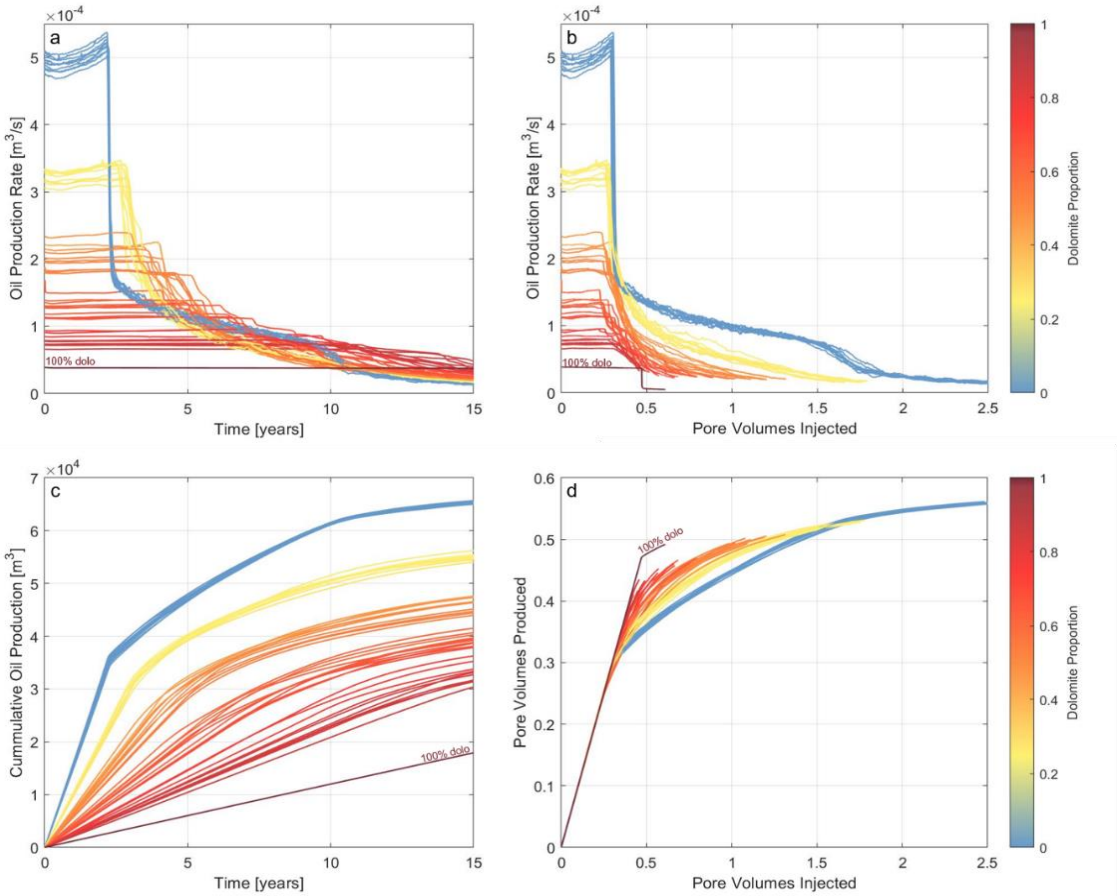

Figure 4-13: Production curves for Scenario 1 for different dolomite proportions. a) Oil production rate versus time. b) Oil production rate versus pore volumes injected (PVI). c) Cumulative oil production versus time. d) Pore volumes of oil produced (PVP) versus pore volumes injected (PVI).

The production rate versus pore volumes injected (PVI) shows behavior which is independent of applied pressure gradient relative to the absolute permeability values (**Fig. 4-13 c, d**). The production rates decrease as more dolomite bodies are introduced into the models, and post breakthrough production drops are more gradual and with multiple steps. The time of breakthrough varies around 0.28 PVI, independent of dolomite proportion. The number of pore volumes of oil produced show same linear

behavior until around 0.28 PVI (**Fig. 4-13 d**). When no dolomite is present a clear break is visible at breakthrough. With increasing amounts of dolomite, this approximately linear trend is continued for longer; thereby producing more oil per volume of water injected.

Breakthrough time shows an exponentially increasing relationship with dolomite proportion in the clinoforms (**Fig. 4-14 a**). This is related to the exponentially decreasing oil production rate at water breakthrough (**Fig. 4-14 c**). No clear trend can be observed when comparing breakthrough time or oil production rate versus pore volumes injected (**Fig. 4-14 b, d**). Pore volumes injected at breakthrough vary around 0.28(±0.03) PVI. However, the range of pore volumes injected (PVI) at time of breakthrough increases with increasing dolomite proportion; linear clusters appear for different ranges of dolomite proportions and number of dolomite bodies. For example, the breakthrough time for models with 4 dolomite bodies (76-88% dolomite) shows a linearly increasing trend versus PVI (**Fig. 4-14 b**). The production rate does not clearly vary with PVI at breakthrough (**Fig. 4-12 d**).

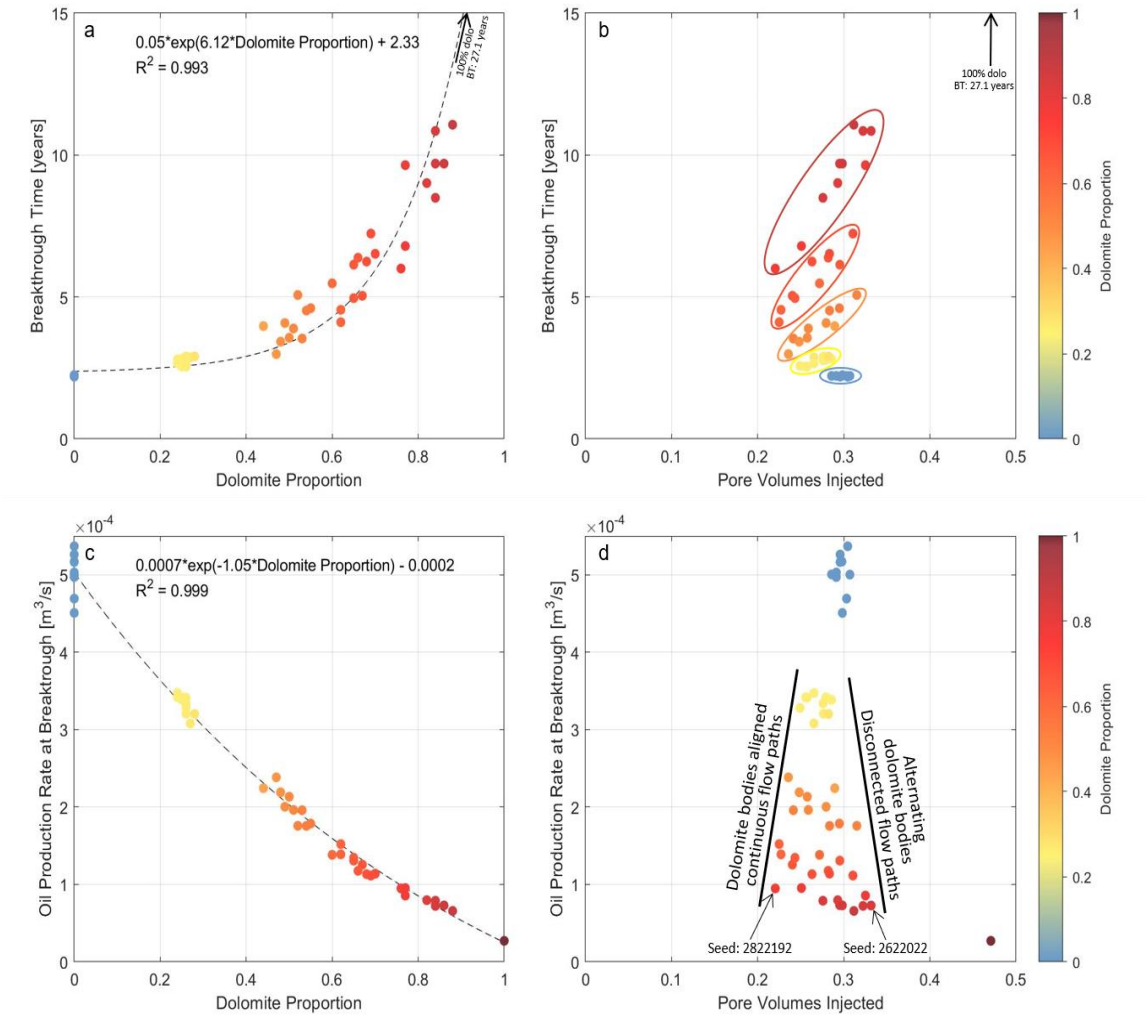

Figure 4-14: Cross plots of dynamic properties at breakthrough for Scenario 1. a) Breakthrough time shows an exponential relationship with dolomite proportion. b) Breakthrough times are not clearly correlated with PVI at breakthrough, however linear clusters can be distinguished by the number of dolomite bodies. c) Oil production rate at breakthrough (proxy for production plateau level) decreases exponentially with dolomite proportion. d) Oil production rate at breakthrough is not correlated with PVI. The range of PVI at breakthrough increases with dolomite proportion.

The amount of remaining oil (**Fig. 4-13 d**; oil remaining = 1 – PVP) at breakthrough varies between 56% and 70% and reaches 44% to 56% at the end of simulation time (15 years). The remaining oil increases with increasing dolomite proportions. In map view (**Fig. 4-17 a, b**) the waterfront moves shows extended fingers along continuous limestone occurrences and bypassed oil is located where dolomite bodies are spatially clustered, surrounded by continuous flow paths through limestone.

4.4.6.2. Scenario 2: Dolomitization improving flow properties

Dolomitization can cause an increase in porosity and permeability relative to its precursor limestone. In Scenario 2, dolomite porosity is increased by 10%, and permeability increased 1000% relative to the mean limestone properties (**Table 4-3**). The flow results are compared again to the undolomitized case (blue lines, **Fig. 4-15**), showing a breakthrough around 2.5 years and 0.3 PVI (**Fig. 4-15 a & Fig. 4-16 a**). With increasing dolomite proportions, the observed production rates are increased, and water breakthrough occurs earlier, as early as 0.58 years at dolomite proportion of 89%. For lower dolomite proportions (<50%) the decline in oil production rate shows multiple steps, rather than a smooth decrease at higher dolomite proportions (>50%). Cumulative oil production (**Fig. 4-15 c**) shows a smoother evolution when dolomite is partially present relative to simulations at 0% or 100% dolomite proportions. With increasing dolomite proportion, cumulative production shows a decreasing amount of spread between production values; i.e. the difference of flow behavior between 0 and 20% is much greater than the difference between 60 and 80%.

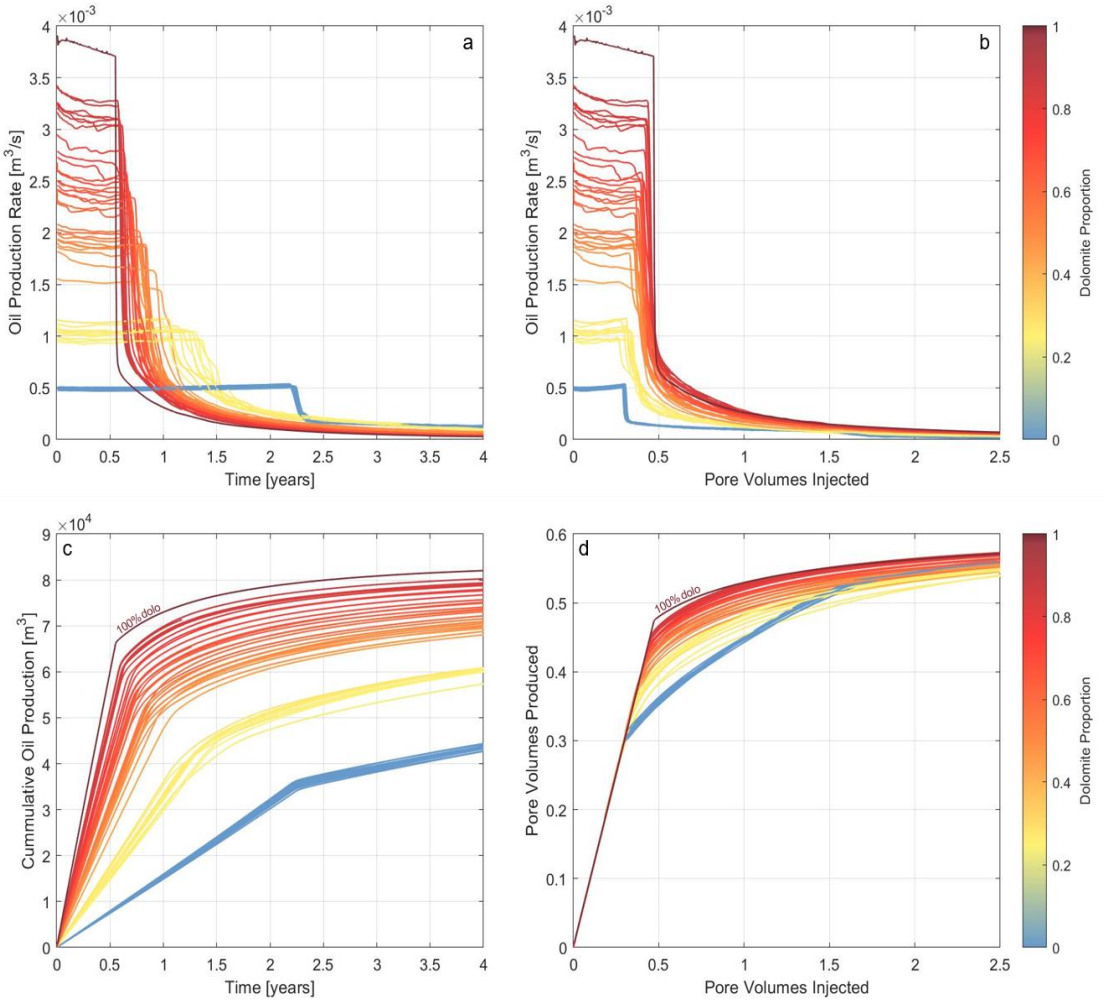

Figure 4-15: Production curves for Scenario 2 for different dolomite proportions. a) Oil production rate versus time. b) Oil production rate versus pore volumes injected (PVI). c) Cumulative oil production versus time. d) Pore volumes of oil produced versus pore volumes injected.

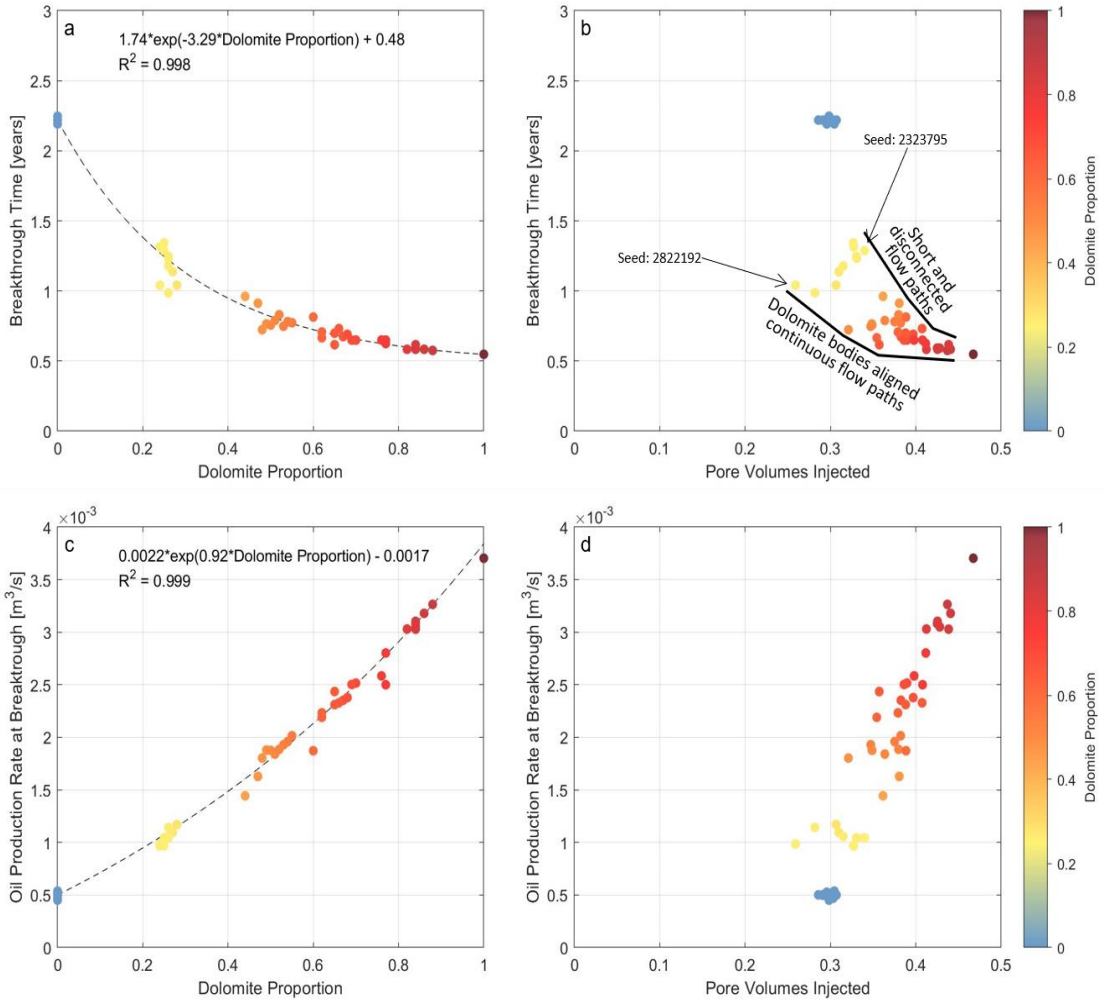

Figure 4-16: Cross plots of dynamic properties at breakthrough for Scenario 2. a) Breakthrough time shows an exponential relationship with dolomite proportion. b) Breakthrough times show a decreasing trend with PVI at breakthrough; however, results are spread out for low dolomite proportions (<50%) and converge for higher proportions. c) Oil production rate at breakthrough (proxy for production plateau level) increases exponentially with dolomite proportion. d) Oil production rate at breakthrough linearly increases with PVI. The range of PVI at breakthrough decreases with dolomite proportion.

The production rates versus PVI (**Fig. 4-15 b**) shows the breakthrough increases from 0.3PVI without dolomite to 0.44PVI at 89% dolomite. Plotting pore volumes produced (PVP) versus pore volumes injected (PVI) (**Fig. 4-15 d**) shows an increase of recovery with increasing dolomite proportion. However, at lower dolomite proportions (~20%) recovery factor falls below undolomitized cases when PVI is greater than ~1.3. Water breakthrough times show an exponentially decreasing relationship with dolomite proportion (**Fig. 4-16 a**) because of exponentially increasing production rates before breakthrough (**Fig. 4-16 c**). Breakthrough time in years show a decreasing trend with PVI (**Fig. 4-16 b**); however, for low dolomite proportions (~20 - 40%) the data is quite scattered and varies between 0.26 and 0.34 PVI. Overall, the sensitivity of flow metrics varies with dolomite proportion; increasing dolomite proportions increase the variation of PVI, decreases water breakthrough times, and increase the variance of production rates (**Fig. 4-16 d**).

The amount of remaining oil (**Fig. 4-15 d**; oil remaining = 1 – PVP) at breakthrough varies between 70% without dolomite to 53% when fully dolomitized. At end of simulation time (4 years), remaining oil is clustered around 44% +/- 2% . The amount of remaining oil decreases with increasing dolomite proportions. In map view (**Fig 4-17 a**, **b**) the waterfront moves faster along higher permeability dolomite, but overall a fairly continuous waterfront forms rather than elongated fingers in Scenario 1. Bypassed oil is mainly located in the upper part of the clinoforms in the rhodolitic facies, as flow preferentially sweeps the underlying bioclastic facies.

4.5. Discussion

4.5.1. Petrophysical properties variations and their relationship with dolomitization model.

Dolomitization can result in significant changes in the porosity and permeability of the host limestone (Murray 1960; Weyl 1960; Halley and Schmoker 1983; Schmoker et al. 1985; Lucia and Major 1994b). The facies composition (coralline algae dominated bioclastic grainstone to packstones) of both the Marion Plateau (case study used for Scenario 2 dolomites) and Bonaire (case study used for Scenario 1 dolomites) are highly similar, have a similar age (Miocene), paleoclimate (subtropical), and range of environments (Ehrenberg et al. 2006; Laya et al. 2018a; Laya et al. 2021). Despite these similarities, dolomite porosity and permeability values relative to limestone values are demonstrably vastly different between these two locales likely due to their very different dolomitization models: reflux dolomitization in the case of Bonaire, and geothermal convection dolomitization for the case of Marion Plateau.

Thus, when evaluating whether a dolomite geobody will have relatively higher or lower porosities and permeabilities relative to its host limestone, the model of dolomitization is a significant factor to consider. To illustrate this point, we will compare two reactive transport models with identical dimensions, at the same time scales, with the same limestone textural distributions, of an isolated carbonate platform: one with a reflux dolomitization scenario (Al-Helal et al. 2012), and another with a geothermal convection dolomitization scenario (Whitaker and Xiao, 2010). In the geothermal convection case, a larger dolomite geobody (~2 km deep, 20 km wide) is generated, with

only small (<10%) rock fractions of rock dolomitized (Figure 3, Whitaker and Xiao, 2010). In the reflux dolomitization case, a smaller (~1 km deep, 15 km wide) dolomite geobody is generated in the same time, with a greater proportion of the geobody with >90% dolomite rock fractions (Figure 5, Al-Helal et al. 2012). Additionally, the ratio of the area undergoing porosity creation is much higher when the dolomitization is produced by large-scale water circulation from geothermal convection as compared to dolomitization driven by reflux. Thus, in-line with the two dolomite poroperm scenarios tested in this study, the Bonaire dataset which reflects dolomites produced by reflux dolomitization (Scenario 1) will likely have lower porosities and permeabilities relative to the precursor limestone, whereas the Marion Plateau dataset which reflects dolomites produced by geothermal convection dolomitization (Scenario 2) will likely have higher porosities and permeabilities relative to the precursor limestone.

4.5.2. Role of dolomite geobodies in lateral flow

4.5.2.1. Scenario 1: Dolomitization reducing porosity and permeability

Scenario 1 reflects the porosity and permeability distribution based on the measurements of outcrop samples, in which dolomitized sample are on average 60% less porous and approximately an order of magnitude less permeable. This reduction in flow properties is clearly reflected in the waterflooding simulation experiments. As expected, flow rates decrease as more dolomite is present and water breakthrough is delayed (**Fig. 4-13 a, c**). In undolomitized clinoforms (100% limestone), all production curves are

close to identical (**Fig. 4-13 a, c**), and flow behavior can be subdivided into (1) early linear behavior when the majority of the flow is concentrated in the lower bioclastic facies; (2) a clear break at breakthrough, when the model-wide water front arrives at the opposite side and oil production rate drops as a consequence of sweeping of upper rhodolitic facies; and (3) a second break that indicates the water front has passed through the whole domain with another reduction in oil production rate related to the sweeping of remaining oil until irreducible saturation is reached.

Even at low dolomite proportions (<30%), this behavior changes as the sharp breaks are smoothed out. When low permeability dolomite is encountered, the waterfront is deviated around the dolomite bodies and splits into multiple fronts (which can also merge again further downstream). Additionally, more flow is forced upwards into the upper encrusting facies relative to undolomitized clinoforms. As a result, the second break present in undolomitized clinoforms is no longer visible, even at low dolomite proportions (**Fig. 4-13 c, d**). The break in production curves at breakthrough is still well-defined at low dolomite proportions (<30%) but gradually disappears as more dolomite is present.

Sweep efficiency increases with increasing dolomite proportions (**Fig. 4-13 d**). At higher dolomite proportions, higher pore volumes of oil are produced per pore volume water injected as a consequence of narrower or terminated fluid flow paths; in other words, these dolomite geobodies focus more flow through lower quality rock.

As dolomite proportion increases, the range of possible breakthrough times and PVI increases, indicating an increasing sensitivity to the facies model. At very high

dolomite proportions (>75%) the maximum PVI is 50% higher than the minimum PVI. This is related to the relative distribution of dolomite bodies. Within a clinothem, dolomite bodies were assumed to be distributed close to uniform along depositional strike direction. But no relationship is assumed between location of dolomite bodies in neighboring clinothems. When dolomite bodies are roughly aligned from one clinothem to the next (**Fig. 4-15 b, d**), flow paths are preserved through limestone facies leading (directly) from inlet to outlet, and breakthrough is early, and less volume has been swept (low PVI). When dolomite geobody positions are in alternating positions for successive clinothems (similar to a chessboard pattern) very few connected flow paths remain (**Fig. 4-17 a, b, c**), and breakthrough is delayed thus leading to a larger volume of oil swept. As more dolomite bodies are present the chance of continuous flow paths from inlet to outlet is reduced and most models tend towards completely discontinuous flow paths. This is also reflected in **Figure 4-14**, showing an increase in PVI with later breakthrough times. Another difference is the spacing between different clinoforms (**Fig. 4-15 b, d**). For the same number of dolomite bodies, the flow paths remaining between them are longer if clinoform spacing increases (to approximately equidistant clinoform spacing), and thus reducing the number of times flow paths are diverted or interrupted.

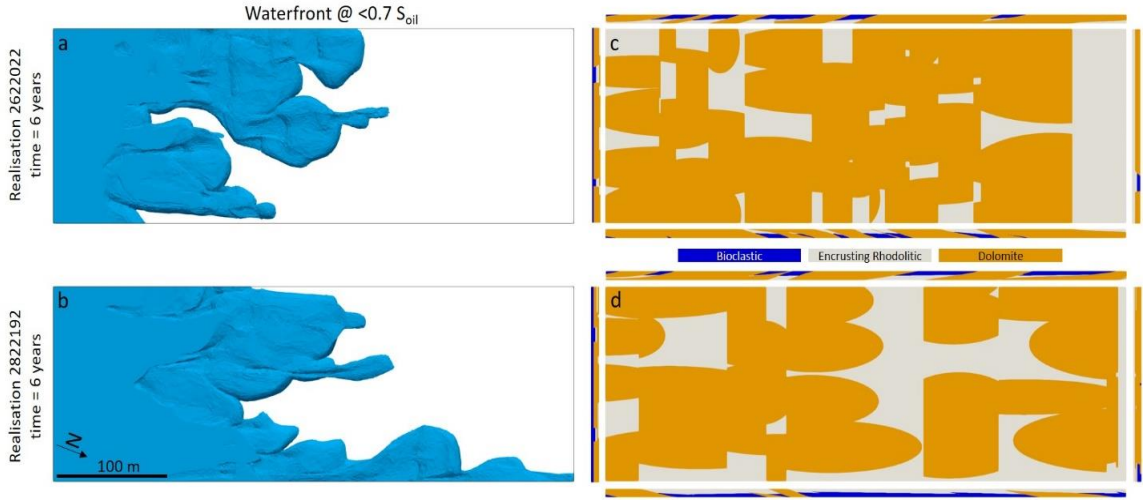

Figure 4-17: Comparison of waterfront after 6 years of production in realization 2622022 and 2822192 (Figure 4-14 d) of Scenario 1 with four dolomite bodies per clinothem. a) Waterfront is split up into multiple fingers that have reached roughly halfway across the model, while in (b) breakthrough has already occurred. c) Map and side views of model. Distribution of dolomite bodies is dense as a result of short spacing between clinoforms, and flow paths in limestone are very short and interrupted. d) Map and side views of model. Spacing of clinoforms is large, resulting in longer flow paths within one clinothem. Position of dolomite bodies are roughly aligned, resulting in a long continuous flow path, particularly along the bottom edge of the model.

4.5.2.2. Scenario 2: Dolomitization increasing flow properties

Scenario 2 reflects an alternative to the outcrop measurements, in which dolomite bodies are on average 5% more porous and 10x more permeable than the precursor limestone. This increase in petrophysical properties causes an expected increase in flow rates and earlier water breakthrough (**Fig. 4-15 a, c**). In contrast to undolomitized clinoforms, the production curves indicate a model-wide continuous waterfront, preferentially sweeping the bottom bioclastic facies until breakthrough (**Fig. 4-16 a, b),** followed by sweeping the upper encrusting rhodolitic facies until a second break is

observed in production curves (**Fig. 4-15 a, b**). When dolomite bodies are introduced, even at low proportions, this behavior changes as dolomite bodies span both upper encrusting/rhodolitic and lower bioclastic facies. This allows some of the upper parts of the models to be swept where they are dolomitized (**Fig. 4-16**). The waterfront is focused along dolomite bodies, forming protruding fingers instead of a more piston-like displacement. At low dolomite proportions (20-40%), this behavior results in a smoother break in production curves at breakthrough and multiple steps rather than a sharp decline in oil production rate. With increasing dolomite proportions, a more continuous waterfront forms and results in the production profile showing a sharp break again above ~80% dolomite as the models become more homogeneous.

Sweep efficiency increases with increasing dolomite proportion (**Fig. 4-15 d**) with higher pore volumes of oil produced per pore volume water injected. At low dolomite proportions (<30%) after around 1.3PVI, recovery drops below that of undolomitized limestone. This is likely caused by preferential flow paths along permeable dolomite geobodies which focus fluid flow and slow down sweeping of the upper encrusting/rhodolitic facies. As flow paths get wider and better connected with increasing dolomite proportions, more of the relatively low-quality limestone is connected to more permeable dolomite and thus swept.

At low dolomite proportions (20-40%), the range of possible breakthrough times and PVI at breakthrough is relatively large (**Fig. 4-16 b**), further indicating a large sensitivity to the facies model similar to what was found in Scenario 1. This is likely caused by the alignment of dolomite geobodies between successive clinoforms or the

lack thereof (**Fig. 4-18**). When dolomite geobodies are not aligned between the model inlet and outlet, flow is diverted between isolated bodies of high permeability dolomite. Whereas if dolomite bodies are aligned, a direct path forms between the model inlet and outlet. In addition to dolomite body alignment, clinoform spacing also plays a role in breakthrough time and PVI. As dolomitization is bound within individual clinothems (Laya et al, 2018), wider clinoform spacing also allows longer dolomite geobodies to form and thus form longer uninterrupted flow paths (e.g. **Fig. 4-18 d**). In short, the combination of dolomite geobody alignment and clinoform spacing determine the breakthrough time and PVI at low dolomite proportions. With increasing dolomite proportions, sensitivity of both breakthrough time and PVI to the geological model diminishes as connectivity between dolomite bodies increases and thus the role of clinoform spacing decreases.

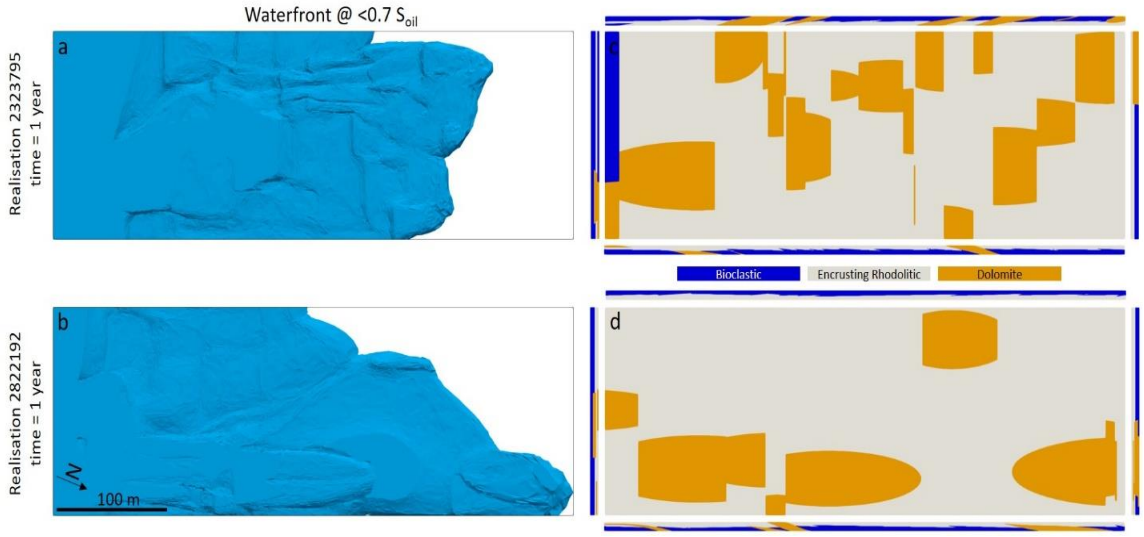

Figure 4-18: Comparison of waterfront in plain view, after 1 year of production in Scenario 2 (dolomite more permeable than limestone) for realization 2323795 and 2822192 with 1 dolomite body per clinothem (Figure 16 d). a) Waterfront progresses along the whole model width with minimal protrusions. b) Waterfront favors one side of the model and is approximately 100m ahead of the waterfront above. c) Map and side views of model. Distribution of dolomite bodies is not aligned from input face to output. Some connectivity is present between dolomite bodies. Dolomite body length (directly dependent on clinoform spacing) is relatively short. d) Map and side views of model. The number of visible dolomite bodies is limited to 9. The dolomite bodies are aligned and long (wide clinoform spacing), resulting in a longer continuous flow path.

4.5.3. Controls on dolomite geobody geometries

These flow models demonstrate that breakthrough times are not merely a function of the volume of dolomite but are strongly affected by the orientation and connectivity of dolomite geobodies as well. Thus, a good understanding of the origin of the dolomite geobodies is vital to reducing the uncertainty in flow behavior in dolomitized systems. The geometry (and by extension, connectivity) of the dolomite

geobodies are strongly controlled by the hydrodynamic driver of the dolomitizing fluids (Whitaker et al. 2004) and the distribution of textures (and thus, porosity and permeability)(Al-Helal et al. 2012) within the precursor limestones. For example, dolomitization by geothermal processes as previously described will lead to larger dolomite bodies with correspondingly larger zones of enhanced or decreased porosity and permeability (Whitaker and Xiao, 2010). Similarly, formations with greater abundances of micritic mud relative to larger grain fractions will likely also have higher abundances of dolomite (Murray and Lucia 1967; Al-Helal et al. 2012)

In the case of Seru Grandi, clinoform spacing shows a gamma distribution with a shape parameter of ~1, which is approximated by an exponential distribution.;. Exponential spacing distribution can be interpreted deposition by a stochastic Poisson process, in which the thickness between successive events, in this case formation of clinoform surfaces, occur independently of each other, rather than by hierarchical and periodic processes of deposition (e.g. sea-level changes) (Drummond and Wilkinson, 1996). The dolomite geobodies in Seru Grandi are consistently bounded by clinoform surfaces, with minimal cross-cutting of dolomite geobodies across clinoforms, and (maximum) dolomite body size ultimately controlled by the same process. Similarly, the size of dolomite geobodies within the Seru Grandi clinoforms would be exponential as well. As also observed for clinoform spacing, this would suggest that dolomitization in the Seru Grandi occurred by events independent of clinothem deposition following the suggestion of Laya et al. (2021). This finding is key to understanding the impact of fluid flow as a function of dolomite geobody abundance, as it demonstrates a clear link

between the distribution of the dolomite geobodies with the overall carbonate clinoform architecture.

Gabellone et al. (2016) suggest that varying the distribution of permeable beds, the configuration of brine pools, and the sequence of dolomitization can result in widely different configurations of dolomite geobodies. Therefore, whether dolomite geobodies tend to align and form long continuous flow paths (or baffles) or cluster and form isolated pods of enhanced or reduced permeability is heavily dependent on how the carbonate bodies are deposited at the onset of dolomitization and subsequently by the dolomitizing model.

In the case of carbonate clinoforms, the workflow and findings from this study would be particularly applicable to both prospective and producing carbonate basins such as the Upper Cretaceous and Tertiary carbonates of the Northern Carnarvon Basin in Australia (Hocking, 1998). Specifically, by integrating data from on the geological history, rock properties of both the dolomite and limestone rocks, dolomitization model, and strata geometries, one can best capture the flow behavior of the reservoir and thus optimize production.

4.6. Conclusions

Geological models of partially dolomitized clinoforms were constructed based on the detailed characterization of the Miocene Seru Grandi outcrop in Bonaire using conventional diagenetic analysis, conventional field studies, digital outcrop model measurements. The effect of dolomitization on flow behavior of clinoforms is studied, at

a grid cell to inter-well scale, for two scenarios: (1) Dolomitization reduces flow properties as observed in outcrop and (2) dolomitization improves flow properties (alternative subsurface scenario). Both scenarios indicate an exponential relationship between breakthrough times and flow rates versus dolomite proportions. However, regardless of dolomite proportions, a low number of well-aligned dolomite bodies can produce similar behavior than many poorly aligned dolomite bodies. The sensitivity of the flow behavior to the geological models is different for both scenarios. If dolomitization decreases flow properties, sensitivity of breakthrough time and PVI increases with dolomite proportion. If dolomitization causes an increase in flow properties, sensitivity decreases with dolomite proportion. For both scenarios, the contrast between limestone and dolomite permeability forms flow barriers or conduits, but the flow behavior is controlled by the spatial organization of dolomite geobodies. This is important for uncertainty analysis of subsurface models, as the sensitivity to the geological model varies depending on effect dolomitization has on petrophysical properties relative to the precursor limestone.

The results from this study have direct applications for improving quantification and characterization of carbonate succession with complex geometries across multiple orders of magnitudes of scales which collectively allow for 1) better representation of carbonate geometries in geological models, 2) better predictions of flow behavior, and 3) better predictions of flow connectivity in these systems.

5. CONCLUSIONS

The objective of this dissertation was to employ high temperature dolomite synthesis experiments in laboratory, petrographical and geochemical studies on samples obtained from Bonaire, and digital outcrop models paired with an unstructured mesh flow simulator to investigate the relationship between biogenic HMC with dolomitization, and the effect of dolomitization on fluid flow behavior in carbonate clinoforms.

In Chapter 2, we used high temperature dolomite synthesis experiments to determine the effect magnesium concentrations in HMC bioclasts has on dolomitization rate, dolomite stoichiometry, and dolomite textures. We observe that the Mg concentration in biogenic HMC does not correlate with rate of dolomitization, induction period, or the stoichiometry of dolomite products except in specific cases such as *Goniolithon*. These edge cases may be a result of their exceptional effectiveness at liberating Mg ions into solution relative to similar bioclasts. Additionally, skeletal HMC grains consistently retain their original microstructure upon dolomitization because of the very fine mimetic dolomite that is precipitated within their microstructures. Collectively, our data suggests that reactant microstructure appears to influence reaction rates to a greater degree than the reactant Mg concentration. Our observations are generally in line with previous studies and illustrate a set of diagenetic pathways that can occur to result in selective dolomitization of HMC bioclasts. The results also imply that the observed correlation between coralline red algae abundance and global

dolomitization events in the Neogene is not caused by reactant magnesium concentration, but more likely reflects changes in species abundance and microstructure.

In Chapter 3, we use petrographic and geochemical analyses on partially dolomitized samples obtained from the Seru Grandi terraces in Bonaire to assess the degree and sequence of preferential dolomitization of various carbonate components. We observe that selective dolomitization does occur within the partially dolomitized samples in Bonaire. The micrite matrix is most likely to be dolomitized first, followed by coralline red algae, and subsequently all other allochems are likely to be among the last to be dolomitized. Coralline red algae also show evidence of having been stabilized to LMC prior to dolomitization based on observations of $\delta^{18}O$ and $\delta^{13}C$ stable isotope geochemistry values between the bulk rock and coralline red algae clasts. This ties in with the observation that coralline red algae appear to be able to initiate and sustain local dolomitization via an internal sourcing of Mg ions during stabilization from HMC to LMC. Distinct variations in pore-filling cement habit and composition can also be observed between updip and downdip sediments within individual clinoforms. Collectively, this study demonstrates that the diagenetic history for the Seru Grandi clinoforms is much more complex than previously known.

In Chapter 4, we characterized the geometries within the partially dolomitized Seru Grandi clinoforms using a digital outcrop model and constructed multiple iterations of geological models containing varying amounts of dolomite geobodies to study the effect of dolomitization on flow behavior in carbonate clinoforms. Two scenarios are tested within grid to inter-well scales, one where dolomitization reduces the flow

properties relative to the precursor limestone, and another where dolomitization increases flow properties relative to the precursor limestone. In either scenario tested, we observe an exponential relationship between breakthrough times and flow rates with respect to the amount of dolomite geobodies in the model. Independent of dolomite proportions, a low number of well-aligned dolomite bodies can produce similar behavior than many poorly aligned dolomite bodies. The sensitivity of the flow behavior to the geological models varies as a function of the dolomite's permeability relative to the precursor limestone. When dolomite geobodies have a lower permeability than the precursor limestone, sensitivity of breakthrough time and PVI increases with dolomite abundance. When dolomite geobodies have a higher permeability than the precursor limestone, sensitivity of breakthrough time and PVI decreases with dolomite abundance. The results from this study have direct applications for improving quantification and characterization of carbonate succession with complex geometries across multiple orders of magnitudes of scales

Overall, this dissertation demonstrates that dolomitization can be linked to the occurrence of HMC; however, the link relies less on the actual mineralogy of the HMC component, but rather the reactive surface area of the HMC component. Additionally, this dissertation also demonstrates that fluid flow behavior in carbonate reservoirs does not simply depend on the abundance or rock properties of dolomite geobodies, but their configuration in the reservoir as well.

REFERENCES

ADAMS, E.W., GRÉLAUD, C., PAL, M., CSOMA, A.É., AL JA'AIDI, O.S., AND AL HINAI, R., 2011, Improving reservoir models of Cretaceous carbonates with digital outcrop modelling (Jabal Madmar, Oman): static modelling and simulating clinoforms: Petroleum Geoscience, v. 17, p. 309-332.

ADAMS, J.E., AND RHODES, M.L., 1960, Dolomitization by Seepage Refluxion1: AAPG Bulletin, v. 44, p. 1912-1920.

ADEY, W.H., AND MACINTYRE, I., 1973, Crustose coralline algae: a re-evaluation in the geological sciences: Geological Society of America Bulletin, v. 84, p. 883-904.

AGUIRRE, J., RIDING, R., AND BRAGA, J.C., 2000, Diversity of coralline red algae: origination and extinction patterns from the Early Cretaceous to the Pleistocene: Paleobiology, v. 26, p. 651-667.

AL-HELAL, A.B., WHITAKER, F.F., AND XIAO, Y., 2012, Reactive transport modeling of brine reflux: dolomitization, anhydrite precipitation, and porosity evolution: Journal of Sedimentary Research, v. 82, p. 196-215.

ALEXANDER, C.S., 1961, The marine terraces of Aruba, Bonaire, and Curaçao, Netherlands Antilles: Annals of the Association of American Geographers, v. 51, p. 102-123.

ANSELMETTI, F.S., EBERLI, G.P., AND DING, Z.-D., 2000, From the Great Bahama Bank into the Straits of Florida: A margin architecture controlled by sea-level fluctuations and ocean currents: GSA Bulletin, v. 112, p. 829-844.

ARVIDSON, R.S., AND MACKENZIE, F.T., 1999, The dolomite problem; control of precipitation kinetics by temperature and saturation state: American Journal of Science, v. 299, p. 257-288.

AUER, G., AND PILLER, W.E., 2020, Nanocrystals as phenotypic expression of genotypes—An example in coralline red algae: Science advances, v. 6, p. eaay2126.

BAKER, P., 1986, Pore-water chemistry of carbonate-rich sediments, Lord Howe Rise, southwest Pacific-Ocean: Initial reports of the deep sea drilling project, v. 90, p. 1249-1256.

BAKER, P.A., AND BLOOMER, S.H., 1988, The origin of celestite in deep-sea carbonate sediments: Geochimica et Cosmochimica Acta, v. 52, p. 335-339.

BAKER, P.A., AND KASTNER, M., 1981, Constraints on the formation of sedimentary dolomite: Science, v. 213, p. 214-216.

BANDOIAN, C.A., AND MURRAY, R.C., 1974, Pliocene-pleistocene carbonate rocks of Bonaire, Netherlands Antilles: Geological Society of America Bulletin, v. 85, p. 1243-1252.

BANNER, J.L., 1995, Application of the trace element and isotope geochemistry of strontium to studies of carbonate diagenesis: Sedimentology, v. 42, p. 805-824.

BASHARI, A., 2005, Khuff formation Permian-Triassic carbonate in the Qatar-South Fars arch hydrocarbon province of the Persian Gulf: First Break, v. 23.

BETZLER, C., LÜDMANN, T., HÜBSCHER, C., AND FÜRSTENAU, J., 2013, Current and sea-level signals in periplatform ooze (Neogene, Maldives, Indian Ocean): Sedimentary Geology, v. 290, p. 126-137.

BLATT, H., MIDDLETON, G., AND MURRAY, R.C., 1980, Origin of sedimentary rocks, Prentice Halline Englewood Cliffs, New Jersey, p. 782.

BRAGA, J.C., AND AGUIRRE, J., 1995, Taxonomy of fossil coralline algal species: Neogene Lithophylloideae (Rhodophyta, Corallinaceae) from southern Spain: Review of Palaeobotany and Palynology, v. 86, p. 265-285.

BRAGA, J.C., AND AGUIRRE, J., 2001, Coralline algal assemblages in upper Neogene reef and temperate carbonates in Southern Spain: Palaeogeography, Palaeoclimatology, Palaeoecology, v. 175, p. 27-41.

BUCHBINDER, B., AND FRIEDMAN, G.M., 1970, Selective dolomitization of micritic envelopes; a possible clue to original mineralogy: Journal of Sedimentary Research, v. 40, p. 514-517.

BUCHBINDER, L.G., 1979, Facies, Environment of Deposition and Correlation of the Zohar (Brur Calcarenite) Karmon, and Shderot Formations in the Ashdod Area, Geological Survey of Israel.

BUDD, D., 1997a, Cenozoic dolomites of carbonate islands: their attributes and origin: Earth-Science Reviews, v. 42, p. 1-47.

BUDD, D.A., 1997b, Cenozoic dolomites of carbonate islands: their attributes and origin: Earth-Science Reviews, v. 42, p. 1-47.

BUDD, D.A., AND MATHIAS, W.D., 2015, Formation of Lateral Patterns In Rock Properties By Dolomitization: Evidence From A Miocene Reaction Front (Bonaire, Netherlands Antilles): Journal of Sedimentary Research, v. 85, p. 1082-1101.

BUDD, D.A., AND PARK, A.J., 2018, Formation of bed-scale spatial patterns in dolomite abundance during early dolomitization: Part I. Mechanisms and feedbacks revealed by reaction–transport modelling: Sedimentology, v. 65, p. 209-234.

BUDD, D.A., AND PARK, A.J., 2019, Bed-scale spatial patterns in dolomite abundance: Part II. Effect of varied fluid chemistry, flow rate, precursor mineralogy, temperature, textural heterogeneity, nucleation density and bed geometry: Sedimentology, v. 66, p. 2721-2748.

BULLEN, S.B., AND SIBLEY, D.F., 1984, Dolomite selectivity and mimic replacement: Geology, v. 12, p. 655-658.

BUSTER, N.A., AND HOLMES, C.W., 2006, Magnesium content within the skeletal architecture of the coral Montastraea faveolata: locations of brucite precipitation and implications to fine-scale data fluctuations: Coral Reefs, v. 25, p. 243-253.

CANTRELL, D., SWART, P., AND HAGERTY, R., 2004, Genesis and characterization of dolomite, Arab-D reservoir, Ghawar field, Saudi Arabia: GeoArabia, v. 9, p. 11-36.

CHAPPARD, D., DEGASNE, I., HURE, G., LEGRAND, E., AUDRAN, M., AND BASLE, M., 2003, Image analysis measurements of roughness by texture and fractal analysis correlate with contact profilometry: Biomaterials, v. 24, p. 1399-1407.

CHAVE, K.E., 1952, A solid solution between calcite and dolomite: The Journal of Geology, v. 60, p. 190-192.

CHAVE, K.E., 1954, Aspects of the biogeochemistry of magnesium 1. Calcareous marine organisms: The Journal of Geology, v. 62, p. 266-283.

CHAVE, K.E., AND SCHMALZ, R.F., 1966, Carbonate-seawater interactions: Geochimica et Cosmochimica Acta, v. 30, p. 1037-1048.

CHOQUETTE, P.W., AND PRAY, L.C., 1970, Geologic nomenclature and classification of porosity in sedimentary carbonates: AAPG bulletin, v. 54, p. 207-250.

COHEN, H., AND KACZMAREK, S., 2017, Evaluating the effects of fluid NaCl and KCl concentrations on reaction rate, major cation composition, and cation ordering during high-temperature dolomitization experiments: Geological Society of America Abstracts with Programs, p. 182-46.

CONSTANTZ, B.R., 1986, The primary surface area of corals and variations in their susceptibility to diagenesis, Reef diagenesis, Springer, p. 53-76.

DAVIS, R., FONTANILLA, J., BISWAS, P., AND SAHA, S., 1997, Lithology, lithofacies, and permeability estimation in Ghawar Arab-D reservoir: Middle East Oil Show and Conference.

DEFFEYES, K., LUCIA, F.J., AND WEYL, P., 1965a, Dolomitizanon of Recent and Plio-Pleistocene Sediments by Marine Evaporite Waters on Bonaire Netherlands Antilles.

DEFFEYES, K., LUCIA, F.J., AND WEYL, P., 1965b, Dolomitizanon of Recent and Plio-Pleistocene Sediments by Marine Evaporite Waters on Bonaire Netherlands

Antilles: SEPM Special Publication, v. Dolomitization and Limestone Diagenesis (SP13), p. 71 - 88.

DIAZ-PULIDO, G., NASH, M.C., ANTHONY, K.R., BENDER, D., OPDYKE, B.N., REYES-NIVIA, C., AND TROITZSCH, U., 2014, Greenhouse conditions induce mineralogical changes and dolomite accumulation in coralline algae on tropical reefs: Nature communications, v. 5, p. 1-9.

DIX, G.R., 1997, Stratigraphic patterns of deep-water dolomite, Northeast Australia: Journal of Sedimentary Research, v. 67, p. 1083-1096.

DUNHAM, R.J., 1962, Classification of carbonate rocks according to depositional textures.

EHRENBERG, S.N., EBERLI, G.P., AND BAECHLE, G., 2006, Porosity–permeability relationships in Miocene carbonate platforms and slopes seaward of the Great Barrier Reef, Australia (ODP Leg 194, Marion Plateau): Sedimentology, v. 53, p. 1289-1318.

EMBRY, A.F., AND KLOVAN, J.E., 1971, A late Devonian reef tract on northeastern Banks Island, NWT: Bulletin of Canadian petroleum geology, v. 19, p. 730-781.

ENGEL, M., BRÜCKNER, H., FÜRSTENBERG, S., FRENZEL, P., KONOPCZAK, A.M., SCHEFFERS, A., KELLETAT, D., MAY, S.M., SCHÄBITZ, F., AND DAUT, G., 2013, A prehistoric tsunami induced long-lasting ecosystem changes on a semi-arid tropical island—the case of Boka Bartol (Bonaire, Leeward Antilles): Naturwissenschaften, v. 100, p. 51-67.

FALINI, G., ALBECK, S., WEINER, S., AND ADDADI, L., 1996, Control of aragonite or calcite polymorphism by mollusk shell macromolecules: Science, v. 271, p. 67-69.

FELIS, T., GIRY, C., SCHOLZ, D., LOHMANN, G., PFEIFFER, M., PÄTZOLD, J., KÖLLING, M., AND SCHEFFERS, S.R., 2015, Tropical Atlantic temperature seasonality at the end of the last interglacial: Nature communications, v. 6, p. 6159.

FLÜGEL, E., 2004, Microfacies of carbonate rocks: analysis, interpretation and application, Springer Science & Business Media.

GABELLONE, T., WHITAKER, F., KATZ, D., GRIFFITHS, G., AND SONNENFELD, M., 2016, Controls on reflux dolomitisation of epeiric-scale ramps: Insights from reactive transport simulations of the Mississippian Madison Formation (Montana and Wyoming): Sedimentary Geology, v. 345, p. 85-102.

GAINES, A.M., 1977, Protodolomite redefined: Journal of Sedimentary Research, v. 47, p. 543-546.

GAINES, A.M., 1980, Dolomitization kinetics: recent experimental studies: SEPM Special Publication, p. 81 - 86.

GEORGE, C., AND STILES, L., 1978, Improved techniques for evaluating carbonate waterfloods in West Texas: Journal of Petroleum Technology, v. 30, p. 1,547-1,554.

GHOSH, V., 2013, Matrix Acidizing Parallel Core Flooding Apparatus [unpublished Master's thesis thesis]: Texas A&M University.

GLOVER, E., AND SIPPEL, R., 1967, Synthesis of magnesium calcites: Geochimica et Cosmochimica Acta, v. 31, p. 603-613.

GOLDSMITH, J.R., AND GRAF, D.L., 1958, Structural and compositional variations in some natural dolomites: The Journal of Geology, v. 66, p. 678-693.

GOODELL, H., AND GARMAN, R., 1969, Carbonate geochemistry of Superior deep test well, Andros Island, Bahamas: AAPG Bulletin, v. 53, p. 513-536.

GROSSMAN, E., 2012, Chapter 10: oxygen isotope stratigraphy: The Geologic Time Scale: Boston, Elsevier, p. 181-206.

GUIRY, M.D., AND GUIRY, G.M., 2021, Goniolithon Foslie, 1898: http://www.algaebase.org, National University of Ireland, Galway.

HALFAR, J., AND MUTTI, M., 2005, Global dominance of coralline red-algal facies: a response to Miocene oceanographic events: Geology, v. 33, p. 481-484.

HALLEY, R.B., AND SCHMOKER, J.W., 1983, High-Porosity Cenozoic Carbonate Rocks of South Florida: Progressive Loss of Porosity with Depth1: AAPG Bulletin, v. 67, p. 191-200.

HANDFORD, C., AND BARIA, L., 2007, Geometry and seismic geomorphology of carbonate shoreface clinoforms, Jurassic Smackover Formation, north Louisiana: Geological Society, London, Special Publications, v. 277, p. 171-185.

HASHIM, M.S., AND KACZMAREK, S.E., 2020, Experimental stabilization of carbonate sediments to calcite: Insights into the depositional and diagenetic controls on calcite microcrystal texture: Earth and Planetary Science Letters, v. 538, p. 116235.

HENRIKSEN, S., HELLAND-HANSEN, W., AND BULLIMORE, S., 2011, Relationships between shelf-edge trajectories and sediment dispersal along depositional dip and strike: a different approach to sequence stratigraphy: Basin Research, v. 23, p. 3-21.

HIPPOLYTE, J.-C., AND MANN, P., 2011, Neogene–Quaternary tectonic evolution of the Leeward Antilles islands (Aruba, Bonaire, Curaçao) from fault kinematic analysis: Marine and Petroleum Geology, v. 28, p. 259-277.

JACKSON, M., HAMPSON, G., SAUNDERS, J., EL-SHEIKH, A., GRAHAM, G., AND MASSART, B., 2014, Surface-based reservoir modelling for flow simulation: Geological Society, London, Special Publications, v. 387, p. 271-292.

JACKSON, M., PERCIVAL, J., MOSTAGHIMI, P., TOLLIT, B., PAVLIDIS, D., PAIN, C., GOMES, J., ELSHEIKH, A.H., SALINAS, P., AND MUGGERIDGE, A., 2015, Reservoir modeling for flow simulation by use of surfaces, adaptive unstructured meshes, and an overlapping-control-volume finite-element method: SPE Reservoir Evaluation & Engineering, v. 18, p. 115-132.

JACKSON, M.D., HAMPSON, G.J., AND SECH, R.P., 2009, Three-dimensional modeling of a shoreface-shelf parasequence reservoir analog: Part 2. Geologic controls on fluid flow and hydrocarbon recovery: AAPG bulletin, v. 93, p. 1183-1208.

JACQUEMYN, C., JACKSON, M.D., AND HAMPSON, G.J., 2019, Surface-based geological reservoir modelling using grid-free NURBS curves and surfaces: Mathematical Geosciences, v. 51, p. 1-28.

JAMES, N.P., AND JONES, B., 2015, Origin of carbonate sedimentary rocks, John Wiley & Sons.

JENNINGS JR, J., AND WARD, W., 2000, Geostatistical analysis of permeability data and modeling of fluid-flow effects in carbonate outcrops: SPE Reservoir Evaluation & Engineering, v. 3, p. 292-303.

JONES, G.D., AND XIAO, Y., 2005, Dolomitization, anhydrite cementation, and porosity evolution in a reflux system: Insights from reactive transport models: AAPG bulletin, v. 89, p. 577-601.

KACZMAREK, S.E., GREGG, J.M., BISH, D.L., MACHEL, H.G., FOUKE, B.W., MACNEIL, A., LONNEE, J., AND WOOD, R., 2017, Dolomite, very-high magnesium calcite, and microbes: implications for the microbial model of dolomitization: SEPM Special Publication, v. 109, p. 1-14.

KACZMAREK, S.E., AND SIBLEY, D.F., 2007, A comparison of nanometer-scale growth and dissolution features on natural and synthetic dolomite crystals: implications for the origin of dolomite: Journal of Sedimentary Research, v. 77, p. 424-432.

KACZMAREK, S.E., AND SIBLEY, D.F., 2011, On the evolution of dolomite stoichiometry and cation order during high-temperature synthesis experiments: an alternative model for the geochemical evolution of natural dolomites: Sedimentary Geology, v. 240, p. 30-40.

KACZMAREK, S.E., AND SIBLEY, D.F., 2014, Direct physical evidence of dolomite recrystallization: Sedimentology, v. 61, p. 1862-1882.

KACZMAREK, S.E., AND THORNTON, B.P., 2017, The effect of temperature on stoichiometry, cation ordering, and reaction rate in high-temperature dolomitization experiments: Chemical Geology, v. 468, p. 32-41.

KENWARD, P.A., FOWLE, D.A., GOLDSTEIN, R.H., UESHIMA, M., GONZÁLEZ, L.A., AND ROBERTS, J.A., 2013, Ordered low-temperature dolomite mediated by carboxyl-group density of microbial cell walls: AAPG bulletin, v. 97, p. 2113-2125.

KOCURKO, M.J., 1979, Dolomitization by spray-zone brine seepage, San Andres, Colombia: Journal of Sedimentary Research, v. 49, p. 209-213.

KRAMER, P.A., SWART, P.K., DE CARLO, E.H., AND SCHOVSBO, N.H., 2000, Overview of interstitial fluid and sediment geochemistry, sites 1003-1007 (Bahamas transect): Proceedings pf ODP, science results, v. 166, p. 179-195.

LAND, L., 1992, The dolomite problem: stable and radiogenic isotope clues: Isotopic signatures and sedimentary records, p. 49-68.

LAND, L.S., 1967, Diagenesis of skeletal carbonates: Journal of Sedimentary Research, v. 37, p. 914-930.

LAND, L.S., 1985, The origin of massive dolomite: Journal of Geological Education, v. 33, p. 112-125.

LAND, L.S., 1998, Failure to Precipitate Dolomite at 25° C fromDilute Solution Despite 1000-Fold Oversaturation after32 Years: Aquatic Geochemistry, v. 4, p. 361-368.

LAND, L.S., AND EPSTEIN, S., 1970, LATE PLEISTOCENE DIAGENESIS AND DOLOMITIZATION, NORTH JAMAICA 1: Sedimentology, v. 14, p. 187-200.

LAYA, J.C., SULAICA, J., TEOH, C.P., WHITAKER, F., GABELLONE, T., TUCKER, M.E., TESCH, P., MILLER, B., PRINCE, K., AND IZAGUIRRE, I., 2018a, Controls on Neogene carbonate facies and stratigraphic architecture of an isolated carbonate platform–the Caribbean island of Bonaire: Marine and Petroleum Geology, v. 94, p. 1-18.

LAYA, J.C., SULAICA, J., TEOH, C.P., WHITAKER, F., GABELLONE, T., TUCKER, M.E., TESCH, P., MILLER, B., PRINCE, K., AND IZAGUIRRE, I., 2018b, Controls on Neogene carbonate facies and stratigraphic architecture of an isolated carbonate platform – the Caribbean island of Bonaire: Marine and Petroleum Geology, v. 94, p. 1-18.

LAYA, J.C., TEOH, C.P., PRINCE, K., AND WIDODO, R., 2018c, Dolomitization of Neogene Carbonate Platforms: Controversies on Synchronous Events and Bioclast Influence: International Sedimentological Congress.

LAYA, J.C., TEOH, C.P., WHITAKER, F., MANCHE, C., KACZMAREK, S., TUCKER, M., GABELLONE, T., AND HASIUK, F., 2021, Dolomitization of a Miocene-Pliocene progradational carbonate platform by mesohaline brines: Re-examination of the reflux model on Bonaire Island: Marine and Petroleum Geology, v. 126, p. 104895.

LU, F.H., AND MEYERS, W.J., 1998, Massive dolomitization of a late Miocene carbonate platform: a case of mixed evaporative brines with meteoric water, Nijar, Spain: Sedimentology, v. 45, p. 263-277.

LUCIA, F., AND MAJOR, R., 1994a, Porosity evolution through hypersaline reflux dolomitization: Dolomites: A Volume in Honour of Dolomieu, p. 325-341.

LUCIA, F.J., AND MAJOR, R.P., 1994b, Porosity evolution through hypersaline reflux dolomitization, *in* Purser, B., Tucker, M.E., and Zenger, D., eds., Dolomites: A Volume in Honour of Dolomieu, p. 325-341.

LUMSDEN, D.N., 1979, Discrepancy between thin-section and X-ray estimates of dolomite in limestone: Journal of Sedimentary Research, v. 49, p. 429-435.

MACHEL, H.G., 2004, Concepts and models of dolomitization: a critical reappraisal: Geological Society, London, Special Publications, v. 235, p. 7-63.

MANCHE, C.J., AND KACZMAREK, S.E., 2019, Evaluating reflux dolomitization using a novel high-resolution record of dolomite stoichiometry: A case study from the Cretaceous of central Texas, USA: Geology, v. 47, p. 586-590.

MANN, S., 2009, Handbook of Biomineralization: Biomimetic and bioinspired chemistry, v. 2, John Wiley & Sons.

MANSOUR, A.S., AND ABD-ELLATIF, M.T., 2013, Dolomitization of the Miocene carbonates in Gebel Abu Shaar El Qiblie and Salum area, Egypt: a petrographical and geochemical comparative study: Carbonates and Evaporites, v. 28, p. 347-363.

MATTHEW, A.J., WOODS, A.J., AND OLIVER, C., 1991, Spots before the eyes: new comparison charts for visual percentage estimation in archaeological material: Recent developments in ceramic petrology, v. 81, p. 211-263.

MATTHEWS, A., AND KATZ, A., 1977, Oxygen isotope fractionation during the dolomitization of calcium carbonate: Geochimica et Cosmochimica Acta, v. 41, p. 1431-1438.

MELIM, L., WESTPHAL, H., SWART, P., EBERLI, G., AND MUNNECKE, A., 2002, Questioning carbonate diagenetic paradigms: evidence from the Neogene of the Bahamas: Marine Geology, v. 185, p. 27-53.

MILLIMAN, J.D., GASTNER, M., AND MÜLLER, J., 1971, Utilization of magnesium in coralline algae: Geological Society of America Bulletin, v. 82, p. 573-580.

MOBERLY, R., 1970, Microprobe study of diagenesis in calcareous algae: Sedimentology, v. 14, p. 113-123.

MORROW, D., 1982, Diagenesis 2. Dolomite-part 2 dolomitization models and ancient dolostones: Geoscience Canada, v. 9.

MORSE, J.W., ARVIDSON, R.S., AND LÜTTGE, A., 2007, Calcium carbonate formation and dissolution: Chemical reviews, v. 107, p. 342-381.

MORSE, J.W., AND MACKENZIE, F.T., 1990, Geochemistry of sedimentary carbonates, Elsevier.

MURRAY, R., AND LUCIA, F., 1967, Cause and control of dolomite distribution by rock selectivity: Geological Society of America Bulletin, v. 78, p. 21-36.

MURRAY, R.C., 1960, Origin of porosity in carbonate rocks: Journal of Sedimentary Research, v. 30, p. 59-84.

NASH, M., TROITZSCH, U., OPDYKE, B., TRAFFORD, J., RUSSELL, B., AND KLINE, D., 2011, First discovery of dolomite and magnesite in living coralline algae and its geobiological implications.

NASH, M., UTHICKE, S., NEGRI, A., AND CANTIN, N., 2015, Ocean acidification does not affect magnesium composition or dolomite formation in living crustose coralline algae, Porolithon onkodes in an experimental system: Biogeosciences Discussions, v. 12.

NASH, M.C., DIAZ-PULIDO, G., HARVEY, A.S., AND ADEY, W., 2019, Coralline algal calcification: A morphological and process-based understanding: PloS one, v. 14, p. e0221396.

NASH, M.C., OPDYKE, B.N., TROITZSCH, U., RUSSELL, B.D., ADEY, W.H., KATO, A., DIAZ-PULIDO, G., BRENT, C., GARDNER, M., AND PRICHARD, J., 2013, Dolomite-rich coralline algae in reefs resist dissolution in acidified conditions: Nature climate change, v. 3, p. 268-272.

OHDE, S., AND KITANO, Y., 1981, Protodolomite in Daito jima, Okinawa: Geochemical Journal, v. 15, p. 199-207.

OSMAN, H., GRAHAM, G.H., MONCORGE, A., JACQUEMYN, C., AND JACKSON, M.D., 2020, Is Cell-to-Cell Scale Variability Necessary in Reservoir Models?: Mathematical Geosciences, p. 1-26.

PATON, C., HELLSTROM, J., PAUL, B., WOODHEAD, J., AND HERGT, J., 2011, Iolite: Freeware for the visualisation and processing of mass spectrometric data: Journal of Analytical Atomic Spectrometry, v. 26, p. 2508-2518.

PATRUNO, S., AND HELLAND-HANSEN, W., 2018, Clinoforms and clinoform systems: Review and dynamic classification scheme for shorelines, subaqueous deltas, shelf edges and continental margins: Earth-Science Reviews, v. 185, p. 202-233.

PÉREZ-HUERTA, A., SUZUKI, M., CAPPELLI, C., LAIGINHAS, F., AND KINTSU, H., 2019, Atom Probe Tomography (APT) Characterization of Organics Occluded in Single Calcite Crystals: Implications for Biomineralization Studies: C — Journal of Carbon Research, v. 5, p. 50.

PÉREZ-HUERTA, A., WALKER, S.E., AND CAPPELLI, C., 2020, In Situ Geochemical Analysis of Organics in Growth Lines of Antarctic Scallop Shells: Implications for Sclerochronology: Minerals, v. 10, p. 529.

PETRASH, D.A., BIALIK, O.M., BONTOGNALI, T.R., VASCONCELOS, C., ROBERTS, J.A., MCKENZIE, J.A., AND KONHAUSER, K.O., 2017, Microbially catalyzed dolomite formation: From near-surface to burial: Earth-Science Reviews, v. 171, p. 558-582.

PIERSON, B.J., EBERLI, G.P., AL-MEHSIN, K., AL-MENHALI, S., WARRLICH, G., DROSTE, H.J., MAURER, F., WHITWORTH, J., DRYSDALE, D., AND VAN BUCHEM, F., 2010, Seismic stratigraphy and depositional history of the Upper Shu'aiba (Late Aptian) in the UAE and Oman: Barremian–Aptian stratigraphy and hydrocarbon habitat of the eastern Arabian Plate. GeoArabia Special Publication, v. 4, p. 411-444.

POMAR, L., BRANDANO, M., AND WESTPHAL, H., 2004, Environmental factors influencing skeletal grain sediment associations: a critical review of Miocene examples from the western Mediterranean: Sedimentology, v. 51, p. 627-651.

QING, H., AND MOUNTJOY, E.W., 1994, Formation of coarsely crystalline, hydrothermal dolomite reservoirs in the Presqu'ile Barrier, Western Canada Sedimentary Basin: AAPG bulletin, v. 78, p. 55-77.

REN, M., AND JONES, B., 2017, Spatial variations in the stoichiometry and geochemistry of Miocene dolomite from Grand Cayman: Implications for the origin of island dolostone: Sedimentary Geology, v. 348, p. 69-93.

RICH, J.L., 1951, Three critical environments of deposition, and criteria for recognition of rocks deposited in each of them: Geological Society of America Bulletin, v. 62, p. 1-20.

RIXHON, G., MAY, S.M., ENGEL, M., MECHERNICH, S., SCHROEDER-RITZRAU, A., FRANK, N., FOHLMEISTER, J., BOULVAIN, F., DUNAI, T., AND BRÜCKNER, H., 2018, Multiple dating approach (^{14}C, $^{23}0Th/U$ and ^{36}Cl) of tsunami-transported reef-top boulders on Bonaire (Leeward Antilles)–Current achievements and challenges: Marine Geology, v. 396, p. 100-113.

ROBERTS, J.A., KENWARD, P.A., FOWLE, D.A., GOLDSTEIN, R.H., GONZÁLEZ, L.A., AND MOORE, D.S., 2013, Surface chemistry allows for abiotic precipitation of dolomite at low temperature: Proceedings of the National Academy of Sciences, v. 110, p. 14540-14545.

ROEHL, P., AND CHOQUETTE, P., 1985, Perspectives on World-Class Carbonate Petroleum Reservoirs: AAPG Bulletin, v. 69, p. 148-148.

ROSE, K., AND KACZMAREK, S.E., 2019, Effects of Reactant Surface Area and Mineralogy on Dolomite Stoichiometry: AGUFM, v. 2019, p. PP41C-1574.

ROYSE, C., WADELL, J., AND PETERSEN, L., 1971, X-ray determination of calcite-dolomite; an evaluation: Journal of Sedimentary Research, v. 41, p. 483-488.

SALINAS, P., PAVLIDIS, D., XIE, Z., ADAM, A., PAIN, C., AND JACKSON, M., 2017a, Improving the convergence behaviour of a fixed-point-iteration solver for multiphase flow in porous media: International Journal for Numerical Methods in Fluids, v. 84, p. 466-476.

SALINAS, P., PAVLIDIS, D., XIE, Z., JACQUEMYN, C., MELNIKOVA, Y., JACKSON, M.D., AND PAIN, C.C., 2017b, Improving the robustness of the control volume finite element method with application to multiphase porous media flow: International Journal for Numerical Methods in Fluids, v. 85, p. 235-246.

SALINAS, P., PAVLIDIS, D., XIE, Z., OSMAN, H., PAIN, C., AND JACKSON, M., 2018, A robust mesh optimisation method for multiphase porous media flows: Computational Geosciences, v. 22, p. 1389-1401.

SALLER, A.H., 1984, Petrologic and geochemical constraints on the origin of subsurface dolomite, Enewetak Atoll: An example of dolomitization by normal seawater: Geology, v. 12, p. 217-220.

SALLER, A.H., AND HENDERSON, N., 1998, Distribution of porosity and permeability in platform dolomites: Insight from the Permian of west Texas: AAPG bulletin, v. 82, p. 1528-1550.

SCHLANGER, S.O., 1957, Dolomite growth in coralline algae: Journal of Sedimentary Research, v. 27, p. 181-186.

SCHMALZ, R., 1965, Brucite in carbonate secreted by the red alga Goniolithon sp: Science, v. 149, p. 993-996.

SCHMOKER, J.W., KRYSTINIK, K.B., AND HALLEY, R.B., 1985, Selected Characteristics of Limestone and Dolomite Reservoirs in the United States1: AAPG Bulletin, v. 69, p. 733-741.

SCHNEIDER, W.T., 1943, Geology of Wasson Field, Yoakum and Gaines Counties, Texas: AAPG Bulletin, v. 27, p. 479-523.

SIBLEY, D.F., 1980, Climatic control of dolomitization, Seroe Domi Formation (Pliocene), Bonaire, NA: SEPM Special Publication, v. 28, p. 247-258.

SIBLEY, D.F., 1982, The origin of common dolomite fabrics; clues from the Pliocene: Journal of Sedimentary Research, v. 52, p. 1087-110.

SIBLEY, D.F., 1991, Secular changes in the amount and texture of dolomite: Geology, v. 19, p. 151-154.

SIBLEY, D.F., DEDOES, R.E., AND BARTLETT, T.R., 1987, Kinetics of dolomitization: Geology, v. 15, p. 1112-1114.

SIBLEY, D.F., AND GREGG, J.M., 1987, Classification of dolomite rock textures: Journal of sedimentary Research, v. 57, p. 967-975.

SIBLEY, D.F., GREGG, J.M., BROWN, R.G., AND LAUDON, P.R., 1993, Dolomite crystal size distribution, Carbonate microfabrics, Springer, p. 195-204.

SIMMS, M., 1984, Dolomitization by groundwater-flow system in carbonate platforms: Gulf Coast Association of Geological Societies Transactions, v. 34, p. 411-420.

SMITH, A.B., 1990, Biomineralization in echinoderms: Skeletal biomineralization: patterns, processes and evolutionary trends, v. 1, p. 413-442.

STEEL, R., OLSEN, T., ARMENTROUT, J., AND ROSEN, N., 2002, Clinoforms, clinoform trajectories and deepwater sands: Sequence-stratigraphic models for exploration and production: Evolving methodology, emerging models and application histories: Gulf Coast Section SEPM 22nd Research Conference, Houston, Texas, p. 367-381.

STEINTHORSDOTTIR, M., COXALL, H., DE BOER, A., HUBER, M., BARBOLINI, N., BRADSHAW, C., BURLS, N., FEAKINS, S., GASSON, E., AND HENDERIKS, J., 2020, The Miocene: the Future of the Past: Paleoceanography and Paleoclimatology, p. e2020PA004037.

STROHMENGER, C.J., WEBER, L.J., GHANI, A., AL-MEHSIN, K., AL-JEELANI, O., AL-MANSOORI, A., AL-DAYYANI, T., VAUGHAN, L., KHAN, S.A., AND MITCHELL, J.C., 2006, High-resolution sequence stratigraphy and reservoir characterization of Upper Thamama (Lower Cretaceous) reservoirs of a giant Abu Dhabi oil field, United Arab Emirates: AAPG Memoir, v. 88, p. 139-171.

STUMM, W., AND MORGAN, J.J., 2012, Aquatic chemistry: chemical equilibria and rates in natural waters, v. 126, John Wiley & Sons.

SULAICA, J.L., 2015, Facies Distribution and Paleogeographic Evolution of Pleistocene Carbonates in Bonaire, Netherlands Antilles [unpublished Master's Thesis thesis]: Texas A&M University.

SUN, S.Q., 1994, A reappraisal of dolomite abundance and occurrence in the Phanerozoic: Journal of Sedimentary Research, v. 64, p. 396-404.

SWART, P., 1993, The formation of dolomite in sediments from the continental margin of northeastern Queensland, *in* McKenzie, J.A., Davies, P.J., and Palmer-Julson, A.A., eds., Proceedings of the Ocean Drilling Program, Scientific Results, Leg 133:: College Station, Texas, Ocean Drilling Program, p. 513-523.

SWART, P.K., AND BURNS, S., 1990, Pore-water chemistry and carbonate diagenesis in sediments from Leg 115: Indian Ocean, Proc., scientific results, ODP, Leg 115, Mascarene Plateau, ODP, Texas A&M University, College Station; UK distributors, IPOD Committee …, p. 629-645.

SWART, P.K., AND GUZIKOWSKI, M., 1988, Interstitial water chemistry and diagenesis of periplatform sediments from the Bahamas, ODP Leg 1011, *in* Austin, J.A.J., and Schlager, W., eds., Austin, JA, Jr, Schlager, W. Proceedings of the Ocean Drilling Program, Scientific Results, p. 363-380.

SWART, P.K., AND MELIM, L.A., 2000, The Origin of Dolomites in Tertiary Sediments from the Margin of Great Bahama Bank: Journal of Sedimentary Research, v. 70, p. 738-748.

TEOH, C.P., JACQUEMYN, C., AND LAYA, J.C., in review, The effects of dolomite geobodies within carbonate clinoforms on fluid flow and connectivity: Insights

from an outcrop analogue on Bonaire, The Netherlands: Marine and Petroleum Geology.

TESCH, P., REECE, R.S., POPE, M.C., AND MARKELLO, J.R., 2018, Quantification of architectural variability and controls in an Upper Oligocene to Lower Miocene carbonate ramp, Browse Basin, Australia: Marine and Petroleum Geology, v. 91, p. 432-454.

THOMAS, H., BRIGAUD, B., BLAISE, T., SAINT-BEZAR, B., ZORDAN, E., ZEYEN, H., ANDRIEU, S., VINCENT, B., CHIROL, H., AND PORTIER, É., 2021, Contribution of drone photogrammetry to 3D outcrop modeling of facies, porosity, and permeability heterogeneities in carbonate reservoirs (Paris Basin, Middle Jurassic): Marine and Petroleum Geology, v. 123, p. 104772.

THORNE, J., 1995, On the scale independent shape of prograding stratigraphic units, Fractals in petroleum geology and earth processes, Springer, p. 97-112.

TUCKER, M.E., AND WRIGHT, V.P., 1990, Carbonate sedimentology: Oxford, Blackwell, 482 p.

VAHRENKAMP, V.C., AND SWART, P.K., 1990, New distribution coefficient for the incorporation of strontium into dolomite and its implications for the formation of ancient dolomites: Geology, v. 18, p. 387-391.

WALTER, L.M., 1985, Relative reactivity of skeletal carbonates during dissolution: implications for diagenesis: SEPM Special Publication v. 36, p. 3-15.

WARD, W., AND HALLEY, R.B., 1985, Dolomitization in a mixing zone of near-seawater composition, late Pleistocene, northeastern Yucatan Peninsula: Journal of Sedimentary Research, v. 55, p. 407-420.

WARREN, J., 2000, Dolomite: occurrence, evolution and economically important associations: Earth-Science Reviews, v. 52, p. 1-81.

WEBER, J.N., AND KAUFMAN, J.W., 1965, Brucite in the caleareous alga Goniolithon: Science, v. 149, p. 996-997.

WEFER, G., AND BERGER, W.H., 1991, Isotope paleontology: growth and composition of extant calcareous species: Marine geology, v. 100, p. 207-248.

WEYL, P.K., 1960, Porosity through dolomitization--Conservation-of-mass requirements: Journal of Sedimentary Research, v. 30, p. 85-90.

WHITAKER, F.F., SMART, P.L., AND JONES, G.D., 2004, Dolomitization: from conceptual to numerical models: Geological Society, London, Special Publications, v. 235, p. 99-139.

WHITAKER, F.F., AND XIAO, Y., 2010, Reactive transport modeling of early burial dolomitization of carbonate platforms by geothermal convection: AAPG bulletin, v. 94, p. 889-917.

YAKHIYAYEV, N., COZZI, M., AND JENKINS, S., 2016, Overview of Depositional and Diagenetic Impacts on Reservoir Characterization, Karachaganak Field, Kazakhstan: SPE Annual Caspian Technical Conference & Exhibition.

ZAPATA, S., CARDONA, A., MONTES, C., VALENCIA, V., VERVOORT, J., AND REINERS, P., 2014, Provenance of the Eocene soebi blanco formation, Bonaire, Leeward

Antilles: Correlations with post-Eocene tectonic evolution of northern South America: Journal of South American Earth Sciences, v. 52, p. 179-193.

ZHANG, F., XU, H., KONISHI, H., AND RODEN, E.E., 2010, A relationship between d 104 value and composition in the calcite-disordered dolomite solid-solution series: American Mineralogist, v. 95, p. 1650-1656.

APPENDIX

Supplementary Table 1: Point counting and selectivity results

	Dol. CRA	Dol. OA	Dol. mat	Cal. CRA	Cal. OA	Cal. Mat	CRA Diff.	OA Diff.	Matrix Diff.
L1 SG_33	21%	0%	31%	25%	11%	12%	-9%	-100%	43%
L1 SG_34	43%	0%	32%	5%	4%	15%	77%	-100%	37%
L1 SG_35	13%	0%	27%	26%	8%	25%	-34%	-100%	4%
L1 SG_37	6%	0%	29%	12%	14%	38%	-35%	-100%	-14%
L3 SG_10	3%	0%	38%	26%	14%	18%	-80%	-100%	35%
L3 SG_9	28%	0%	29%	29%	11%	3%	-1%	-100%	82%
L1 SG_5	33%	5%	40%	2%	13%	7%	89%	-44%	70%
L1 SG_36	29%	7%	34%	8%	5%	17%	57%	19%	33%
L3 SG_5	0%	0%	18%	42%	18%	22%	-100%	-100%	-10%
L3 SG_6	3%	0%	9%	58%	12%	18%	-90%	-100%	-33%
L3 SG_7	4%	0%	19%	47%	12%	18%	-84%	-100%	3%
L3 SG_11	0%	0%	20%	36%	27%	17%	-100%	-100%	8%
L1 Wdg1.1	0%	0%	12%	44%	31%	13%	-100%	-100%	-4%
L1 Wdg1.2	0%	0%	8%	54%	28%	10%	-100%	-100%	-11%

Supplementary Table 2: Elemental analyses results

Sr CRA Dol. (ppm)	Mg/Ca CRA Dol. (ppm/ppm)	Sr Matrix Dol. (ppm)	Mg/Ca Matrix Dol. (ppm/ppm)	Sr Cement Dol. (ppm)	Mg/Ca Cement Dol. (ppm/ppm)	Sr CRA Cal. (ppm)	Mg/Ca Matrix Cal. (ppm/ppm)	Sr Matrx Cal. (ppm)	Mg/Ca CRA Cal. (ppm/ppm)	Sr Cement Cal. (ppm)	Mg/Ca Cement Cal. (ppm/ppm)
169.51	0.43	205.17	0.39	177.75	0.50	131.79	0.03	335.53	0.01	171.26	0.03

280.08	0.22	172.64	0.43	202.17	0.51	130.89	0.02	242.14	0.02	198.36	0.02
225.34	0.22	177.16	0.43	199.45	0.52	130.23	0.02	334.64	0.02	198.59	0.02
281.60	0.24	174.62	0.44	222.48	0.49	143.50	0.02	306.71	0.01	212.47	0.02
230.14	0.21	220.34	0.42	204.55	0.52	164.93	0.02	213.62	0.01	200.45	0.02
217.80	0.25	224.83	0.45	196.60	0.51	160.21	0.02	230.50	0.03	202.56	0.02
206.27	0.42	174.93	0.44	214.00	0.49	173.04	0.02	240.51	0.02	238.45	0.02
179.23	0.42	194.99	0.40	243.88	0.50	143.96	0.04	268.46	0.02	230.04	0.04
185.18	0.41	186.42	0.38	161.80	0.49	147.83	0.03	319.72	0.02	260.25	0.03
204.20	0.42	164.57	0.42	167.54	0.51	129.32	0.03	227.28	0.01	240.64	0.03
198.20	0.28	197.72	0.42	193.34	0.51	151.93	0.03	212.42	0.01	205.21	0.03
177.61	0.26	183.88	0.41	180.11	0.48	136.87	0.02	194.95	0.01	173.28	0.02
225.23	0.32	183.43	0.41	171.16	0.49	133.52	0.02	210.08	0.01	169.06	0.02
202.70	0.26	205.59	0.42	163.03	0.48	146.40	0.03	183.93	0.01	190.40	0.03
201.79	0.52	204.83	0.43	187.07	0.48	157.74	0.05	173.32	0.01	189.51	0.05
169.77	0.41	210.30	0.40	169.35	0.47	183.79	0.03	179.87	0.01	208.81	0.03
231.67	0.43	198.25	0.40	168.81	0.44	171.30	0.03	181.29	0.01	128.26	0.03
172.40	0.40	177.81	0.35	175.40	0.42	159.44	0.02	193.79	0.01	207.77	0.02
172.47	0.42	172.17	0.42	157.67	0.44	157.78	0.03	198.25	0.01	212.51	0.03
198.49	0.45	177.02	0.40	188.95	0.43	138.03	0.02	201.60	0.01	188.84	0.02
213.19	0.43	165.65	0.41	193.28	0.42			192.51	0.01	197.72	0.06
219.79	0.47	165.93	0.39	198.13	0.43			223.40	0.01	208.66	0.04
201.53	0.47	194.40	0.41	186.83	0.42			191.24	0.01	217.43	0.06
198.94	0.47	173.35	0.42	221.47	0.44			230.07	0.01	200.79	0.04
233.20	0.47	176.11	0.33	183.31	0.45			240.52	0.01	223.68	0.06
250.42	0.50	174.80	0.37	188.05	0.45			228.94	0.01	218.68	0.06
283.95	0.48	182.14	0.41	181.62	0.45			234.50	0.01	252.00	0.02
271.93	0.48	184.00	0.32	183.81	0.44			177.32	0.01	225.78	0.02
283.34	0.46	191.03	0.36	196.18	0.43			176.39	0.01	200.58	0.07
270.89	0.46	186.84	0.40	211.36	0.45			169.43	0.01	201.61	0.05
284.20	0.47	186.75	0.37	256.00	0.39			165.20	0.01	166.39	0.02
246.04	0.46	282.92	0.42	277.87	0.44			140.00	0.01	190.31	0.03
251.27	0.55	264.61	0.42	270.88	0.43			53.45	0.01	207.37	0.02

254.69	0.52	280.89	0.42	276.25	0.42		173.33	0.01	176.44	0.05
246.80	0.58	281.01	0.43	270.87	0.44		165.61	0.01	218.27	0.03
229.00	0.41	287.91	0.42	333.41	0.45		160.59	0.01	220.81	0.05
242.78	0.44	276.76	0.42	258.65	0.45		142.23	0.01		
240.98	0.45	266.73	0.45	276.09	0.43		118.99	0.01		
224.33	0.41	271.55	0.45	127.24	0.43		47.76	0.01		
267.61	0.45	265.48	0.44	47.97	0.43		142.00	0.01		
292.65	0.43	267.57	0.45	213.98	0.44		127.87	0.01		
258.42	0.44	267.58	0.45	217.62	0.43					
285.75	0.41	293.19	0.43	222.12	0.42					
268.65	0.43	259.33	0.45	222.03	0.44					
257.37	0.44	267.99	0.45	186.48	0.43					
289.43	0.43	265.96	0.45	210.21	0.44					
261.88	0.46	270.43	0.44	214.46	0.45					
279.53	0.42	261.49	0.44	282.02	0.44					
281.25	0.45	262.18	0.44							
291.40	0.44	216.53	0.45							
285.25	0.44	223.05	0.44							
307.75	0.44	216.32	0.44							
288.19	0.45	226.19	0.43							
258.42	0.45	276.43	0.41							
288.77	0.44	296.11	0.42							
259.68	0.43	298.03	0.43							
288.09	0.42	287.56	0.44							
261.16	0.45	290.20	0.43							
254.23	0.43	289.05	0.43							
		289.27	0.43							